EFFECT OF GRAIN STRUCTURE AND DOPING ON THE MECHANICAL PROPERTIES OF POLYSILICON THIN FILMS FOR MEMS

BY

NAGA SIVAKUMAR YAGNAMURTHY

DISSERTATION

Submitted in partial fulfillment of the requirements
for the degree of Doctor of Philosophy in Aerospace Engineering
in the Graduate College of the
University of Illinois at Urbana-Champaign, 2013

Urbana, Illinois

Doctoral Committee:

Professor Ioannis Chasiotis, Chair and Director of Dissertation
Professor Philippe H. Geubelle
Professor John Lambros
Professor Nancy R. Sottos

ABSTRACT

Freestanding devices fabricated for Microelectromechanical Systems (MEMS) employ slender polysilicon flexures that are prone to failure due to large operating stresses. Polycrystalline silicon (polysilicon) films with improved mechanical properties to meet demanding applications could be engineered by modification of the material microstructure. Such advances require detailed experimental studies and quantitative understanding of the convoluted effects of the processing methods on the ensuing mechanical properties. This dissertation investigated the role of grain size and doping on the nature and origin of critical flaws that determine the tensile strength and the local resistance to crack initiation in 1-μm thick polysilicon films, as quantified by the effective mode I critical stress intensity factor, $K_{IC,eff}$.

For the purposes of this study microscale polysilicon thin film specimens were fabricated by a custom process at the Sandia National Laboratories. The films were comprised of either columnar grains (grain size 285 nm) or a laminated structure (grain size 125 nm), and were doped with different concentrations of Phosphorus (P). The columnar grain polysilicon typically had 1 - 2 grains across the film thickness, while the laminated polysilicon contained ten grains across the film thickness, each confined in a 100-nm thick layer. The grain structure and doping concentration had no effect on the elastic stiffness of polysilicon: the average Young's moduli of all polysilicon films were in the narrow range of 153 - 158 GPa. On the other hand, the tensile strength values of undoped columnar grain and laminated polysilicon differed significantly, averaging 1.31±0.09 GPa and 2.44±0.28 GPa, respectively. Heavy doping further impacted the strength of the former type of polysilicon (0.92±0.10 GPa) due to the formation of large sidewall defects at high concentrations of P which, however, had no effect on the tensile strength of laminated polysilicon.

The nature and type of the critical sidewall defects were independent of the specimen size: on grounds of the cumulative Weibull probability distribution function, the results of the present experiments predicted quite reasonably the tensile strength of polysilicon specimens that were 180 times smaller in size. The strength of polysilicon

films scaled with the sidewall surface area (or equivalently the specimen length), which is also the region where the major critical flaws were identified. Notably, in the absence of the initial critical sidewall defects, the average tensile strength of undoped columnar polysilicon increased by 70%, namely from 1.31±0.09 to 2.2±0.11 GPa, thus approaching the strength of laminated polysilicon. The critical defects in columnar polysilicon were located at the specimen free edges which were defined by reactive ion etching (RIE). These defects were initiated at grain boundaries during RIE and were further exacerbated by the reactions taking place during heavy P-doping in high temperature annealing.

Measurements of $K_{IC,eff}$ were used to evaluate the effect of grain structure and doping on the resistance of the two types of polysilicon to crack initiation. The values of $K_{IC,eff}$ for all the polysilicon films were in the range of 0.8 - 1.2 MPa$\sqrt{m}$. Contrary to the trends in tensile strength values, the $K_{IC,eff}$ of columnar polysilicon was higher than that of laminated polysilicon, but the latter demonstrated a much smaller variability in $K_{IC,eff}$, which was owed to the averaging effect of its laminated structure. The $K_{IC,eff}$ of columnar polysilicon further increased by 10% as a result of heavy P-doping, which, on the contrary, had no effect on the $K_{IC,eff}$ of laminated polysilicon. Thus, P-doping only modestly increased the fracture resistance of columnar polysilicon, although its effect on the tensile strength was clearly detrimental.

Finally, using the measured $K_{IC,eff}$ values and the precise defect geometries determined by Atomic Force and Scanning Electron Microscopy, the tensile strength of different polysilicon films was calculated by linear elastic fracture mechanics models for semi-elliptical surface cracks and quarter elliptical edge cracks. The strength values estimated by a quarter elliptical edge crack analysis agreed fairly well with the values obtained by uniaxial tension experiments, further supporting the electron microscopy observations and the Weibull scaling predictions that the tensile strength of as-fabricated columnar grain polysilicon specimens was governed by sidewall defects. On the other hand, the strength values estimated by an elliptical surface crack analysis agreed fairly well with uniaxial tension experiments with columnar grain polysilicon specimens whose sidewall defects were removed via ion beam milling.

ACKNOWLEDGEMENTS

I would like to sincerely thank my advisor Prof. Chasiotis for providing me an opportunity to work with him on this project. His constant support and invaluable guidance were crucial in solving the technical challenges faced during this dissertation research and successfully accomplishing the dissertation objectives in a timely manner. I would also like to thank the Air Force Office of Scientific Research for funding the project through the grant FA9550-09-1-0535 with Dr. B.L. Lee as program manager and Dr. Brad Boyce from the Sandia National Labs for providing us the specimens needed for experiments. Additionally, I would like to thank the Department of Aerospace Engineering at University of Illinois Urbana Champaign for financially supporting me in the form of Teaching Assistantship after the grant ended. Along with my advisor, Prof. Chasiotis, I would like to extend my sincere gratitude to Prof. Geubelle, Prof. Lambros, and Prof. Sottos for agreeing to serve on my PhD committee. Their comments during my preliminary and final exams were crucial in steering my research in the appropriate direction.

I would like to acknowledge the Aerospace Engineering staff Staci, Kendra, and Laura for assisting me in various administrative related issues. The machine shop staff members also helped me in various instances by accommodating by job requests and turning back the machined parts in time that enabled me to meet my research deadlines. I would like to thank the staff at the Material Research Lab (MRL) for training me on various metrology instruments used in my research. Special thanks to Scott Maclaren at MRL for his extended support while imaging crack tips using AFM. I would also like to thank Dr. David Farrow, lab manager for the Mechanical Testing Laboratory in Talbot Lab, for letting me use the Vicker's hardness tester to create fracture specimens.

I thank my past and present labmates who helped me in various aspects during my PhD. I would like to specially thank Dr. Krishna Jonnalagadda for teaching me uniaxial tension testing of thin films. Additionally, I would like to thank Mr. Pavan Kolluru, Mr. Tanil Ozkan, Mr. Debashish Das and Dr. Nikhil Karangjaokar from my group, for helping me with the Focus Ion Beam, high speed camera, and infrared camera. I enjoyed

all the insightful discussions with my present and past colleagues of Nano-Mechanics Research Lab and would like to thank them for their support and companionship throughout the research.

Finally, I would like to thank my family members and fiancé, Saismrithi, who were always there for me and supported me in difficult situations. All my friends Nikhil, Pavan, Sastry, Gasak, Varun, Sreekanth, Raj, and cricket and dance folks made my stay at Champaign enjoyable and memorable.

TABLE OF CONTENTS

CHAPTER 1

Introduction

1.1 Motivation and Relevance

Polycrystalline silicon (polysilicon) has been the most common material for Microelectromechanical Systems (MEMS) because of its advantageous electrical and mechanical properties as well as the mature and versatile fabrication processes for intricately shaped polysilicon devices [1]. MEMS perform most reliably as two-dimensional suspended devices comprised of slender beams and flexures to allow for large in-plane displacements under relatively low operating forces. Common MEMS devices that employ polysilicon as structural material include comb-drive actuators [2,3], airbag sensors for automobiles [4,5], and micro-mirrors in LCD projectors [6-9]. These MEMS-based sensors have several advantages over large scale counter parts, such as light weight, small form factor, and the ability to batch produce hundreds to thousands of devices on a single silicon wafer. Figure 1.1 shows a Scanning Electron Microscopy (SEM) image of a drive gear [10], and a transmission gear assembly [11] fabricated at the Sandia National Laboratories using Sandia's Ultra-planar Multi-level MEMS Technology 5 layer process (SUMMiT V^{TM}) [12]. In this process, multiple layers of 1-2.5 μm thick polysilicon films are deposited with alternating sacrificial oxide layers combined with intermediate steps for patterning of the polysilicon layers and selective etching of the sacrificial oxide layers to obtain quasi-three dimensional MEMS structures. A detailed description of the SUMMiT V^{TM} process for polysilicon based MEMS is provided in [12].

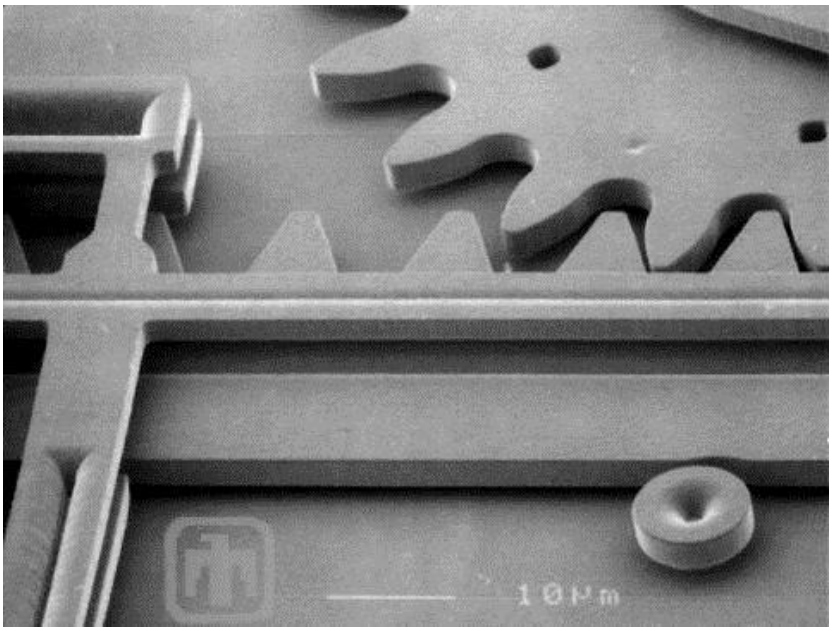

(a)

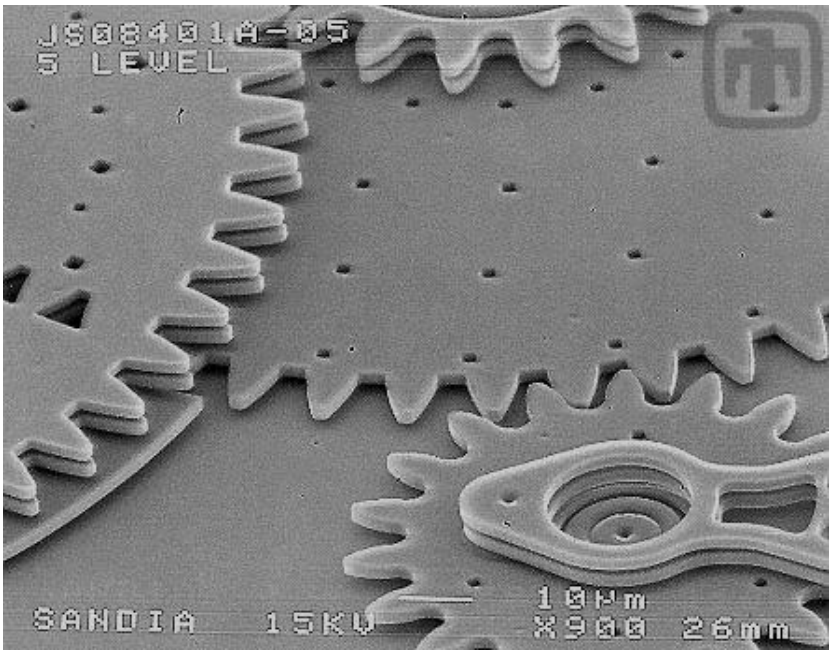

(b)

Figure 1.1. Polysilicon based **(a)** drive gear, and **(b)** transmission gear assembly fabricated at the Sandia National Laboratories via the SUMMiT V^{TM} process [10,11]. Courtesy of Sandia National Laboratories, SUMMiT™ Technologies.

The microdevices shown in Figure 1.1 are operated with the application of a bias voltage to achieve electrostatic actuation. However, in order to reach the desired motion, slender components can be subjected to large stresses that often exceed 1 GPa. From a stress view point, it is advantageous to increase the thickness and width of flexures in surface micromachined MEMS, which provides additional benefits in terms of averting device stiction [13,14]. However, an increase in component stiffness results in significantly higher operating voltages, often exceeding 100V, which is undesirable in most applications. Additionally, the brittle nature of polysilicon MEMS presents the advantage of dimensional stability under high applied stresses, but also raises the concern of catastrophic brittle fracture due to voids, crevices or micro-cracks on the surface or in the volume of the material [15]. Prior research has shown the potential of increasing the mechanical strength of small polysilicon parts to ~3.5 GPa [16-18], which, however, is still far lower than the value reported from experiments with defect-free single crystal silicon beams [19,20]. For instance, the strength of near defect-free single crystal silicon has been shown to be of the order of 10-20 GPa [19-23], which is far higher than the tensile strength of polycrystalline silicon reported in the range of 1-5 GPa [16,18,24-28]. The latter depends on the specimen size and the applied stress profile, consistently with expectations for brittle materials [15,24,26]. The strength of polysilicon films measured from bending experiments [29] is in the range of 5-10 GPa, which is higher than that measured in the range of 1-5 GPa from microscale tension experiments [16,24-28]. Failure initiation in brittle materials occurs at random critical flaws that cause local stress amplification. In a tension experiment, the entire specimen experiences a uniform stress, whereas in a bending experiment, the maximum stress occurs only at a small fraction of the specimen volume, and potentially not in the area of high critical defect density. Thus, the probability for a major flaw to result in critical stress and specimen fracture is quite lower when the material is loaded in bending [30]. Hence, the strength of polysilicon beams measured from bending experiments is expected to be higher. The types of catastrophic flaws and the exact location of failure initiation are strongly tied to the method of specimen fabrication: prior research has shown that film deposition, Reactive Ion Etching (RIE) patterning, doping, annealing and sacrificial etching influence in

different degrees the material porosity and the surface and sidewall roughness [18], which are among the primary forms of catastrophic flaws.

Even though single crystal silicon is known to exhibit high intrinsic strength (~20 GPa) [21], for most MEMS applications, films are grown by chemical vapor deposition (CVD) in the form of amorphous silicon or polycrystalline silicon [31]. Single crystal silicon is anisotropic following the diamond cubic structure and, hence, the mechanical properties of polysilicon films such as the elastic modulus, fracture strength, and toughness are dependent on microstructure. The microstructural features of polycrystalline silicon, such as grain structure, grain size, texture, and surface roughness, depend on fabrication conditions [32-39]. Prior experimental studies have shown a significant effect of microstructure on the mechanical properties of polysilicon films [29,40,41]. Additionally, polysilicon films are doped with boron (B) or phosphorus (P) to ensure electrical conductivity. The presence of P-dopants in silicon during high temperature annealing has been shown to enhance grain growth and change the microstructure of the resulting polysilicon films [32,34,35]. While the grain size does not directly impact the fracture strength, the size of defects formed for larger grain sizes are also larger, thus resulting in lower strength compared to small grain polysilicon processed under identical conditions [40,41]. Similarly, other studies have shown a drop in the strength of polysilicon due to severe structural degradation when exposed in aqueous Hydrofluoric (HF) acid based etchants [38,39,43]. Therefore, the origins of lower strength for large grain polysilicon should be sought in the side effects of the fabrication methods, e.g. prolonged annealing at high temperature, high P-doping, and prolonged exposure to HF etching. Moreover, P atoms are expected to occupy either interstitial or substitutional sites in silicon and their effect on the cohesive strength of silicon is still unknown. Extensive literature data, not always connected to systematic studies, have shown that mechanical performance metrics, such as the tensile strength and fracture toughness, must be related to individual processing steps to determine the reliability limiting fabrication processes [17-20,26,29,38-41,43]. Thus, before proceeding, it is important to review the effect of various processing parameters, such as film growth temperature, annealing, doping, and sacrificial etching, on the evolution of the material

microstructure and its effect on the defect structure and the mechanical properties of polysilicon.

1.2 Fabrication vs. Microstructure and Mechanical Properties of Polysilicon

The microstructure of silicon deposited using low pressure chemical vapor deposition (LPCVD) process is dependent on the growth temperature [32]. While silicon films deposited above the critical temperature of 580 ºC result in polycrystals with columnar grain structure, films deposited below this temperature are amorphous. The surface roughness of amorphous silicon films has been reported to be smaller than that of columnar polysilicon [31]. In the absence of major defects, such as cracks or voids, the surface roughness often governs the tensile strength of brittle materials. Deep surface grooves act as microcracks that increase the local stress and initiate early failure. Ballarini et al. [29] measured the strength of polycrystalline and amorphous silicon by on-chip MEMS-based microscale bending tests. In their study, the amorphous polysilicon films failed under a maximum bending stress of 9.7±2 GPa compared to 4.9±0.4 GPa for columnar polysilicon films. The high strength values were possible due to the very small specimen volume: the width and thickness of the specimens tested in bending were 5 μm and 3 μm, respectively. The difference in the strength was attributed to the smoother surface of amorphous silicon with smaller fracture initiating flaws. They also reported the average mode I critical stress intensity factor (K_{IC}) of polycrystalline and amorphous silicon films to be 1±0.3 MPa√m and independent of the material microstructure. However, Tsuchiya et al. [40] reported the strength of amorphous silicon to be smaller than that of polysilicon, which they attributed to the presence of 0.4% atomic hydrogen and large defects in amorphous silicon. They also noticed that the strength of polysilicon depended on the annealing temperature which, in turn, dictated the grain size. The grain size of polysilicon films produced by annealing of amorphous silicon films at 600 ºC (~2 μm) was much larger than that of films formed at 1000 ºC (~0.3 μm): at lower temperatures, the crystallization rate is higher than the nucleation rate, which leads to larger grains [40]. While annealing at higher temperatures is expected to increase the

grain size of a material through primary and secondary crystallization [32], one should also account for the initial microstructure of the material. When annealed at lower temperatures in the range of 600-700 ºC, amorphous silicon produced polycrystalline silicon with significantly larger grain size than that formed at higher temperatures (above 1000 ºC) due to differences in the kinetics of nucleation and crystallization [40]. Hence, the tensile strength of polysilicon obtained by annealing of amorphous silicon at 600-700 ºC was lower than that annealed at 1000 ºC due to the presence of larger defects, as expected in a material with larger grains. However, another study [25] reported an enhancement in the tensile strength of polysilicon with increasing grain size, which was attributed to better interface between the large grains. In this study, the grain size of as-deposited polysilicon films increased from 50 nm to 100 nm as a result of high temperature annealing at 1000 ºC in N_2 atmosphere. In order to achieve films with even larger grain size (500 nm), the polysilicon films were oxidized at 900 ºC in absence of chlorine, which has been shown to enhance grain growth [42]. The oxide layer was subsequently etched using buffered oxide etchant (BOE). The contradicting reports on the effect of microstructure and grain size on the strength of polysilicon are often the result of subtle or fundamental variations in fabrication processes which are not always possible to account for. Hence, further experiments are needed for different fabrication processes to elucidate the microstructural aspects that determine the failure properties of polysilicon films.

Recently, a new microstructure was developed by the Sandia National Laboratories, in which alternate amorphous and polycrystalline silicon layers were deposited and subsequently annealed to obtain a laminate structure [41]. The cross-sectional Transmission Electron Microscopy (TEM) images shown in Figure 1.2 illustrate the different structure of columnar and laminated polysilicon films. Specifically, the grain size of laminated polysilicon (~125 nm) was quite smaller than the in-plane grain size of columnar grain polysilicon (~285 nm). The characteristic strength of undoped laminated polysilicon was 2.79 GPa [41], which was 60% higher than that of undoped columnar polysilicon (1.74 GPa), which was attributed to differences in surface roughness and grain boundary (GB) associated defects in the form of surface grooves. Other reports

[26,43] have also shown that the surface roughness is one of the factors that affect the tensile strength of polysilicon. An experimental study by Boyce et al. [26] investigated the strength of all polysilicon layers from the Sandia SUMMiT V^{TM} process. The authors reported a process-induced layer dependence on the tensile strength of polysilicon, which was attributed to variations in sidewall roughness. Notably, the root mean square (RMS) surface roughness of the topmost polysilicon layer (Poly 4) was smaller than the preceding polysilicon layers, which also exhibited the highest strength of all five layers. While all five polysilicon layers were fabricated via LPCVD on sacrificial oxides, each layer was subjected to different total annealing times which potentially had caused the differences in surface roughness. In addition to the growth temperature, the annealing time and temperature have been shown to modify the grain size, surface roughness and texture, which dictate the ultimate mechanical properties.

In a systematic study [33], the effect of annealing temperature on grain growth and surface roughness of LPCVD polysilicon was studied with the help of Atomic Force Microscopy (AFM). The films were deposited at 620 ºC and subsequently annealed at 920 ºC, 970 ºC, 1020 ºC, and 1070 ºC for 40 min. AFM topography images of the films subjected to each annealing temperature are shown in Figure 1.3. When annealed at 1070 ºC for 40 min, the grains of as-deposited polysilicon grew from 80 nm to 400 nm in the form of clusters. As a result of grain growth, a reduction in the RMS roughness took place after annealing at higher temperatures. For example, the RMS roughness of polysilicon films annealed at 1070 ºC was approximately 3.2 nm and 40% lower than the films annealed at 970 ºC, measured as 5.2 nm. In another report by Kammins [32], the structure of polysilicon was found to be stable with a minimal grain growth when annealed below 1000 ºC. However, they observed a significant grain growth in polysilicon films when annealed over 1100 ºC. Changes in texture were recorded by X-ray diffraction studies on polysilicon films annealed above 1000 ºC, where the predominant (110) texture was reduced in favor of (111) and (331) texture. While high temperature annealing can lower the surface roughness and potentially increase the fracture strength, it also alters the grain size and texture which determine the material resistance to fracture near defects. The critical stress intensity factor, K_{IC}, of single crystal

silicon for (100), (110) and (111) crystallographic planes has been reported as 0.95 MPa√m, 0.90 MPa√m, and 0.83 MPa√m, respectively [44]. A reduction in surface roughness via grain growth could come with the side effect of reducing the average K_{IC}. Hence, differences in strength of columnar and laminated polysilicon, measured in [26,41], could not be attributed solely to differences in surface roughness and GB grooves without taking into account changes in the fracture resistance of the material.

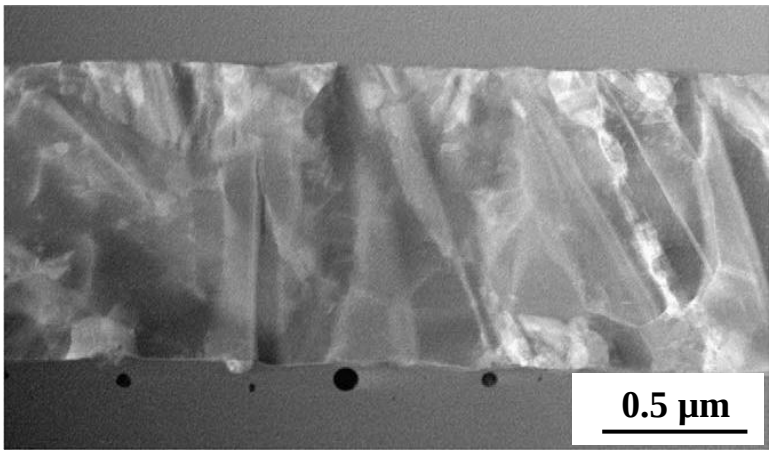

(a)

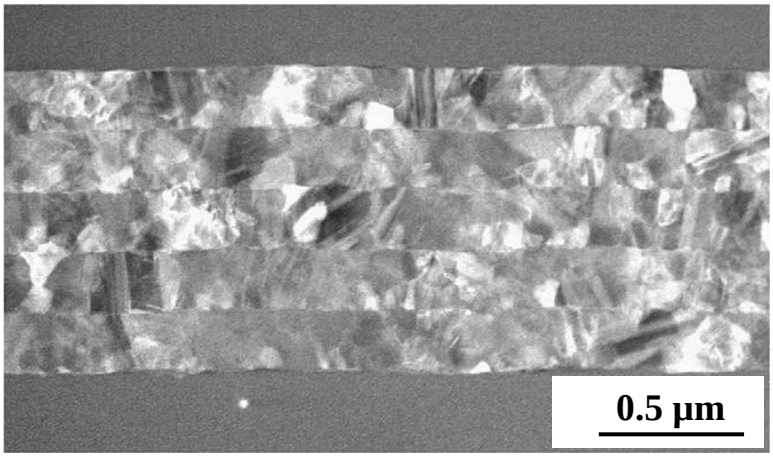

(b)

Figure 1.2. Cross-sectional TEM images showing the grain structure in **(a)** columnar and **(b)** laminated polysilicon. Reprinted from [41], with permission from Elsevier.

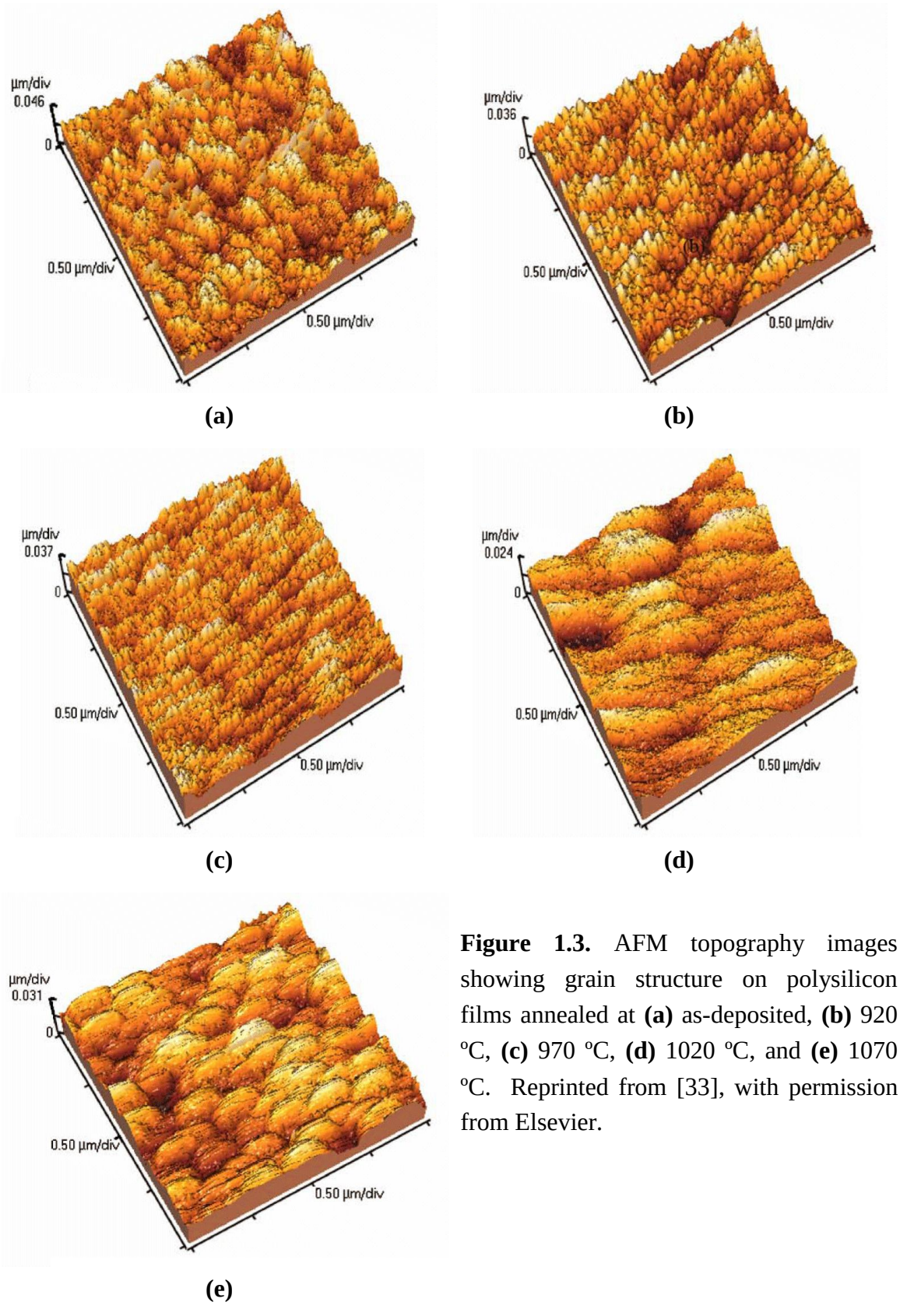

Figure 1.3. AFM topography images showing grain structure on polysilicon films annealed at **(a)** as-deposited, **(b)** 920 ºC, **(c)** 970 ºC, **(d)** 1020 ºC, and **(e)** 1070 ºC. Reprinted from [33], with permission from Elsevier.

Microstructural changes occurring to polysilicon during annealing, which affect the grain size and surface roughness, are further accentuated by the presence of dopants such as P [32]. P-doping of polysilicon films can be carried out by ion implantation [31,32,45] or diffusion from sacrificial phosphosilicate glass (PSG) layers [31,32]. In the former method, the desired amounts of fast moving P ions are implanted inside amorphous or polycrystalline silicon films which are later encapsulated within a thin oxide layer and are heat treated to diffuse P atoms uniformly throughout the film [31,32]. In the latter method, PSG with different concentrations of P is deposited as two sacrificial layers that encapsulate a polysilicon film, which is then annealed at high temperatures to diffuse P from the adjacent PSG layers into the polysilicon layer. In the presence of P dopants, the kinetics of grain growth during annealing for 20 min at 1000 ºC has been shown to increase with the concentration of P [34,35] for three different concentrations of 1.2×10^{20}, 2.5×10^{20}, and 7.5×10^{20} cm^{-3}. As shown in the TEM images of the annealed films in Figures 1.4(a-c), grain growth was modest until the critical concentration of 4×10^{20} cm^{-3}. In the case of P concentration exceeding 7.5×10^{20} cm^{-3}, significant grain growth took place at even lower temperatures such as 800-900 ºC. Similar observations of the impact of P on grain growth during annealing have been reported in [46-48].

Grain growth in polysilicon films is accompanied by changes in its surface roughness and grain texture. Upon doping, P atoms occupy either interstitial or substitutional sites of silicon, which changes the intrinsic material properties. Moreover, diffusion of P is faster through GBs [32,49] and upon cooling down after annealing, P atoms segregate primarily at GBs. However, the effect of P-doping on toughening and strengthening is still inconclusive [41,50-52]. Biebl and von Philipsborn [50] reported 25% smaller strength for P-doped polysilicon as compared to undoped, which was attributed to pronounced surface roughness and large defects that formed during extensive grain growth. Similarly, the authors in [41] reported a 15% reduction in the strength of columnar polysilicon films due to severe defects that formed as a result of P-doping, whereas the strength of laminated polysilicon was found to be independent of doping. Thus, it is apparent that P-doping has an indirect but important effect on the strength of polysilicon films.

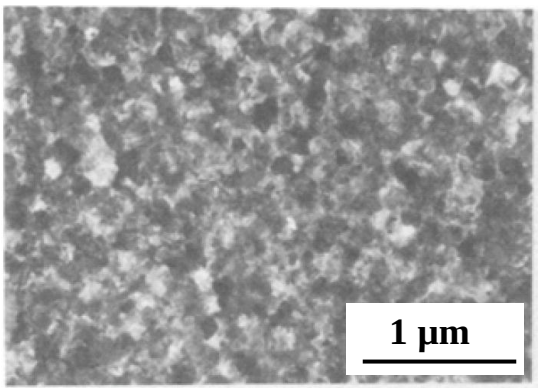

(a)

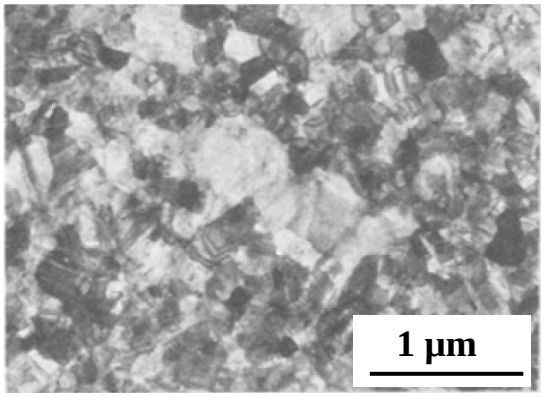

(b)

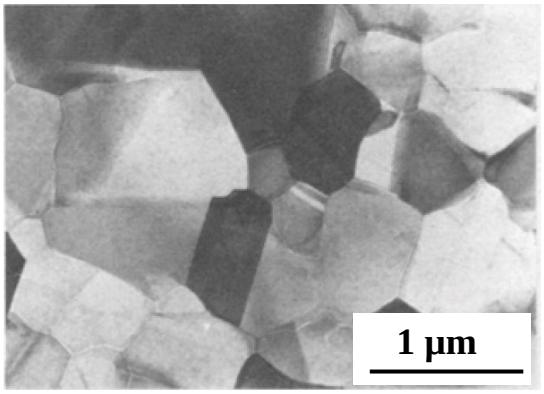

(c)

Figure 1.4. TEM images showing primary grain growth in polysilicon films doped with **(a)** 1.2×10^{20}, **(b)** 2.5×10^{20}, and **(c)** 7.5×10^{20} cm^{-3} concentration of P annealed at 1000 ºC for 20 mins [34]. Reproduced by permission of ECS – The Electrochemical Society.

Furthermore, the reported reduction in the strength of P-doped polysilicon films may not be solely attributed to the large defects without considering the change in the material's fracture resistance as a result of doping. There are very few reports on the effect of P-doping on the fracture toughness of polysilicon: Zeng et al. [51] reported a 3% increase in the critical stress intensity factor of silicon that is heavily P-doped, while Swadener and Nastasi [52] reported an equally insignificant effect. Both studies [51,52] measured the value of K_{IC} of polysilicon by using indentation experiments, which are subject to uncertainties, especially in the presence of a substrate. Fracture experiments with polysilicon films containing sharp cracks, such as those reported in [53], are necessary to accurately quantify the dependence of K_{IC} on P-doping. With the knowledge of material's K_{IC} and the surface flaw spectrum, predictions for the strength of polysilicon films could be made with the help of linear elastic fracture mechanics (LEFM), which could reduce the need for statically significant number of tests with small scale specimens.

Apart from annealing, the exposure of polysilicon to aqueous 49% HF has also been shown to enhance the surface roughness and accentuate GB grooves that reduce the material strength. Surface micromachined polysilicon films are commonly deposited on a sacrificial oxide layer that is later immersed in 49% HF to etch the oxide and obtain freestanding polysilicon structures. While LPCVD polysilicon has been shown by some groups to resist HF attack [36], other reports [37-39,43,43] have observed structural degradation at polysilicon GBs that led to significantly reduced effective Young's modulus and mechanical strength. In a parametric study [36], the effect of HF etching on structural degradation of polysilicon was studied as a function of annealing and doping conditions. Irrespectively of the annealing conditions, undoped polysilicon was resistant to 49% HF, buffered HF and vapor HF. However, P-doped polysilicon GBs were affected by BOE and vapor HF but not 49% HF, and the extent of structural damage was found to be dependent on the annealing temperature and the nature of the underlying layer (i.e. thermal oxide or silicon nitride). On the other hand, Chasiotis and Knauss [43] reported on the reduced strength of P-doped polysilicon specimens fabricated via the multi-user MEMS process (MUMPs), which were exposed in 49% HF for extended times. With the

help of an AFM, they also showed an attendant increase in surface roughness as a result of prolonged exposure to 49% HF etchant. Surface grooves and pores were found at GBs of polysilicon films subjected to longer HF release times, as shown in Figure 1.5. The pores at GBs were attributed to electrochemical (galvanic) corrosion assisted by the Au layer deposited at some areas to provide electrical contact. As a result, the strength of MUMPs polysilicon was found to be dependent on HF release time. While specimens etched for less than 8 min exhibited a strength of 1.43±0.1 GPa, polysilicon specimens exposed for 20 min had a mere 0.25 GPa strength, following a linear drop in strength at the rate of 0.1 GPa/min of exposure to 49% HF. The presence of P was reported to enhance electrochemical corrosion and weaken the GBs.

In the absence of a Au metallization layer, Cho and Chasiotis reported the average strength of MUMPs polysilicon as 1.81±0.1 GPa, namely 25% higher than that of polysilicon films with Au contacts [54]. Similarly, Kahn et al. [37] studied the effect of HF etching on undoped and P-doped polysilicon films in the presence and absence of Au metallization. For undoped polysilicon exposed to 49% HF for 30 min followed by a 3 min rinse in BOE, the RMS surface roughness of as-deposited films increased from 4.4 nm to 8.6 nm in absence of a Au layer and to 16.2 nm in presence of a Au layer. In the case of P-doped polysilicon films, the RMS roughness increased significantly to 44 nm and 26.8 nm for polysilicon with and without a Au layer, respectively. The characteristic strength and Young's modulus of MUMPs polysilicon films in presence of a Au layer that underwent microstructural changes due to galvanic corrosion in 49% HF was investigated by [17]. Along the same lines, the strength of polysilicon dropped from 1.2 GPa for specimens etched for 5 min to almost 0.1 GPa for specimens exposed for 60 min to 49% HF. The strength decreased asymptotically with etching time, unlike the linear trends reported in [38,43]. Similarly, the apparent Young's modulus also decreased nonlinearly from 180 GPa to 25 GPa for etching times ranging between 5 - 90 min. The reduced strength and the effective elastic modulus were attributed to severe GB porosity caused by electrochemical corrosion as shown before in detail in [43,55].

Contrastingly, the authors in [39] showed that there was no major effect of a Au layer on the surface degradation of P-doped MUMPs polysilicon exposed to 49% HF for

90 min. The RMS surface roughness of these films treated with 49% HF with and without the presence of a Au layer was measured as 5.20 nm and 5.17 nm, respectively. However, surface pitting or pores measuring 5-10 nm in diameter were observed at GBs in both cases, as shown in Figure 1.6. Even though the surface morphology of polysilicon with and without a top metal layer exposed to 49% HF was identical, a substantial difference was observed in the resonant frequency of these polysilicon beams. Therefore, these pores were speculated to be deeper in the case of polysilicon with a top Au layer, which caused a reduction in the beam's resonance frequency. Additional contrasting results have been reported in a study in [38] which reported an increase in the Young's modulus and a reduction in the burst pressure of polysilicon membranes exposed to 49% HF.

This background information points to the fact that the mechanical properties of polysilicon could be improved via judicious control of processing. This dissertation aims at shedding light into this challenge by employing a new type of polysilicon films with modified microstructure, recently developed by the Sandia National Laboratories [41].

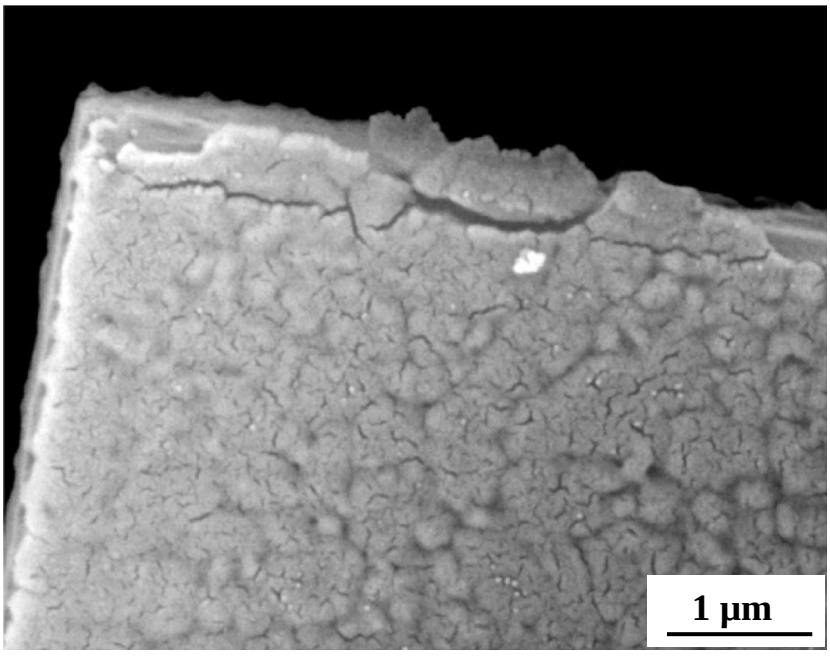

Figure 1.5. SEM image showing GB grooves on the top surface of a polysilicon film treated for for 13 min by 49% HF. Reprinted from [43], with permission from Elsevier.

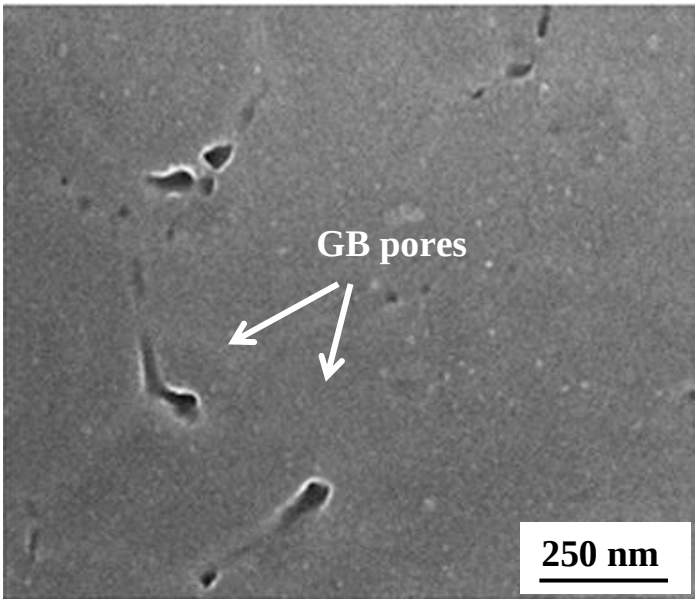

(a)

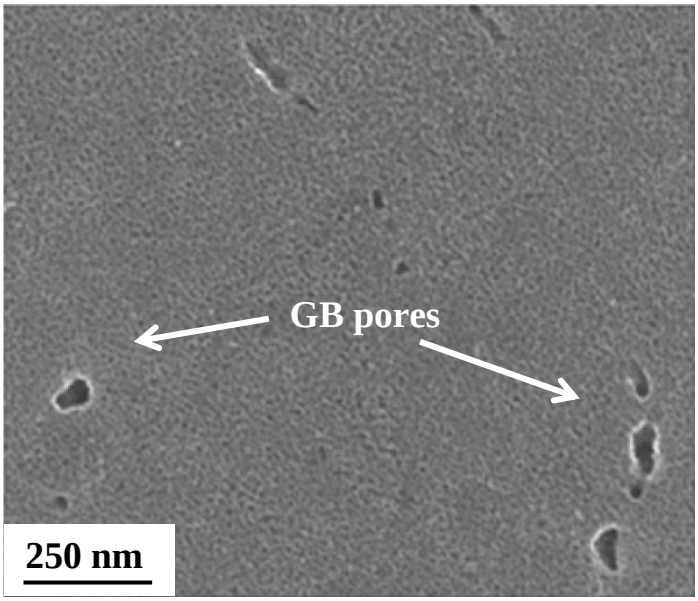

(b)

Figure 1.6. Surface morphology showing GB pores in P-doped polysilicon films **(a)** without, and **(b)** with Au metallization, exposed to 49% HF for 90 min [39]. The presence of the Au layer did not further degrade polysilicon. © 2007 IEEE

1.3 Objectives and Approach of this Dissertation Research

This Ph.D. dissertation research aims at addressing the convoluted effect of doping and grain size on the strength and fracture of polysilicon films fabricated by an experimental run at the Sandia National Laboratories. The mechanical properties of polysilicon manufactured by the regular SUMMiT V^{TM} process have been reported before by Chasiotis and Knauss [43] and Boyce et al. [41], who identified the specimen sidewalls as the location of the flaws controlling failure. More recently, control of grain size has been explored by the Sandia National Laboratories via deposition of laminated polysilicon. A study of this type of polysilicon films by Boyce et al. [41] reported a 60-90% increase in strength compared to columnar polysilicon. This dissertation research addresses several ensuing questions, among them:

(a) The scalability of polysilicon strength data derived from large and small specimens fabricated by the methods described in [41].
(b) The convergence of the mechanical strength of columnar and laminated polysilicon films, once the critical flaws in as-fabricated columnar polysilicon are eliminated.
(c) The ability to make mechanical strength predictions based on a characterization of edge and surface flaws and a fracture mechanics analysis.
(d) The role of grain homogeneity and dopant content on the local fracture behavior of laminated and columnar polysilicon.

These questions are pursued by a thorough mechanical property characterization of columnar and laminated polysilicon films that are doped with different concentrations of P. Six types of 1-μm thick polysilicon films are used in this study:

(a) undoped columnar polysilicon,
(b) lightly doped (0.5% PSG) columnar polysilicon,
(c) heavily doped (2.0% PSG) columnar polysilicon,
(d) undoped laminated polysilicon,
(e) lightly doped (0.5% PSG) laminated polysilicon,
(f) heavily doped (2.0% PSG) laminated polysilicon.

Uniaxial tension experiments are conducted with dog-bone shaped freestanding polysilicon specimens to obtain stress vs. strain response. Optical images of the specimen's top surface containing a speckle pattern are captured during each experiment and full-field strains are calculated by Digital Image Correlation (DIC).

Microscale fracture experiments are conducted with polysilicon films containing a sharp crack to calculate the effective critical stress intensity factor, $K_{IC,eff}$, by LEFM. A statistical analysis of the tensile strength data is conducted using the Weibull cumulative probability density function. The scalability of strength data is evaluated by using Weibull statistics and data sets from large specimens tested in this work and from much smaller specimens published in literature. While this analysis sheds light into the flaw population in as-fabricated polysilicon films, further steps are taken to evaluate the mechanical durability of columnar polysilicon films in the absence of the critical flaw population located at the specimen sidewalls. Finally, the tensile strength of polysilicon is estimated from the measured geometry of critical surface flaws and LEFM, and it is compared with measurements.

1.4 Outline of this Dissertation

This dissertation consists of four Chapters beginning with an Introduction to the state-of-the-art and current open issues. Specimen fabrication and the resulting microstructure are discussed in Chapter 2, which focuses on microscale tension experiments. The tensile strength results are discussed in terms of variations in microstructure and doping of polysilicon films. By virtue of a Weibull statistical analysis, the specimen size effect on the tensile strength is discussed along with an evaluation of the strength of polysilicon specimens in the absence of the initial critical defects in the as-fabricated samples.

Chapter 3 describes experimental methods and measurements of $K_{IC,eff}$. The experimental results are used to explain the role of microstructure and doping in the material's resistance to crack initiation and, under certain circumstances, also

propagation. Using stress intensity factor relations for a semi-elliptical and quarter elliptical surface cracks, the tensile strength of different polysilicon films is also estimated using the surface flaw data obtained by AFM and SEM.

Finally, Chapter 4 provides an assessment of the results obtained in this dissertation vis-à-vis the objectives stated in Chapter 1. Questions not answered in Chapters 2 and 3 are presented in the future work Section along with preliminary results on the fabrication of Chevron notch specimens from single crystal silicon in an effort to measure the K_{IC} of polysilicon's GBs under different P-doping conditions.

CHAPTER 2

Fracture Strength of Polysilicon Films

Fabrication induced microstructural changes in polysilicon can influence its strength, and thus, the reliability of freestanding MEMS devices. In this Chapter, the tensile strength of polysilicon films fabricated at a custom run at the Sandia National Laboratories is experimentally evaluated as a function of grain structure and P concentration. The results are discussed in terms of the origin of critical defects, the scalability of strength values, and the improvement in tensile strength in absence of the initial critical defects.

2.1 Materials and Fabrication

2.1.1 Specimen Preparation

Two types of 1-μm thick polysilicon specimens were fabricated by a custom polysilicon fabrication run at the Sandia National Laboratories: specimens with columnar grain size of 285 nm, and with laminated structure and grain size of 125 nm. Both (in-plane) grain sizes were determined from TEM images at the Sandia National Laboratories [41]. The grain structure of the first polysilicon type was fairly columnar and henceforth we refer to it as "columnar polysilicon", while the latter polysilicon with finer grain size is referred to as "laminated polysilicon". The grain sizes of these two types of polysilicon were smaller than the average grain size for polysilicon films fabricated by the standard SUMMiT V^{TM} microfabrication process [56], which has been reported to be in the range of 435 - 600 nm for poly1 and poly1-2 films [54,57]. A schematic of the fabrication

process for a freestanding polysilicon cantilever is shown in the Figure 2.1. The initial processing steps are identical for both microstructures: First, a 0.63 μm oxide layer was thermally grown on a silicon wafer followed by a 0.8 μm low-stress nitride layer using LPCVD. These blanket films act as electric insulating layers between the wafer and the MEMS structures. A 0.3-μm thick LPCVD polysilicon (Poly0) layer was deposited on top of the nitride layer as a ground layer. A 2 μm sacrificial oxide layer (SacOx1) of either PSG with 0.5% or 2.0% P or undoped silane glass was then deposited and patterned. Thus, each type of polysilicon was doped at two different concentration levels of P, and was also produced in undoped form. Subsequently, a 1 μm columnar polysilicon layer (Poly1) was deposited in a furnace at 580 °C.

The laminated polysilicon films were fabricated by depositing 10 alternate layers of 100-nm thick amorphous and polycrystalline silicon resulting in a 1-μm thick composite film. A second sacrificial oxide layer (SacOx2) was deposited on top of Poly1 and was chemo-mechanically planarized to a thickness of 2 μm. The wafers were then annealed in N_2 environment for 1 hr and at 1050 °C to allow for diffusion of P. In the case of laminated polysilicon, the amorphous silicon layers became polycrystalline during annealing and resulted in the laminated structure, shown in Figure 1.2(b) and Figure 2.2(a). SEM images of the cross-section of laminated and columnar polysilicon are shown in Figures 2.2(a) and 2.2(b), respectively. Notably, the surface topography of laminated polysilicon was very uniform compared to columnar polysilicon that showed significant grain growth and nucleation. Chemical analysis of the small grains shown in Figure 2.2(b) by Energy Dispersive Spectroscopy (EDS) pointed only to the presence of Si in small grains (that appear bright in the figure), as also reported by Boyce et al. [41].

The uniaxial tension specimens were 100 μm wide with a gage length of 1,000 μm. A top view of a microfabricated polysilicon tensile specimen is shown in Figure 2.2(c). Subsequently, the films were etched in 49% HF followed by supercritical CO_2 drying to obtain freestanding specimens for tension experiments. The freestanding films were anchored to the substrate at one end, while the other end was suspended with the help of fine tethers, also connected to anchors.

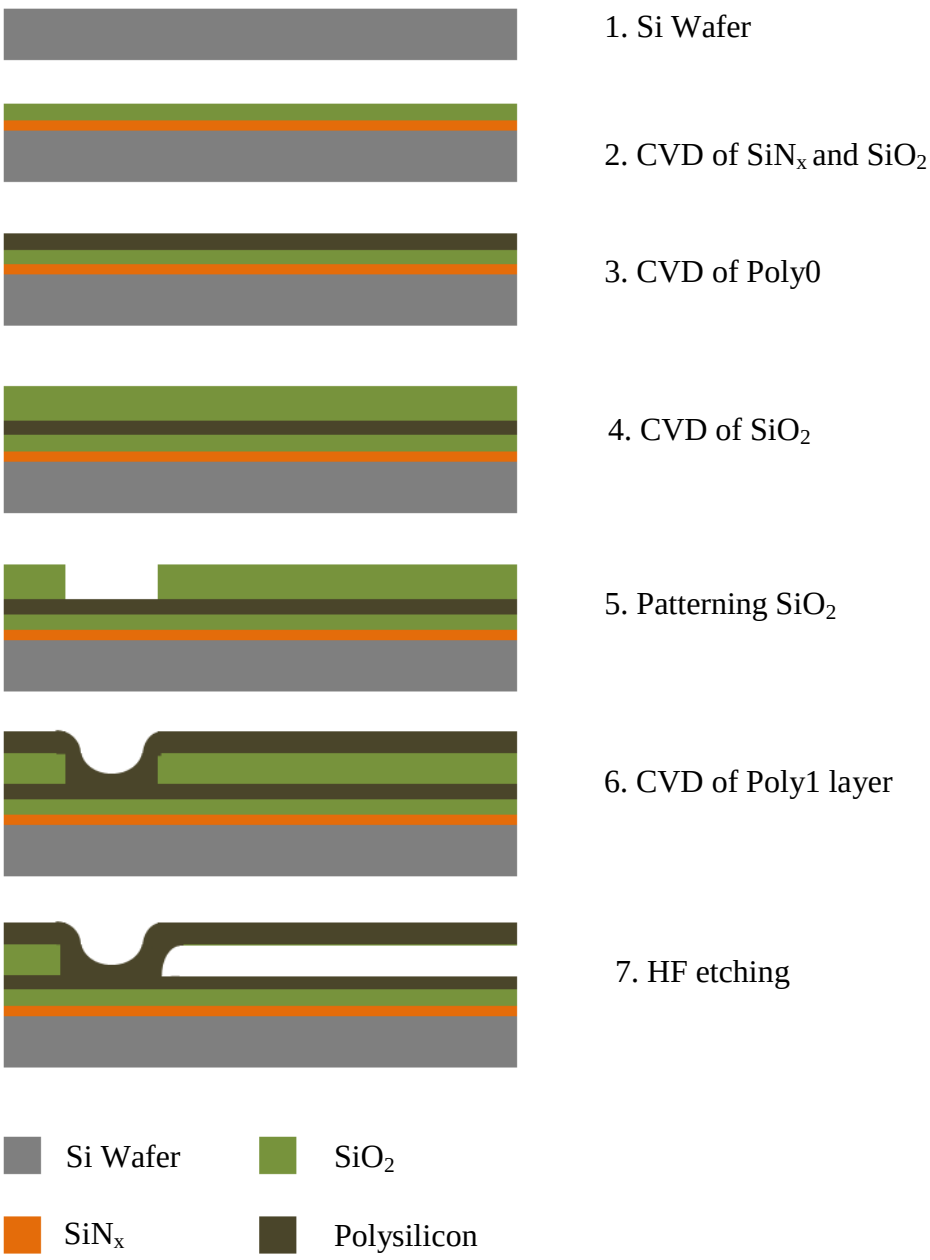

Figure 2.1. Processing steps for micromachining of freestanding polysilicon films. Redrawn from [12], Courtesy of Sandia National Laboratories, SUMMiT™ Technologies.

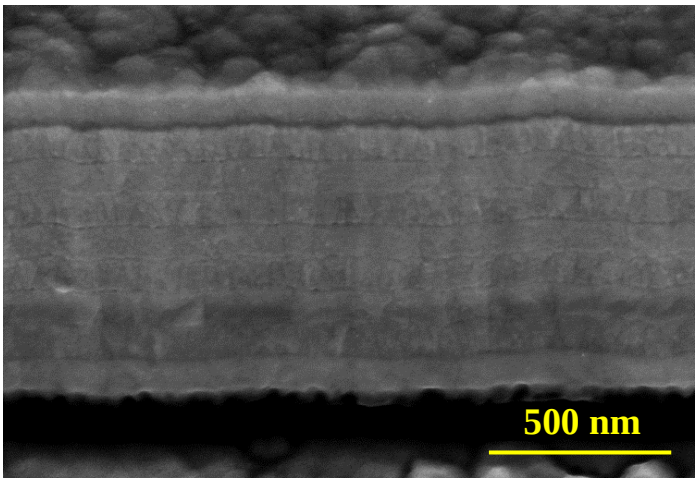

(a)

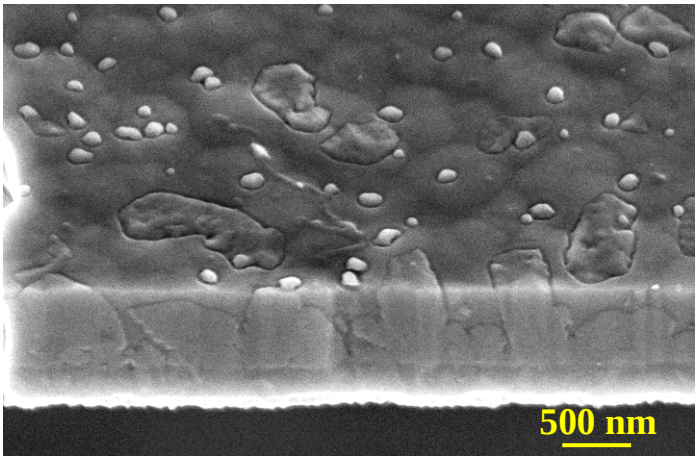

(b)

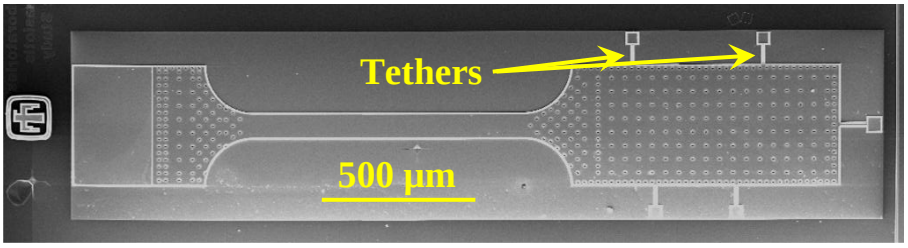

(c)

Figure 2.2 Oblique edge view of **(a)** laminated, **(b)** columnar polysilicon specimens, and **(c)** top view of a microscale specimen for uniaxial tension experiments.

2.1.2 Materials Characterization

The surface roughness of columnar and laminated polysilicon films was characterized by AFM. The average and RMS surface roughness values were calculated from 10 × 10 μm^2 surface areas obtained at three different specimen regions, and are presented in Table 2.1. The AFM topography and photodetector signal error images of undoped and heavily doped (2.0% PSG) laminated and columnar polysilicon films are shown in Figures 2.3(a-h). While the surfaces of columnar and laminated polysilicon were clearly different, the surfaces of undoped and doped polysilicon films with the same grain structure were similar. The surface morphology of laminated polysilicon films, shown in Figures 2.3(a-d), demonstrated the uniform growth of small grains of ~125 nm, whereas the surface of columnar polysilicon films shown in Figures 2.3(e-h) had larger grains of ~285 nm [41]. The top surface of columnar polysilicon contained also abnormal grains measuring more than 500 nm and in some extreme cases as much as 500 × 1000 nm^2. Chemical analysis of abnormally large grains by EDS showed the presence of only silicon atoms, as indicated by the maximum x-ray count peak at 1.74 keV in Figure 2.4. The initial peak at 0 keV is a measurement artifact not corresponding to an element. The unavailability of columnar polysilicon specimens before high temperature annealing did not allow for a definitive assessment of the origin of very large grains, which could be the result of secondary grain growth during high temperature annealing.

The average and RMS roughness values for all polysilicon films were in the range of 6-8 nm and 7-10 nm, respectively. Deep surface grooves were observed in the case of columnar polysilicon films, and in fewer occasions, in laminated films, whose effect on the mechanical strength is discussed in Chapter 3. Finally, the sheet resistance of different polysilicon films measured by the Sandia National Laboratories is presented in Table 2.2, which provides an assessment of the effectiveness of light and heavy P-doping.

Table 2.1. Surface roughness of different polysilicon films computed from three 10 × 10 μm^2 surface images obtained by an AFM.

Polysilicon	Average roughness (nm)	RMS roughness (nm)
Undoped laminated	7.7±0.5	9.5 ± 0.7
0.5% PSG laminated	6.5±0.3	8.1 ± 0.3
2.0% PSG laminated	6.4±0.2	8.0 ± 0.3
Undoped columnar	6.1±0.6	7.8 ± 0.7
0.5% PSG columnar	6.5±0.7	8.5 ± 0.6
2.0% PSG columnar	6.3±0.4	8.6 ± 0.7

Table 2.2. Sheet resistance of polysilicon films measured at the Sandia National Laboratories using a 4-point probe.

Polysilicon	Sheet Resistance (Ohms/sq)
Undoped laminated	Inf
0.5% PSG laminated	-
2.0% PSG laminated	209
Undoped columnar	Inf
0.5% PSG columnar	89240
2.0% PSG columnar	114

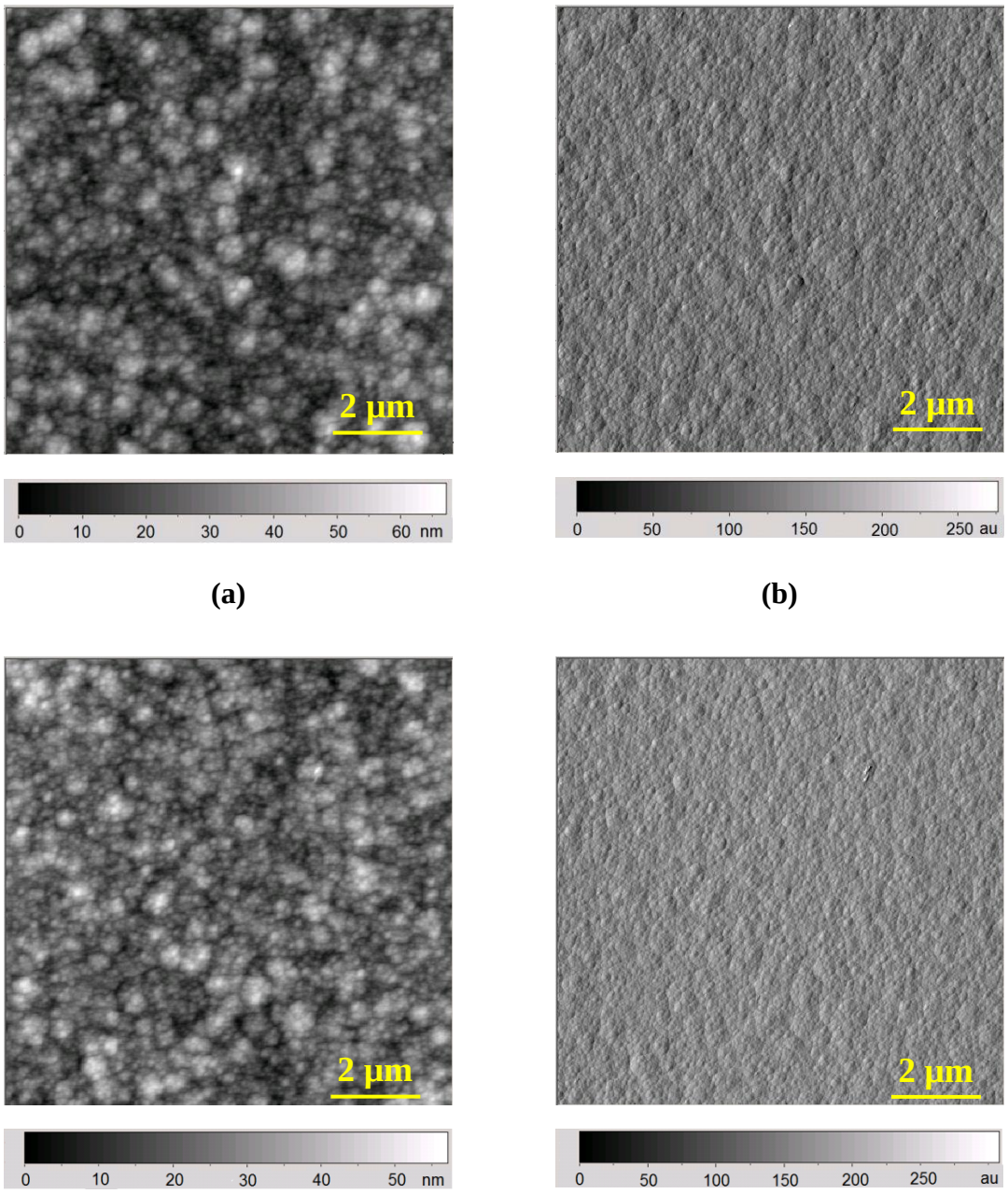

Figure 2.3 (Cont. on next page)

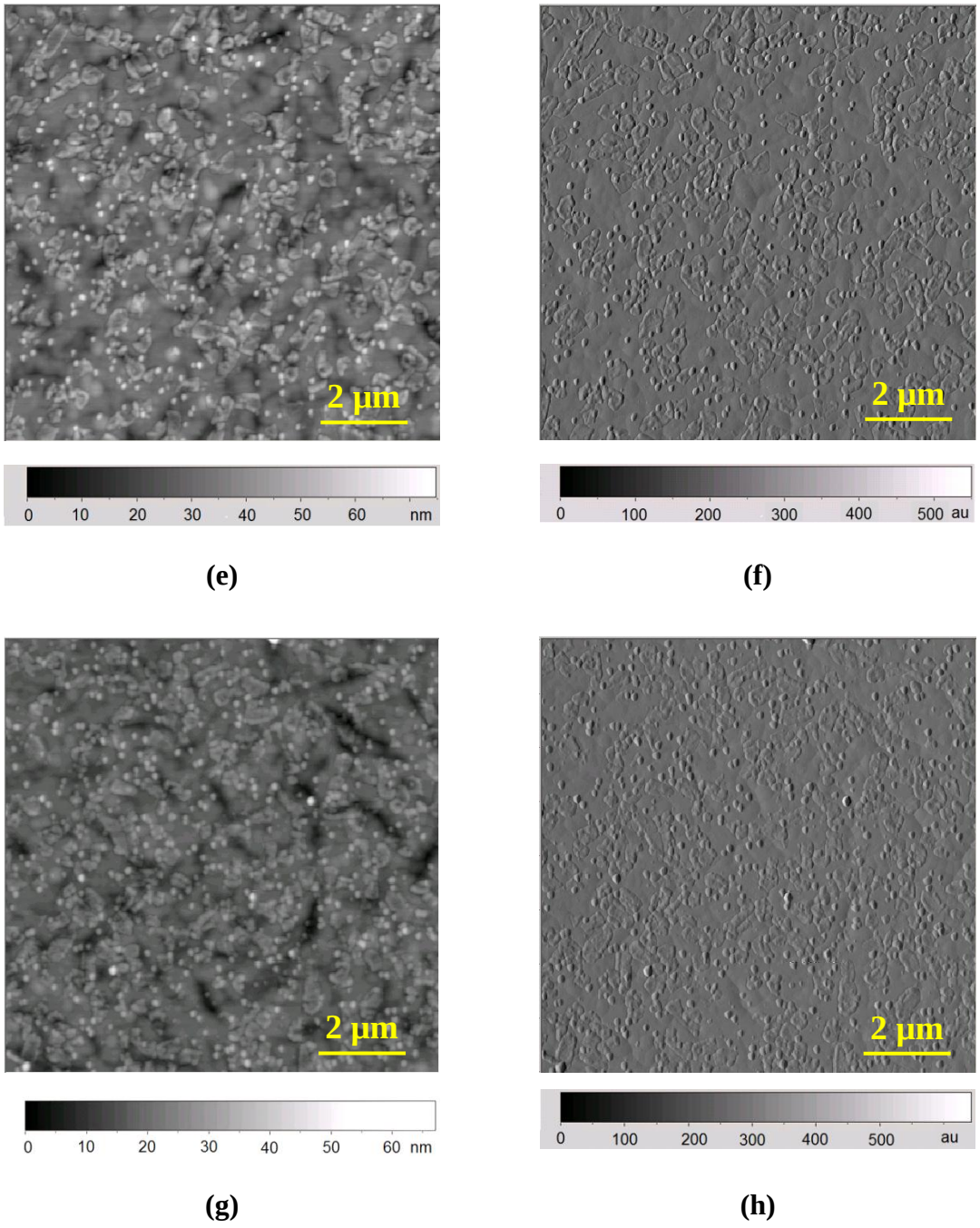

Figure 2.3. AFM topography and photodetector signal error images of **(a-b)** undoped laminated, **(c-d)** heavily doped (2.0% PSG) laminated, **(e-f)** undoped columnar, and **(g-h)** heavily doped (2.0% PSG) columnar polysilicon films.

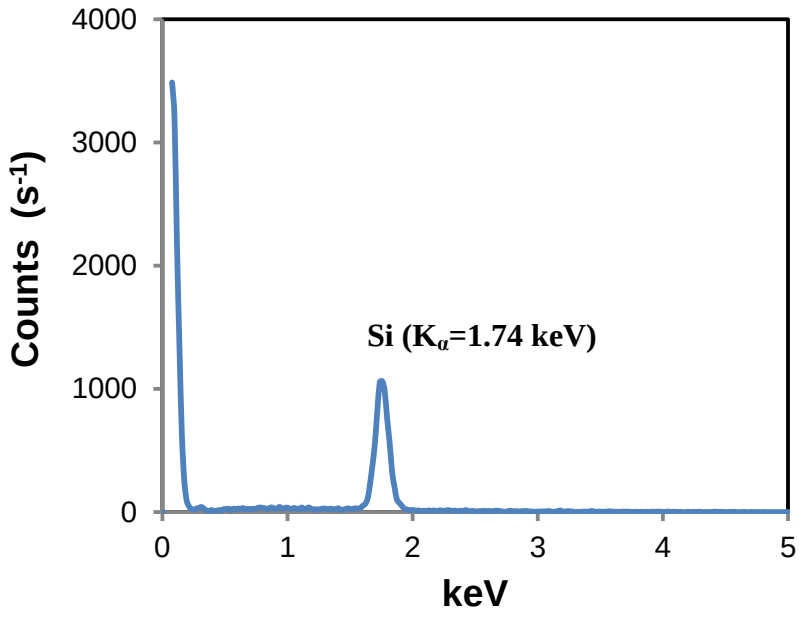

Figure 2.4. EDS spectrum of an undoped columnar polysilicon film showing the presence of only silicon atoms in abnormally large grains at the top film surface.

2.2 Experimental Methods

The apparatus for microscale uniaxial tension experiments described in [58] was employed for strength and Young's modulus measurements. As shown in Figure 2.5, it consists of a PZT actuator for loading a MEMS-scale specimen in tension and a 50g capacity loadcell to measure the force applied to the specimen. The PZT actuator and the loadcell are mounted on linear and rotational micro-positioners to control the specimen alignment. While the fixed end of a specimen is connected to the loadcell using a fixture, the freestanding end is attached to the PZT actuator using a thin glass strip bonded to it with the aid of UV curable adhesive. The tethers supporting the specimen on the silicon wafer, Figure 2.2(c), are broken using a sharp probe mounted on a 3-D micromanipulation stage. All experiments were conducted at the strain rate of 6×10^{-4} s^{-1}. The specimen thickness was measured by an SEM, and was in good agreement with the nominal values calculated using the deposition rate and times. During an experiment,

pictures of specimen surface were recorded by an optical microscope at 200× magnification and DIC analysis was performed to compute the full-field axial strain, which was plotted vs. the measured values of stress. The Young's modulus and the tensile strength were computed from the resulting stress-strain curves.

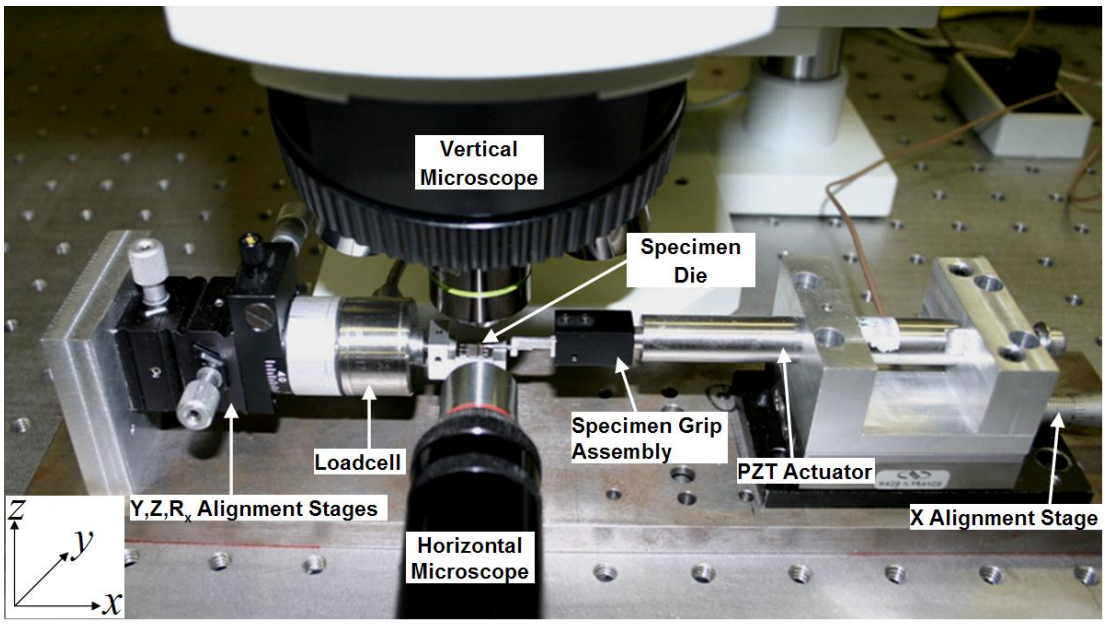

Figure 2.5. Apparatus for uniaxial tension experiments with thin film specimens [58].

2.3 Results and Discussion

The stress-strain response of all polysilicon films was linear, as shown in Figure 2.6(a-d), and the average elastic moduli were in the range of 153 – 158 GPa. These values were consistent with prior measurements in the range of 155 - 165 GPa and 165 - 175 for Sandia's SUMMiT V polysilicon [54,59] and MUMPs polysilicon [18,54,60,61], respectively. Polysilicon consists of grains with different crystallographic orientations whose elastic modulus varies in the broad range of 130 – 188 GPa [62,63] depending on the details of the grain structure. XRD analysis of laminated and columnar grain

polysilicon showed the strong presence of (111), (220), and (311) grains in the same ratio of 10:5:3, which could be the reason for the same average elastic moduli for the two types of polysilicon films.

The tensile strength and Young's modulus for columnar and laminated polysilicon thin films doped with different concentrations of P are given in Table 2.3 and plotted in Figures 2.7 and 2.8. A minimum of 15 specimens were tested for each specimen kind. The tensile strength results for as-fabricated specimens are given in Figure 2.7. The average tensile strength of columnar polysilicon was 1.31±0.09 GPa. This value is 46% lower than that of laminated polysilicon which was 2.44±0.28 GPa. Notably, while the strength of columnar polysilicon doped with 2.0% PSG dropped to 0.92±0.10 GPa, i.e. 30% lower than the undoped form, the strength of columnar polysilicon doped with 0.5% PSG was the same as the undoped material. On the contrary, the strength of laminated polysilicon did not change significantly with doping. Finally, unlike the tensile strength, the Young's modulus of polysilicon was independent of grain structure and doping level as shown in Table 2.3.

Table 2.3. Tensile strength and Young's modulus for columnar grain and laminated polysilicon doped with different concentrations of P. The average value ±1 standard deviation are presented.

Polysilicon	Tensile strength (GPa)	Young's modulus (GPa)
Undoped laminated	2.44±0.28	154.8±3.6
0.5% PSG laminated	-	-
2.0% PSG laminated	2.49±0.24	153.4±11.3
Undoped columnar	1.31±0.09	155.2±2
0.5% PSG columnar	1.30±0.12	157.0±1.2
2.0% PSG columnar	0.92±0.10	157.2±1.8

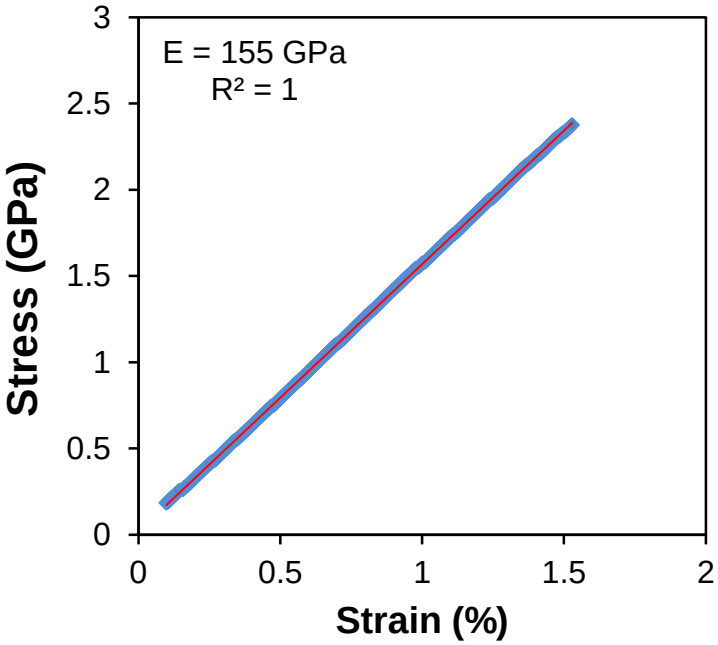

(a)

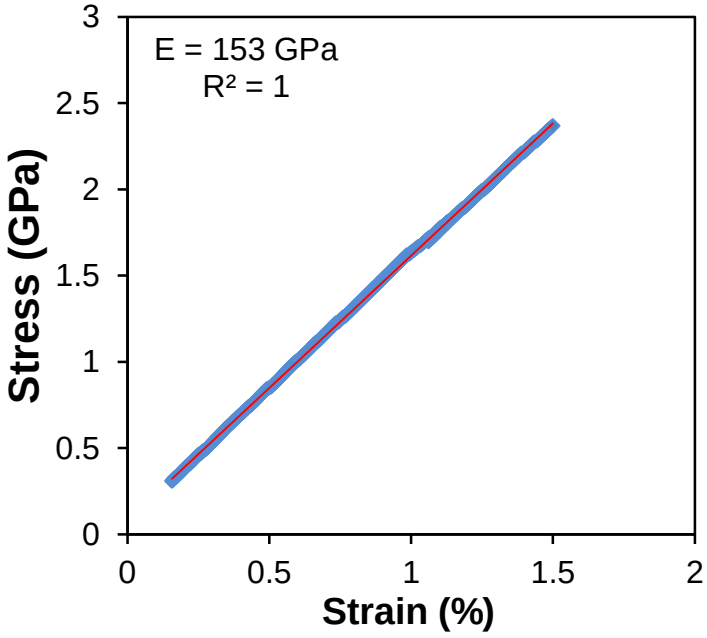

(b)

Figure 2.6 (Cont. on next page)

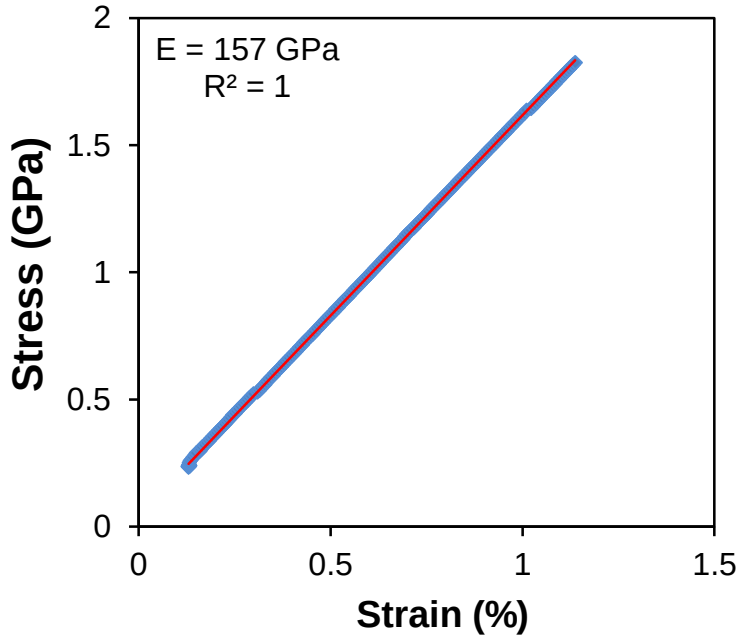

(c)

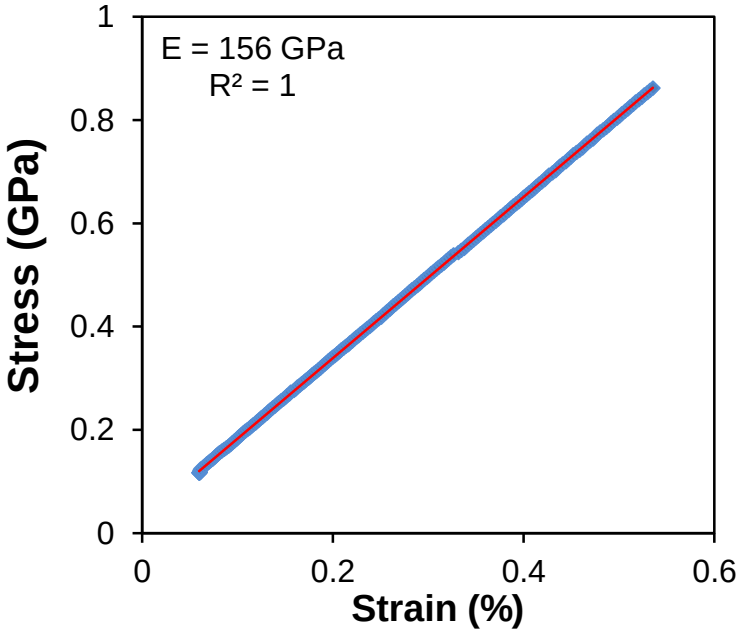

(d)

Figure 2.6. Stress vs. strain response of **(a)** undoped laminated, **(b)** 2.0% PSG doped laminated, **(c)** undoped columnar, and **(d)** 2.0% PSG doped columnar polysilicon films.

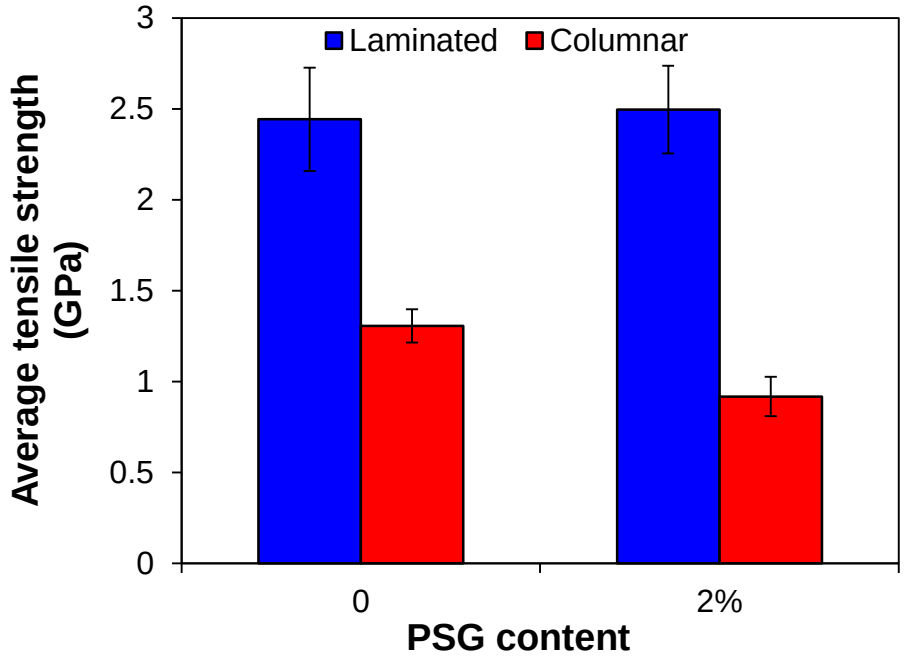

Figure 2.7. Average tensile strength of columnar and laminated undoped (0.0% PSG) and heavily doped (2.0% PSG) polysilicon. The error bars represent one standard deviation.

Due to the brittle nature of polysilicon and its high strength, the specimens shattered upon failure and hence, post fracture analysis of the failure cross-sections could not be carried out. In order to obtain insight in the process of failure initiation, a statistical analysis of the tensile strength data was carried out by using the cumulative three-parameter Weibull distribution function [15,64]:

$$P = 1 - \exp\left(-\left(\frac{\sigma - \sigma_u}{\sigma_c - \sigma_u} \right)^m \right) \tag{2.1}$$

where σ_u is the threshold stress below which no failure is expected to occur, σ_c is the characteristic stress, and m is the Weibull modulus. The probability of failure for a specimen at each stress level was computed using the following estimator [64]:

$$P_n = \frac{n - 0.5}{N} \tag{2.2}$$

where P_n is the probability of failure of n^{th} specimen and N is the total number of specimens tested. The cumulative distribution function was rewritten as

$$\ln\left(-\ln\left(1-P\right)\right) = m\ln\left(\frac{\sigma - \sigma_u}{\sigma_c - \sigma_u}\right) \tag{2.3}$$

to obtain m, σ_c and σ_u from the Weibull probability plot shown in Figure 2.8. The two parameter Weibull modulus for each polysilicon type was calculated from Equation (2.3) as the slope of the linear fit of the experimental data, as shown in Figures 2.9(a-d), after setting σ_u = 0. The characteristic strength was subsequently calculated from the Weibull modulus and the x-intercept. Using a similar approach, m, σ_c and σ_u were calculated from Equation (2.3), as shown in Figures 2.10(a-d). A summary of the computed parameters for the two and three parameter Weibull probability distributions is provided in Table 2.4.

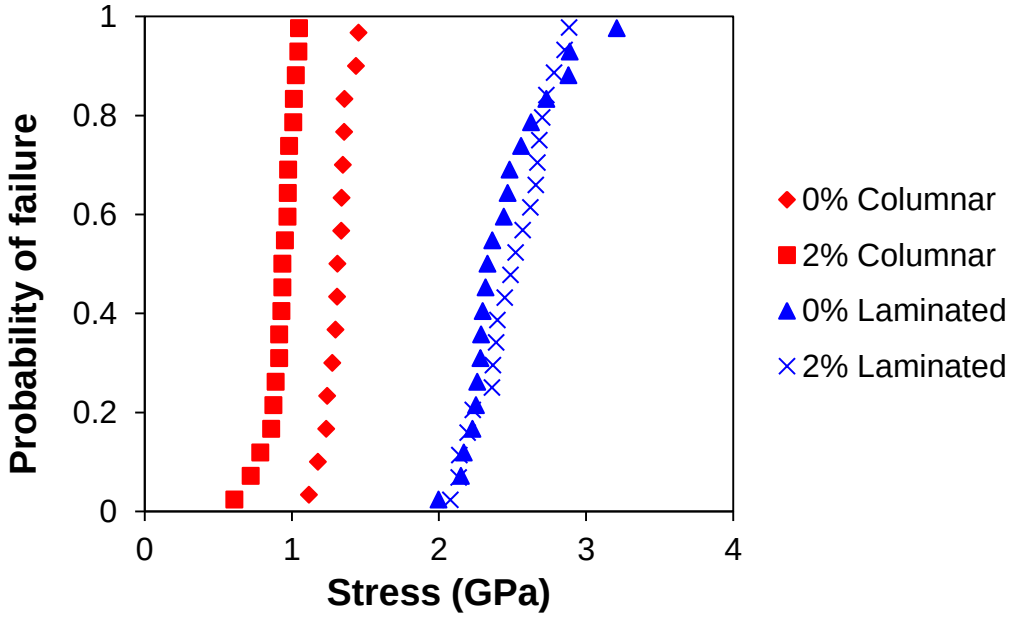

Figure 2.8. Cumulative probability of failure vs. tensile strength for columnar and laminated polysilicon films for different P-doping conditions.

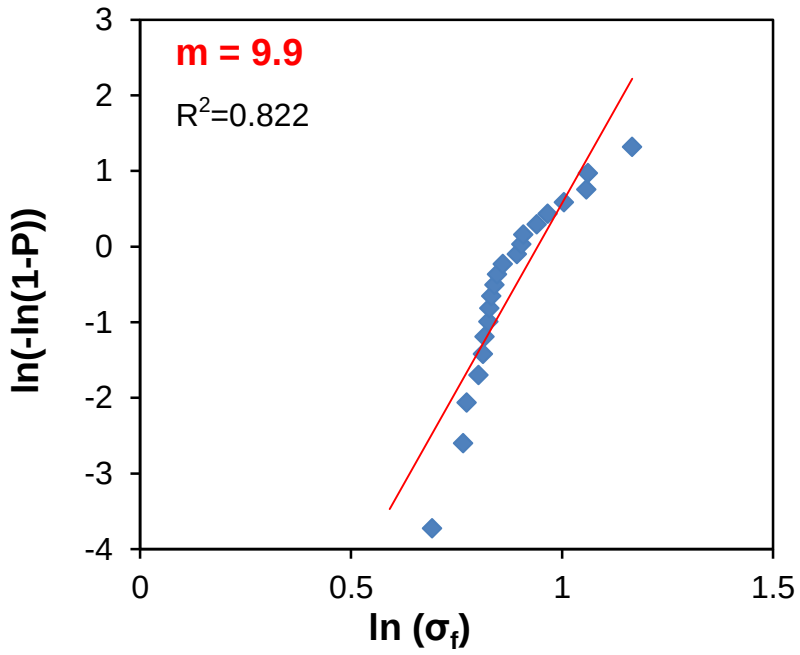

(a)

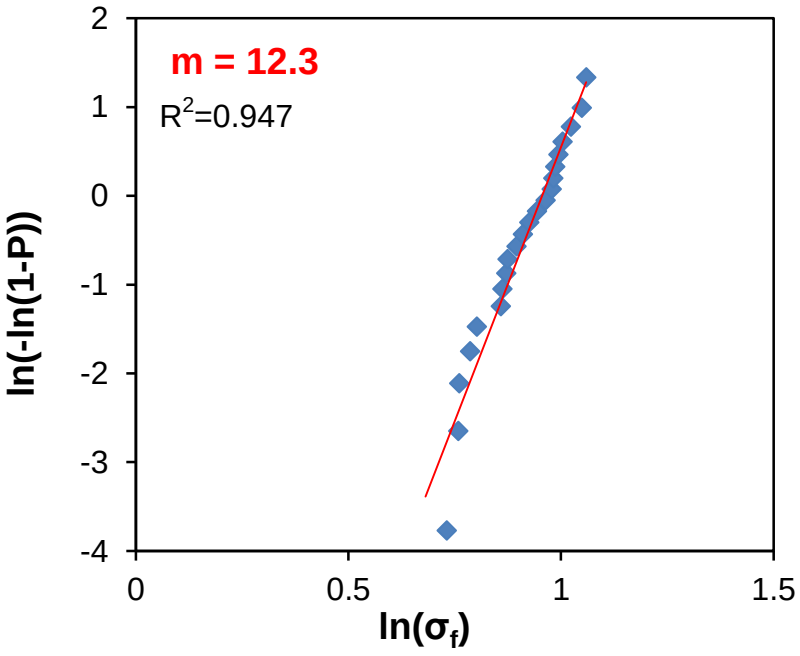

(b)

Figure 2.9 (Cont. on next page)

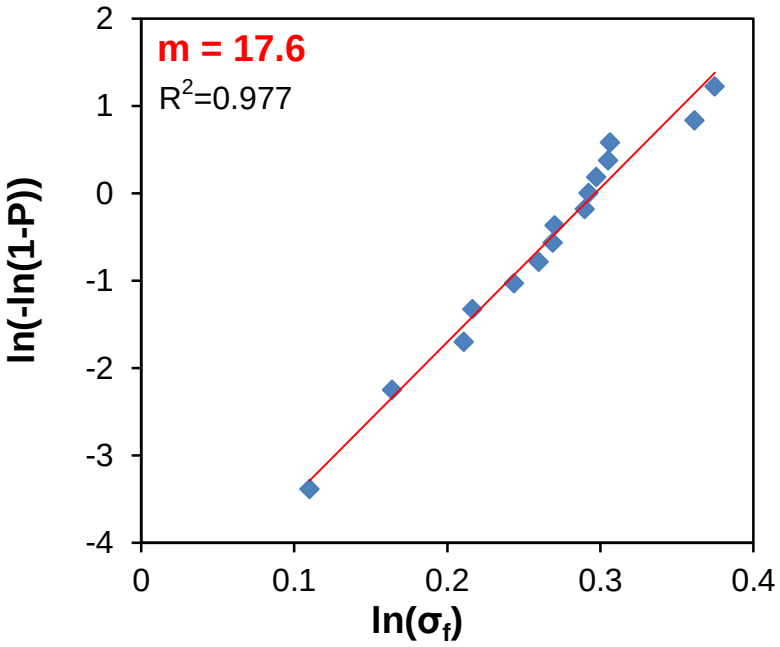

(c)

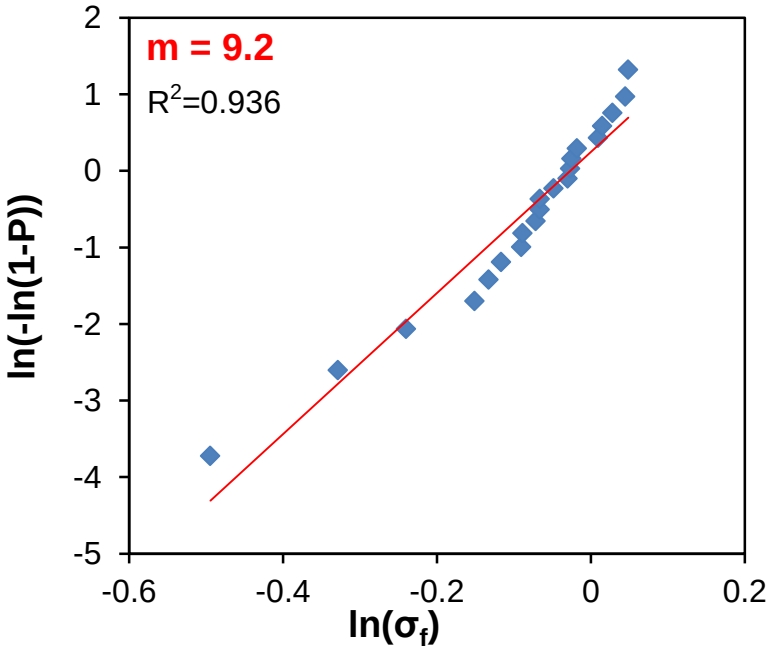

(d)

Figure 2.9. Two parameter Weibull plots for **(a)** undoped laminated, **(b)** 2.0% PSG doped laminated, **(c)** undoped columnar, and **(d)** 2.0% PSG doped columnar polysilicon.

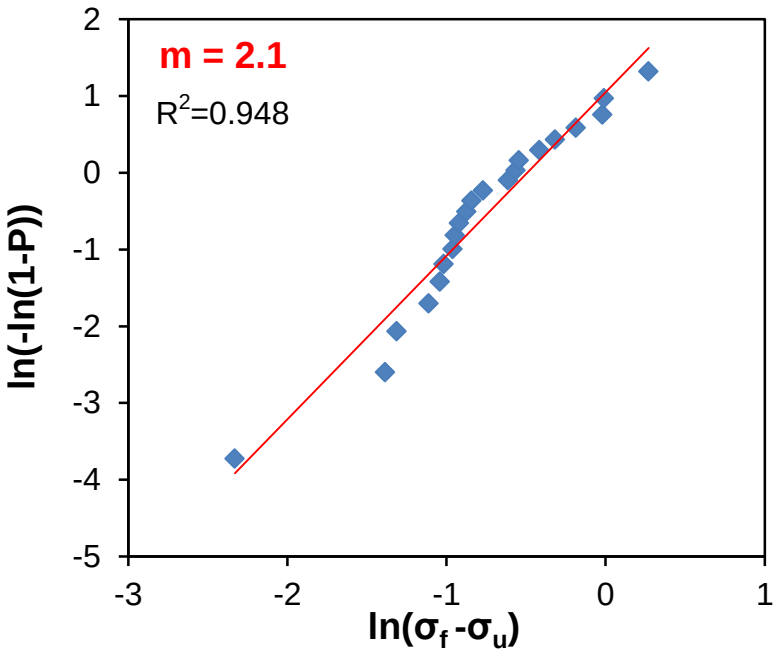

(a)

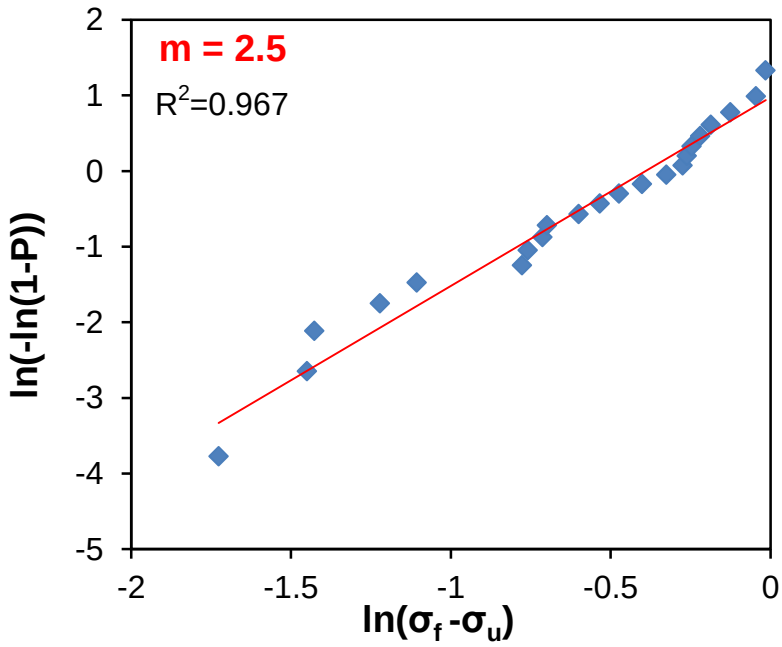

(b)

Figure 2.10 (Cont. on next page)

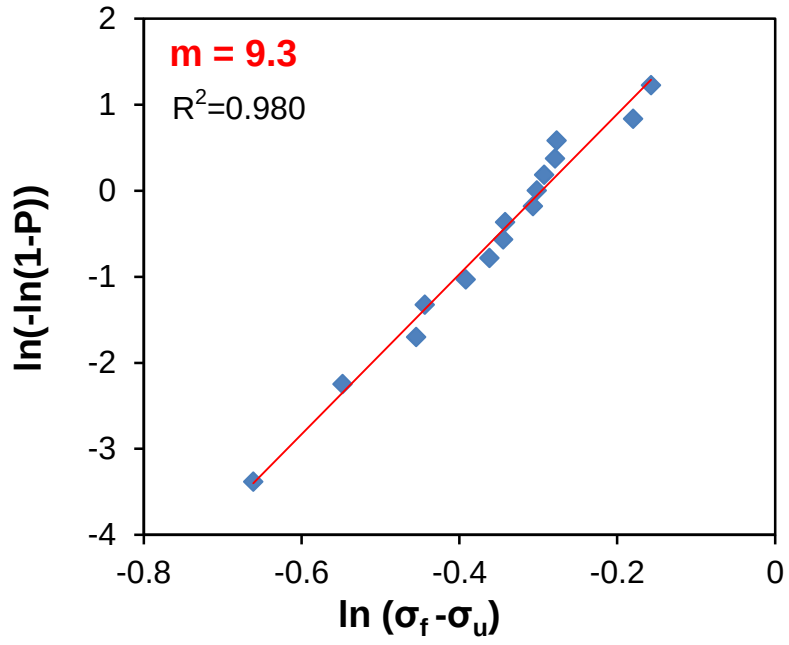

(c)

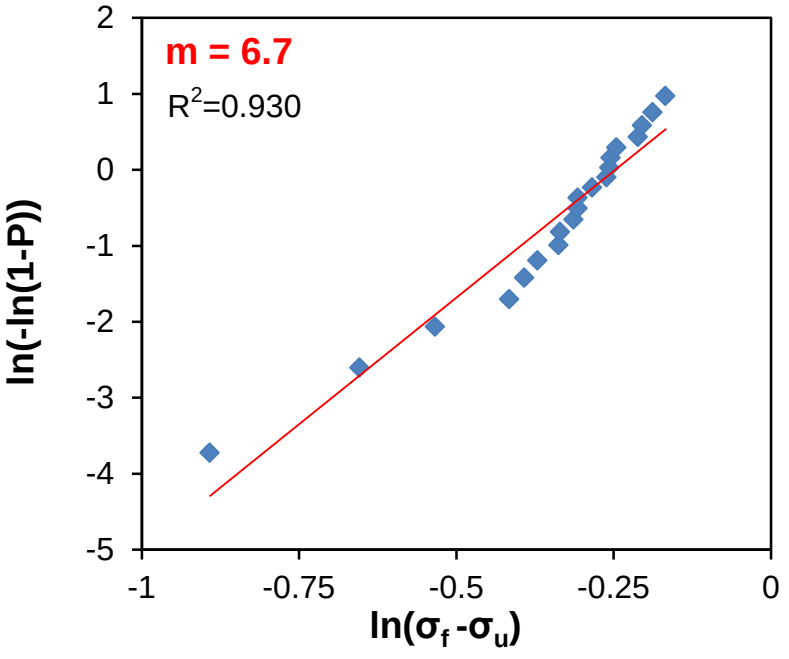

(d)

Figure 2.10. Three parameter Weibull plots for **(a)** undoped laminated, **(b)** 2.0% PSG doped laminated, **(c)** undoped columnar, and **(d)** 2.0% PSG doped columnar polysilicon.

The characteristic strengths for each specimen type calculated for the two and the three parameter Weibull cumulative distribution functions were practically the same. However, the Weibull modulus for each polysilicon type computed using a 2-parameter analysis was in the range of 9.2 - 17.6, which is quite higher than the 3-parameter Weibull moduli lying in the range of 2.1 - 9.3. The two parameter Weibull analysis provides a conservative estimate for *P*, since it assumes that σ_u = 0 GPa. On the other hand, the 3-parameter Weibull cumulative distribution function provides a more accurate assessment of the material's failure characteristics, as it computes a non-*zero* σ_u. The 3-parameter Weibull moduli of columnar polysilicon varied between 6.7 and 9.3, and were quite higher than those of laminated polysilicon, that were between 2.1 and 2.5, indicating that the defects causing failure of columnar polysilicon are quite more consistent in size and location.

Table 2.4. Characteristic strength and Weibull modulus of polysilicon specimens calculated using the two and three parameter Weibull cumulative distribution functions.

Polysilicon	2 parameter Weibull		3 parameter Weibull		
	σ_c (GPa)	*m*	σ_c (GPa)	*m*	σ_u (GPa)
Undoped laminated	2.56	9.9	2.51	2.1	1.9
2.0% PSG laminated	2.60	12.3	2.58	2.5	1.9
Undoped columnar	1.34	17.6	1.34	9.3	0.6
2.0% PSG columnar	0.97	9.2	0.98	6.7	0.2

2.4 Specimen Size Effect on Mechanical Strength

Mechanical strength is a defining metric for MEMS reliability and design. Local fracture parameters, such as the critical stress intensity factor, K_{IC}, are important in understanding and quantifying microstructural effects on fracture because they are derived from well-controlled defect geometries. Microstructurally speaking, the large (80%) difference in strength between laminated and columnar polysilicon films (2.56 vs. 1.34 GPa)is not due to substantial differences in $K_{IC,eff}$ of the two types of material, since, as reported in Chapter 3, the minimum recorded $K_{IC,eff}$ values were nearly identical. In terms of mechanical strength, the Weibull characteristic strength values of columnar and laminated polysilicon specimens were in the range of 1 - 1.3 GPa and 2.5 - 2.6 GPa, respectively. For the same polysilicon films but much smaller specimens, Boyce et al. [41] reported the characteristic strength of columnar and laminated polysilicon using a 2-parameter Weibull analysis in the range of 1.48 - 1.76 GPa and 2.80 - 2.99 GPa[1], respectively, showing that laminated polysilicon specimens are substantially stronger than columnar polysilicon. The strength values reported in their work are 15 - 35% higher than those reported here due to the 180 times smaller (~150×3.74×1 μm^3) specimens they used. Table 2.5 and Table 2.6 compare the results using a 2 and 3-parameter Weibull analysis of the polysilicon specimens tested in this work and in [41]. The strength of brittle materials depends on the size of the specimens tested. Increasing the specimen size enhances the probability of larger critical flaws present in a specimen and reduces the measured strength. Increasing specimen size also increases the statistical probability of critical flaws and, as a result, the value of the Weibull modulus, m. As expected, the characteristic strength of both columnar and laminated polysilicon decreased with increasing specimen size. Meanwhile, the range of Weibull moduli for columnar and laminated polysilicon derived by using a 2-parameter analysis increased from 8.6 - 12.9 to 9.2 - 17.6 indicating that the critical flaws were more evenly distributed in larger specimens. The Weibull moduli of larger specimens derived by using a 3-parameter analysis were also higher than those for smaller specimens, except in the case of undoped laminated polysilicon.

[1] The value of 2.99 GPa for the characteristic strength of 2.0% PSG doped laminated polysilicon was computed from the Weibull plots in reference [41].

Table 2.5. Characteristic strength and modulus of the two parameter Weibull cumulative distribution function calculated in this work and by Boyce et al. [41].

Polysilicon	This work 1000×100×1 μm^3		Boyce et al. [41] 150×3.75×1 μm^3	
	σ_c (GPa)	m	σ_c (GPa)	m
Undoped laminated	2.56	9.9	2.80	8.6
2.0% PSG laminated	2.60	12.3	2.99	9.8
Undoped columnar	1.34	17.6	1.76	12.9
2.0% PSG columnar	0.97	9.2	1.48	8.7

Table 2.6. Characteristic strength, threshold stress, and modulus of the three parameter Weibull cumulative distribution function calculated in this work and for the data by Boyce et al. [41].

Polysilicon	This work 1000×100×1 μm^3			Boyce et al. [41] 150×3.75×1 μm^3		
	σ_c (GPa)	m	σ_u (GPa)	σ_c (GPa)	m	σ_u (GPa)
Undoped laminated	2.51	2.1	1.9	2.79	4.1	1.3
2.0% PSG laminated	2.58	2.5	1.9	3.05	1.9	2.1
Undoped columnar	1.34	9.3	0.6	1.74	2.5	1.3
2.0% PSG columnar	0.98	6.7	0.2	1.46	4.1	0.7

The consistency of the Weibull parameters extracted from the two specimen sizes in this work and in [41] was evaluated using the Weibull statistics:

$$\sigma_{c,1} = \sigma_{c,2}\left(\frac{A_2}{A_1}\right)^{\frac{1}{m_2}} \tag{2.4}$$

$$\sigma_{c,1} = \sigma_{c,2}\left(\frac{V_2}{V_1}\right)^{\frac{1}{m_2}} \tag{2.5}$$

The characteristic strength of large specimens was estimated using the Weibull parameters measured from small specimens and *vice versa*, assuming that the critical flaws are distributed in **(a)** the sidewall surface area, and **(b)** the specimen top surface area. Given that the specimen thickness was 1 μm for both the small and the large specimens, the Weibull analysis using the sidewall surface area as the location of critical flaws is equivalent to an analysis based on the specimen length or a specimen edge length, while the analysis using the specimen top surface area as the location where the critical flaw population resides is also equivalent to an analysis based on volumetric flaws. On the other hand, due to the constant film thickness, the latter analysis could not really distinguish between volumetric and top surface area critical flaws. The bar charts in Figures 2.11(a,b) show that the Weibull size effect for laminated polysilicon specimens is governed by critical defects residing on or along the specimen sidewall surface, as the σ_c of large specimens is closely predicted from experimental data from small specimens and *vice versa*. In the case of columnar polysilicon, an analysis using the sidewall area (or equivalently the specimen length) and specimen top surface area (or equivalently the specimen volume) resulted in equally good agreement between the two data sets, as shown in Figures 2.11(a-d). However, the SEM images shown in Section 2.5 prove that the specimen size effect for columnar polysilicon originated in critical defects residing at the specimen's sidewalls. Therefore, Weibull scaling predictions must be corroborated with direct observations of the geometry and location of the critical flaws in order to obtain unequivocal conclusions.

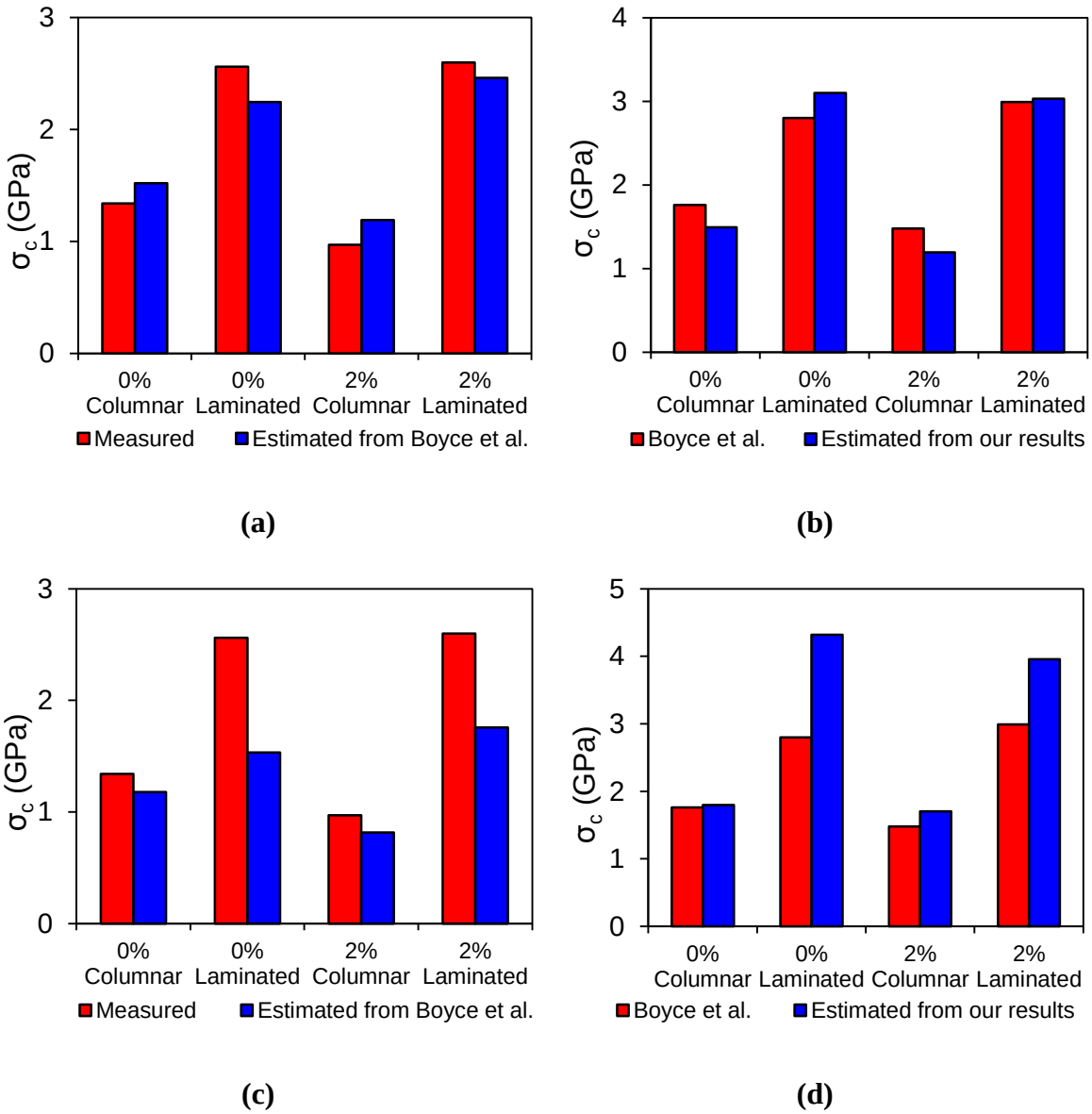

Figure 2.11. Estimates of characteristic strength of large and small specimens using data from small and large specimens, respectively, assuming that all critical flaws lie in the **(a-b)** sidewall area, and **(c-d)** top surface area. The data for Boyce et al. are from reference [41].

2.5 The Role of Grain Structure and Doping on Tensile Strength

The Weibull-based analysis conclusions were further corroborated by AFM and SEM images of the specimen top and sidewall surfaces of columnar and laminated polysilicon specimens. Based on AFM images in Figures 2.3 (a-h), the top surface RMS, average peak-to-valley, and maximum peak-to-valley roughness of laminated polysilicon were nearly the same, and 12% and 26% lower than columnar polysilicon, respectively. Such relatively small variations in average values of the surface roughness do not entirely explain the large difference in tensile strength between the two types of polysilicon. Instead, one must look for individual defects on specimen surfaces such as those shown in Figures 2.12(a,b) for columnar polysilicon. Such large flaws must originate in post processing such as RIE, high temperature annealing or sacrificial etching, as any defects formed during deposition of polycrystalline silicon are expected to be quite small in size. The large sidewall flaws were all located at the top edge of specimen and were always associated with severe GB grooving of large grains in columnar polysilicon. Notably, this GB grooving occurred by GB pitting, Figures 2.13(a,c), which, although was present on the entire specimen surface of 2.0% PSG doped columnar polysilicon, Figure 2.13(a), it was most detrimental at the specimen sidewalls. On the contrary, the sidewall and the top surfaces of laminated polysilicon were smooth, as shown in Figure 2.12(c), without evident GB grooves. However, the undoped and 2.0% PSG doped laminated polysilicon possessed a 100 nm deep step along the entire edge of the top and bottom surfaces, as shown in Figure 2.14(a). Although the top surface step did not contain any discernible defects, the bottom step contained a continuous stream of pores and voids, Figure 2.14(b), which could be the source of failure initiation in laminated polysilicon, since all other flaws identified by SEM imaging were not as severe.

GB grooving was dramatically more pronounced for P-doped columnar polysilicon, as shown in Figures 2.13(a) and 2.15. Contrary to the small effect on $K_{IC,eff}$, as discussed in Chapter 3, heavy doping (2.0% PSG) had significant impact on the tensile strength of columnar polysilicon specimens, causing a reduction of 30% compared to undoped polysilicon. On the contrary, lightly doped (0.5% PSG) columnar polysilicon specimens exhibited the same tensile strength as those of undoped, which provides a path

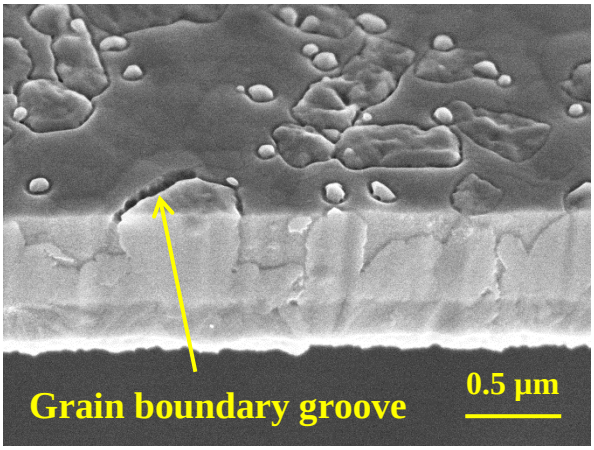

(a)

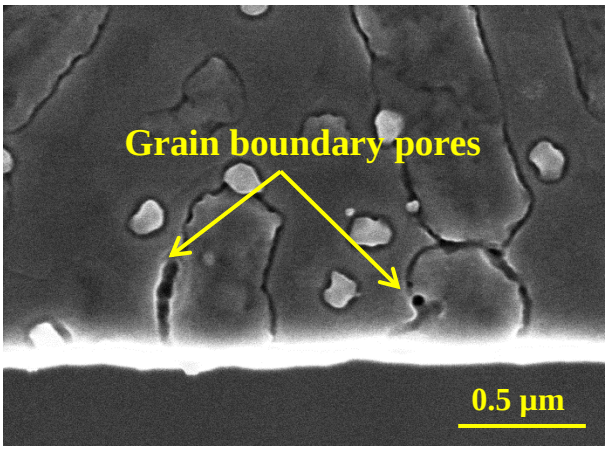

(b)

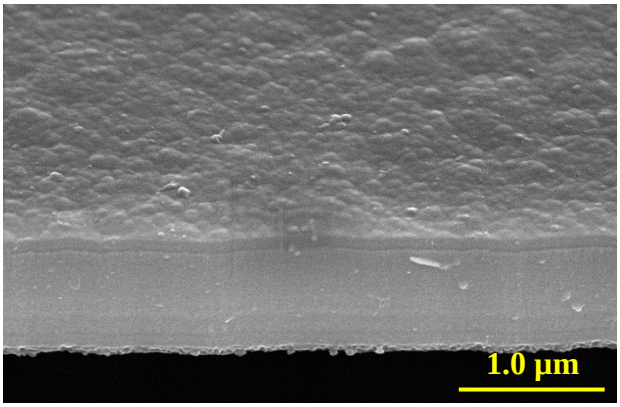

(c)

Figure 2.12. (a) Oblique and **(b)** top surface view of undoped columnar polysilicon, and **(c)** undoped laminated polysilicon specimens.

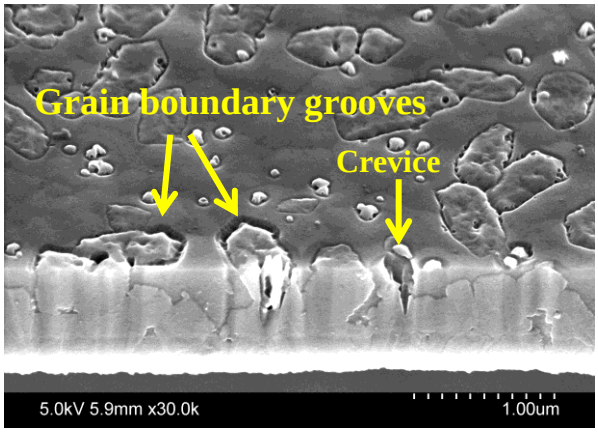

(a)

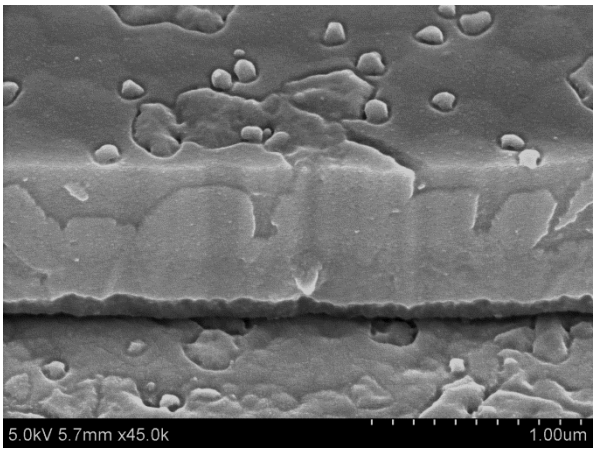

(b)

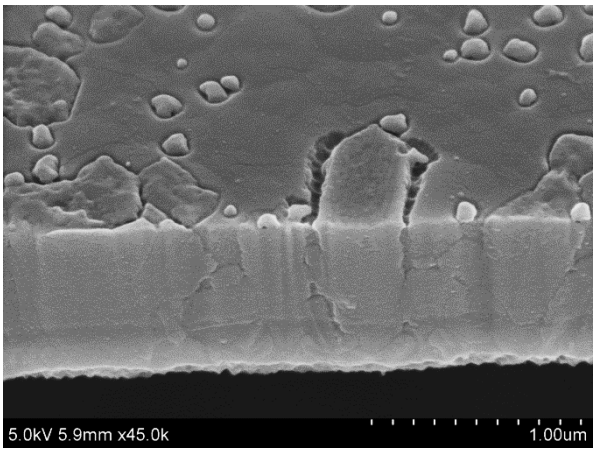

(c)

Figure 2.13. Oblique view of **(a)** 2.0% PSG doped, **(b)** 0.5% PSG doped, and **(c)** undoped columnar polysilicon, after sacrificial etching by 49% HF.

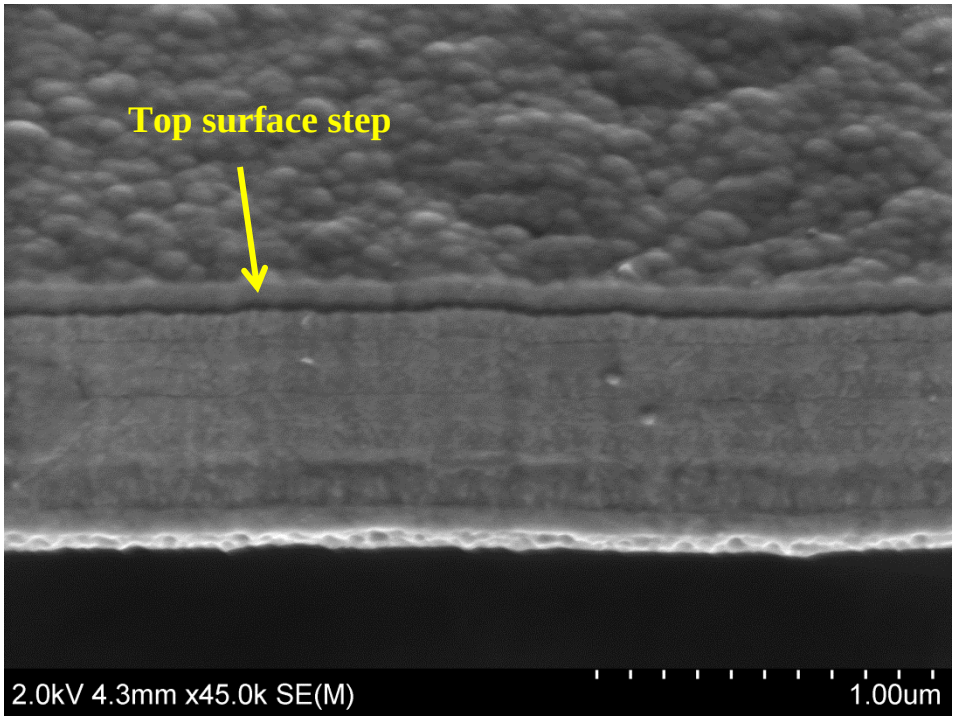

(a)

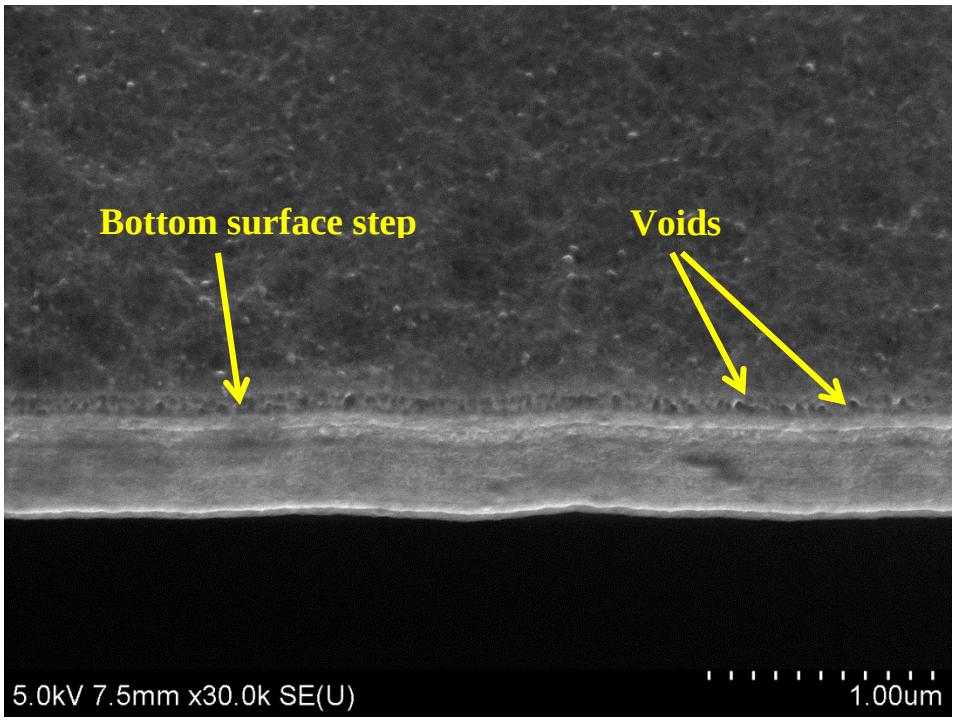

(b)

Figure 2.14. SEM images showing steps present at the edge on **(a)** top, and **(b)** bottom surface of 2.0% PSG doped laminated polysilicon.

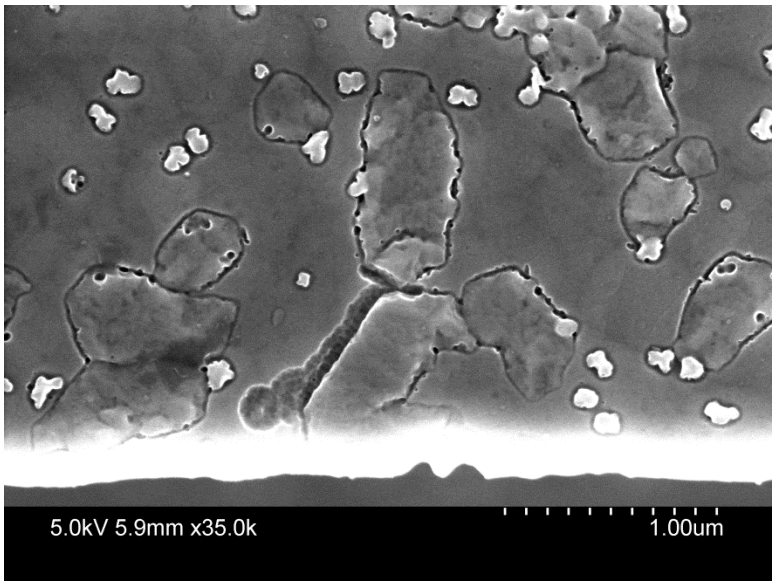

Figure 2.15. Top surface of 2.0% PSG doped columnar polysilicon showing voids and severe GB grooving near the specimen sidewall.

towards benign polysilicon doping. Heavily P-doped polysilicon was characterized by deep crevices and GB grooves at the top edge of the specimen sidewalls, Figure 2.13(a), notably larger than any sidewall ridges that commonly form due to RIE. These sidewall edge crevices were much less pronounced in the lightly doped and undoped specimens shown in Figures 2.13(b,c), which had virtually identical sidewall morphology and hence tensile strength.

While defects in a material can originate in various processing steps, such as CVD, RIE, doping, and annealing, the defects in Figures 2.12(a,b), 2.13(a-c), and 2.15 are not related to polysilicon film deposition or growth since they are present only at the top sidewall surfaces. It is possible that RIE applied to pattern the blanket columnar polysilicon films produced minor grooves at certain GBs, as shown in Figures 2.12(a) and 2.13(b,c). However, such grooves did not exist in any of the laminated polysilicon specimens. A potential explanation lies with the details of the fabrication method of laminated polysilicon films, where the last deposited 100-nm layer was amorphous silicon and remained as such during RIE patterning, only to crystallize during subsequent

annealing. While this could explain the shallow GB grooves near the free specimen edges of undoped and lightly doped columnar polysilicon, the deep crevices and notches at the sidewalls of 2.0% PSG doped columnar polysilicon must have developed during subsequent fabrication steps, including sacrificial etching by 49% HF, which is known to cause GB grooving in polysilicon under specific conditions [37,43]. It is also plausible that the shallow GB crevices in undoped columnar polysilicon served as initial locations for the formation of the deeper crevices along the edges of heavily doped columnar polysilicon specimens. While it has been shown that prolonged etching of polysilicon in 49% HF causes porosity and micro-cracks in the presence of a Au top layer [16,17,39], this mechanism does not entirely explain the formation of such deep crevices only at sidewalls. Specimens etched in 49% HF for very short times that were sufficient to etch only the top 2-μm sacrificial oxide still contained sidewall defects similar to those shown in Figure 2.13(a), which implies that prolonged sacrificial etching was not responsible for those serious crevices. To confirm this point, freestanding heavily doped columnar polysilicon films were additionally exposed to 49% HF for 30 min and 60 min and the top and sidewall surfaces were imaged by an SEM before and after each etching cycle, as shown in Figures 2.16(a-c). The specimen edges that were exposed to 49% HF were fracture cross-sections derived from the fracture experiments described in Chapter 3. As shown in Figure 2.16(c), there were no signs of GB etching at the top specimen surface and the fracture surface, even after the very prolonged exposure of 60 min to 49% HF.

Therefore, it emerges that large sidewall edge defects near the GBs in 2.0% PSG doped columnar polysilicon could have evolved from the smaller edge defects in undoped RIE patterned polysilicon films, during concurrent high temperature annealing and P-doping[2]. According to Robertson [65], GB grooving occurs in polysilicon at high temperatures due to self-diffusion of silicon at GBs into adjacent grains. It has been shown that very minimal grain growth occurs in undoped polysilicon during annealing over 1000 ºC, which, however, increases with the addition of P dopant [33,34]. In the

[2] The frequency of large GB specimen edge defects in 2.0% PSG doped columnar polysilicon was considerably higher than that in undoped polysilicon.

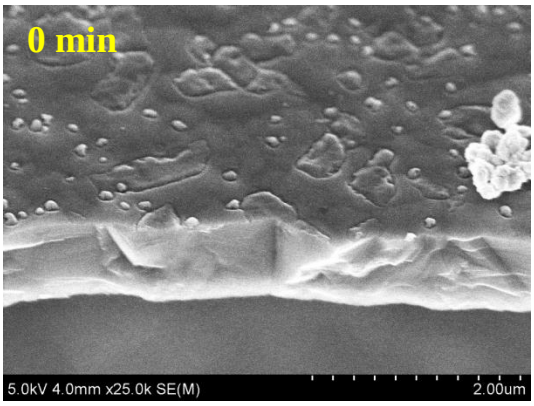

(a)

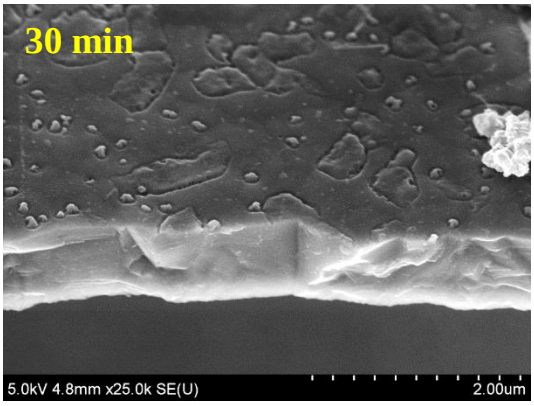

(b)

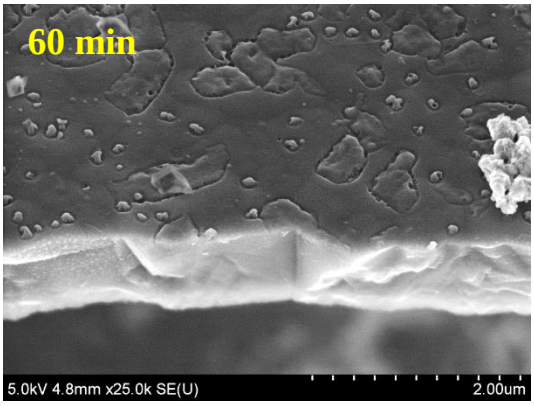

(c)

Figure 2.16. Oblique view of a fractured 2.0% PSG doped columnar polysilicon specimen **(a)** before, and after exposure to 49% HF for **(b)** 30 min, and **(c)** 90 min. No degradation was observed at the specimen top surface or the fracture surface as a result of the prolonged exposure to 49% HF.

present study, the freestanding undoped columnar polysilicon films were additionally annealed at 1100ºC for 1 hr in N_2 atmosphere. Inspection by an SEM showed no signs of grain growth or formation of GB grooves at the specimen free edges, as shown in Figure 2.17. This result further supports the possibility that the GB grooves in undoped and 0.5% PSG doped columnar polysilicon formed during the RIE process. While Wada and Nishimatsu [34] saw limited grain growth in polysilicon with P concentrations of 2.5×10^{20} atoms/cm^3, a remarkable increase in grain growth occurred for polysilicon doped with 7.5×10^{20} P atoms/cm^3. A critical concentration of P for enhanced grain growth in polysilicon has been reported to be ~4×10^{20} atoms/cm^3. In the present study, the concentration of P in 0.5% PSG and 2.0% PSG was estimated to be 2.25×10^{20} atoms/cm^3 and 9×10^{20} atoms/cm^3, respectively. During annealing of heavily doped (2.0% PSG) columnar polysilicon, significant concentration of P diffused into polysilicon GBs, especially at GBs near the sidewalls due to diffusion from the top and the lateral surfaces. PSG with high concentration of P reflows at temperatures over 900 ºC. PSG is a mixture of silicon dioxide (SiO_2) and phosphorus pentoxide (P_2O_5) forming during CVD as a result of the reaction between silane (SiH_4), oxygen (O_2), and phosphine gas (PH_3) [31,32]:

$$SiH_4 + O_2 \rightarrow SiO_2 + 2H_2$$

$$4PH_3 + 5O_2 \rightarrow 2P_2O_5 + 6H_2$$

During annealing, phosphorus pentoxide (P_2O_5) undergoes a reduction reaction with Si to form SiO_2 and P [66,67]:

$$2P_2O_5 + 5Si \rightarrow 2SiO_2 + 4P$$

It is, therefore, plausible that the reduction reaction of P_2O_5 resulted in increased formation of SiO_2 at GBs. When the sacrificial oxide layer is etched by a 49% HF aqueous solution, the newly formed SiO_2 at GBs was also etched away resulting in pores and grooves near GBs, as shown in Figure 2.15. Due to the high P content at the GBs near sidewalls, the formation of deeper grooves was significantly enhanced in this region. The pores and deep crevices were more pronounced in columnar polysilicon doped with

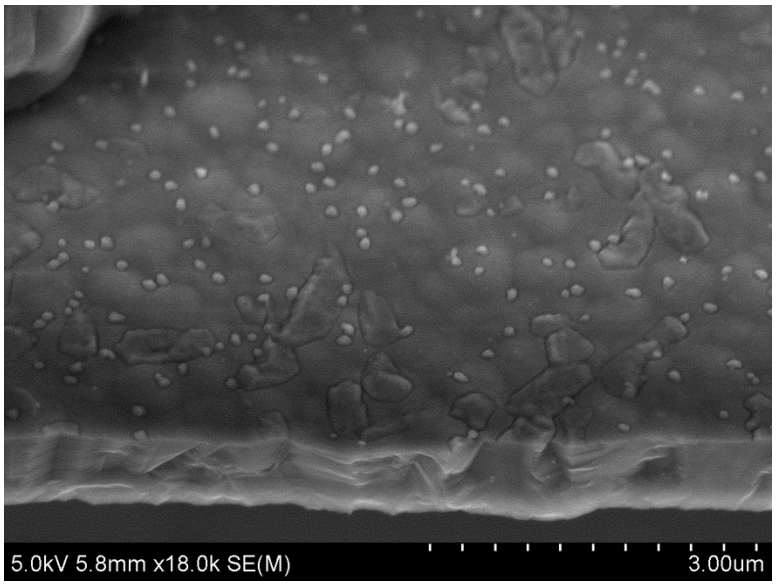

(a)

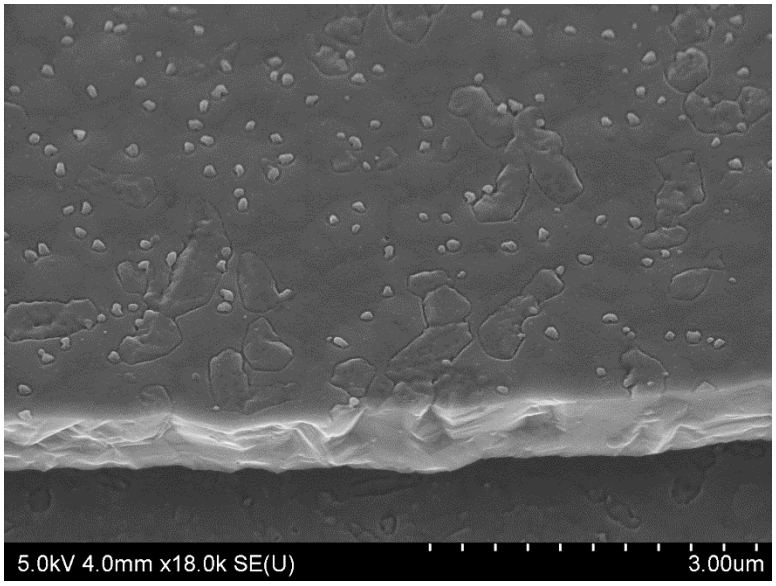

(b)

Figure 2.17. A fractured film of undoped columnar polysilicon **(a)** before, and **(b)** after additional annealing at 1100 ºC for 1 hr in N_2 atmosphere. No GB grooves were observed at the specimen free edges as a result of thermal annealing.

2.0% PSG, whereas such large defects were not found in undoped and 0.5% PSG columnar polysilicon. Thus, P-doping beyond a critical concentration exacerbated edge defect formation during high temperature annealing.

Such large specimen edge defects were not observed in heavily doped laminated polysilicon, whose tensile strength was 2.49±0.24 GPa and was unaffected by doping. The presence of an amorphous top layer during RIE and the lack of GBs at the top film surface deterred the formation of the GB grooves seen at the specimen edges of undoped and lightly doped (0.5% PSG) columnar polysilicon. The top specimen surface was evenly and uniformly doped during high temperature annealing with a PSG overlayer, which averted the formation of high density P regions at GBs and surface grooving.

2.6 Strength of Columnar Polysilicon with Defect-free Sidewalls

The catastrophic flaws on the specimen edges of columnar polysilicon potentially could be eliminated with selective etching of sidewalls using an isotropic etchant such as HF/nitric/acetic acid (HNA) and tetramethylammonium hydroxide solution (TMAH) [31], or by an additional oxidation step of the specimen edge and subsequent etching of the oxide. While these options were not possible for the available specimens, the sidewalls of the microscale uniaxial tension specimens in Figure 2.2(c) were trimmed by a Focus Ion Beam (FIB) in order to quantify the strength of columnar polysilicon in the absence of large sidewall defects. The specimen edges were ion milled using 7 nA probe current to obtain smooth sidewalls, as shown in Figures 2.18(a,b). Subsequently, the sacrificial oxide layer was etched in 49% HF to obtain freestanding specimens for mechanical testing. A comparison between as-fabricated and ion beam trimmed sidewalls is provided in Figures 2.13(a), 2.15 and 2.18(b). The strength of columnar and laminated polysilicon specimens with smooth sidewalls is compared with that of as-fabricated polysilicon specimens and as a function of doping in Figure 2.19. The average tensile strength of columnar polysilicon with ion beam milled sidewalls was in the range of 1.9 -

2.2 GPa, i.e. 70 - 100% higher than that of as-fabricated columnar polysilicon. However, the average strength of laminated polysilicon with ion beam milled sidewalls was in the range of 2.2-2.4 GPa which is 10 - 15% lower than as-fabricated specimens. This

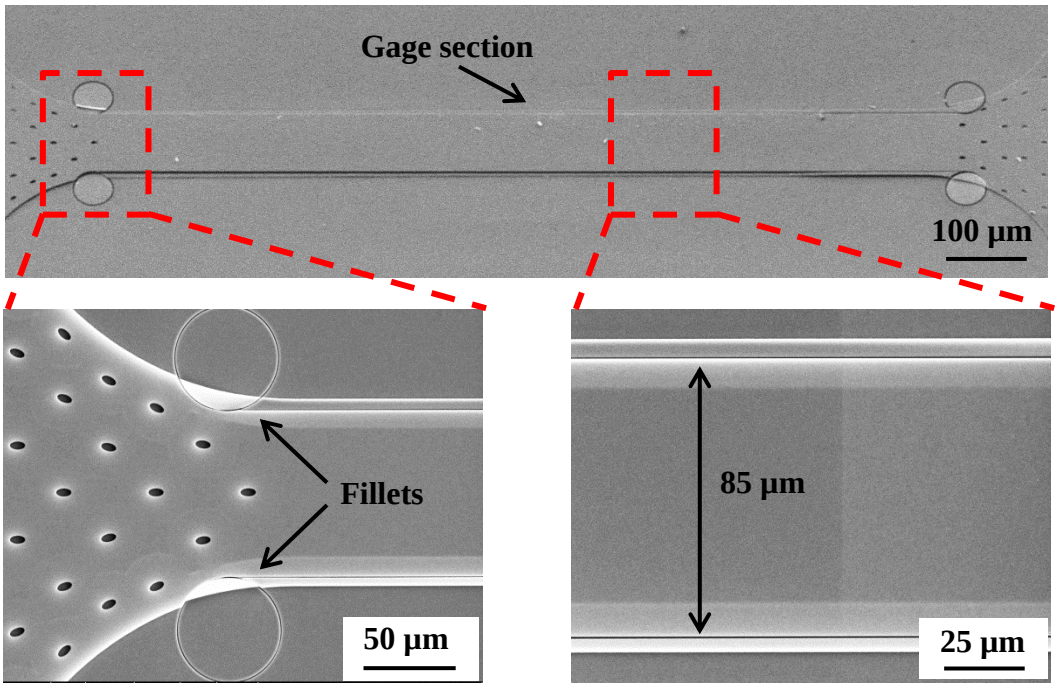

(a)

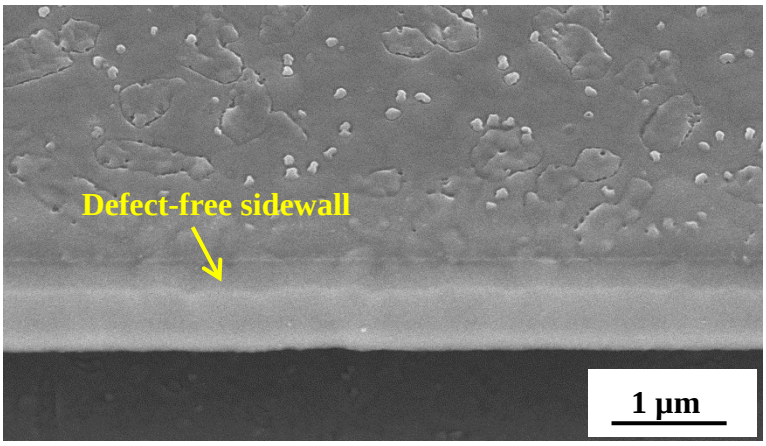

(b)

Figure 2.18. (a) SEM images of an ion beam milled specimen by a FIB showing the gauge section, the round fillets at the gauge ends, and the trimmed specimen edges. **(b)** Oblique view of sidewall after ion beam milling.

indicates that the tensile strength measured from polysilicon specimens with ion milled sidewalls was limited by material damage caused to the specimen sidewalls during ion milling, as shown in Figures 2.20 - 2.22. Polycrystalline silicon near the ion beam milled specimen sidewalls became partly amorphous due to ion beam induced damage, as shown in Figure 2.20(a). Additionally, the ion beam milled sidewalls had rounded and tapered edges, as shown in Figure 2.20(b) and Figures 2.21(a,b), which provide evidence of additional damage that is detrimental to the specimen strength. Milling each sidewall of a specimen, 1000 μm long and 1 μm deep, with 7 nA probe current using the "line cut" method required approximately 30 min of ion beam rastering. The rounded and tapered specimen edges were due to ion beam drift as a result of charging of the polysilicon specimens during milling. The rounded specimen edges further affected the ability to accurately machine the fillets, thus resulting in defects near the fillets as shown in Figures 2.22(a-b). When the fillets were included in the loading grips, the tensile strength of 0.5% PSG doped laminated polysilicon specimens (measured from 3 specimens) was consistent with undoped and heavily doped laminated polysilicon films averaging 2.37±0.33 GPa.

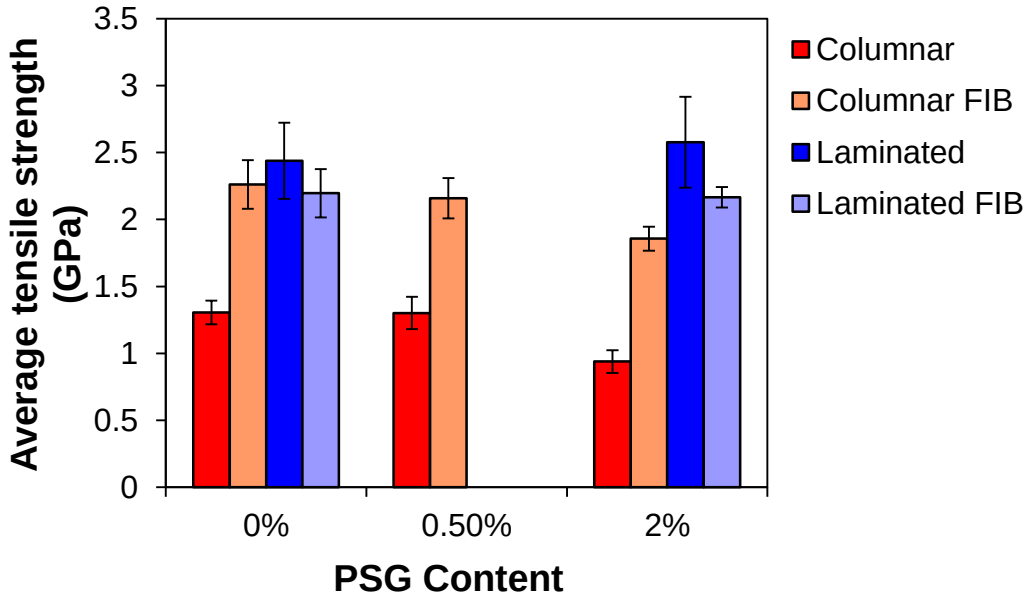

Figure 2.19. Comparison of average tensile strength of as-fabricated columnar and laminated polysilicon, and columnar and laminated polysilicon specimens with ion beam milled sidewalls using a FIB. The error bars represent ±1 standard deviation.

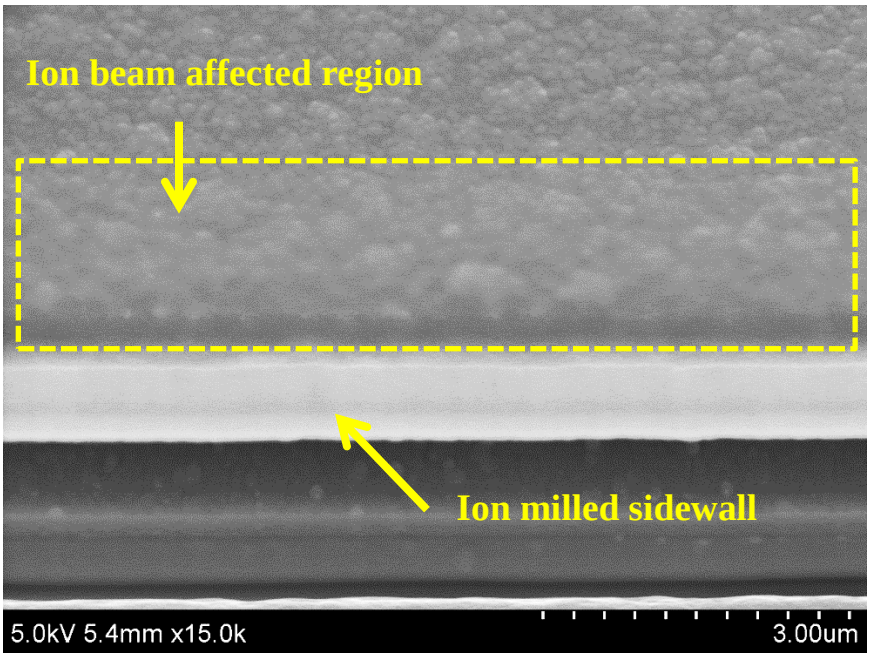

(a)

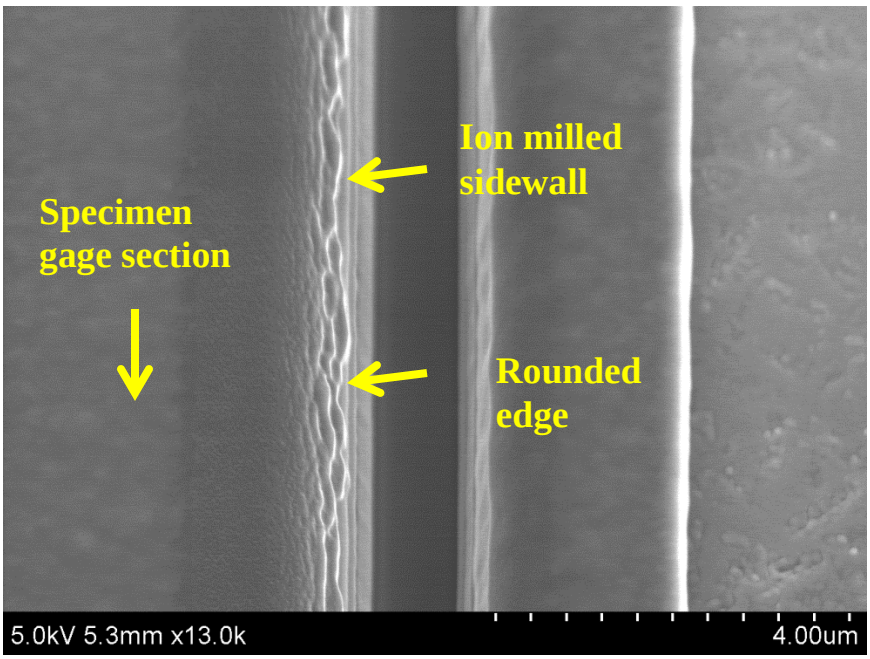

(b)

Figure 2.20. (a) Oblique and **(b)** top view of material damage near the specimen sidewalls of 2.0% PSG doped laminated polysilicon as a result of ion beam milling.

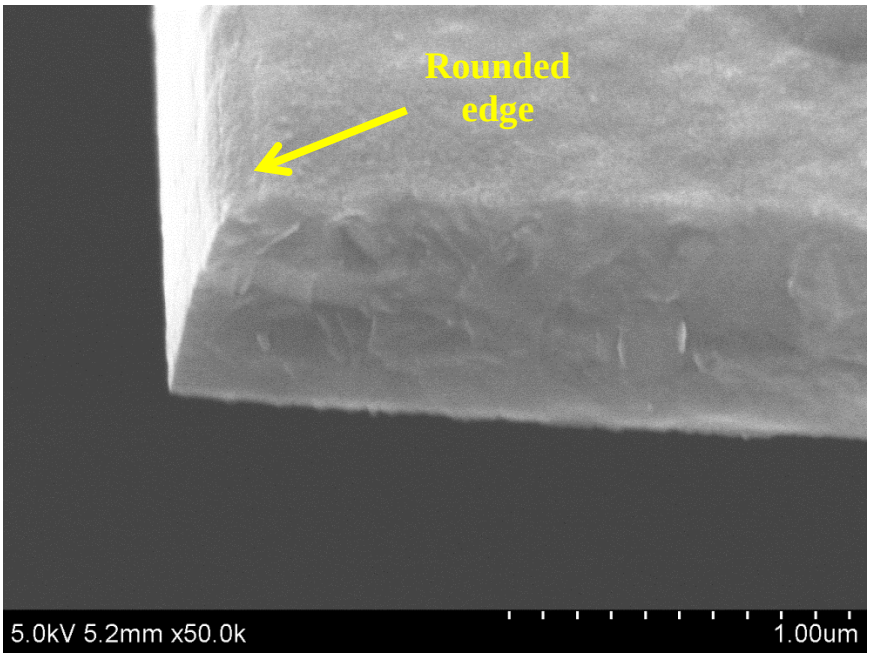

(a)

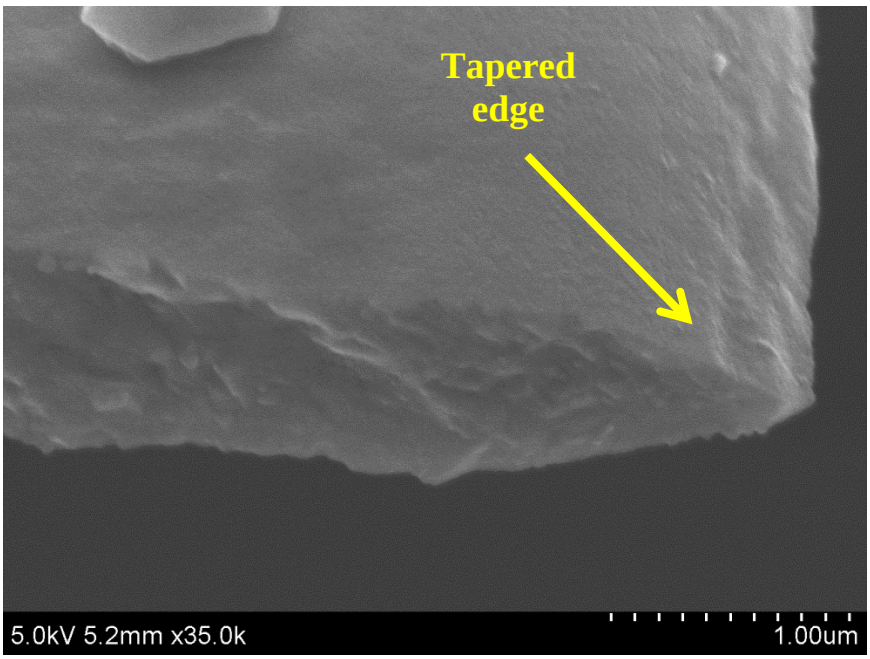

(b)

Figure 2.21. Fracture cross-sections of 0.5% PSG doped laminated polysilicon showing **(a)** rounded, and **(b)** tapered edges caused by ion beam drift during milling when using the "line cut" method.

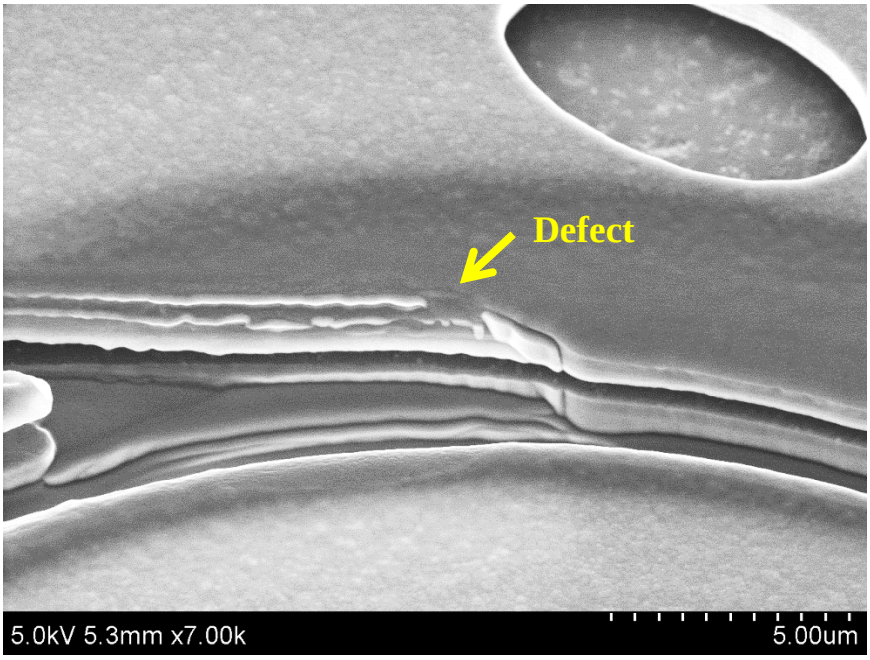

(a)

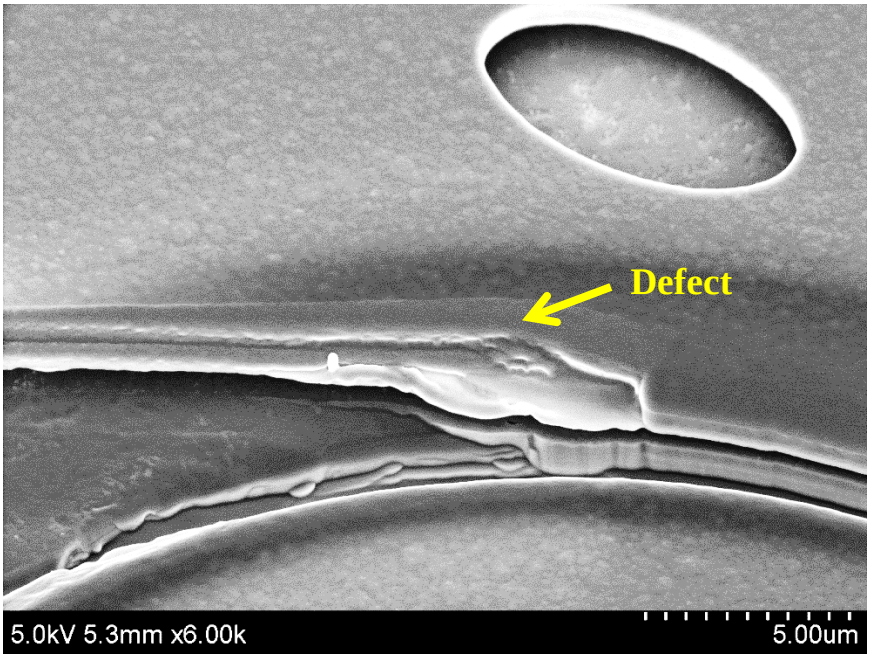

(b)

Figure 2.22. (a,b) Geometry of fillets after ion beam milling by a FIB.

This agreement confirms that failure of ion beam milled specimens was due to material damage at the sidewalls. In an attempt to address this issue, the "box cut" method was applied instead of a "line cut", in which the ion beam is rastered in a 1100 μm × 0.5 μm region to mill an as-fabricated sidewall. Milling each sidewall of a specimen using a "box cut" required approximately 90 min. The increased milling time resulted in significantly more damage at the sidewalls of laminated polysilicon, as shown in Figures 2.23(a,b). The increase in milling time enhanced the ion beam drift due to continuous charging of the specimen, which resulted in heavily rounded and tapered edges, as shown in Figures 2.24(a,b). A visual comparison between specimen edges milled by the "line cut" and the "box cut" methods is provided by Figures 2.21 and 2.24. In the case of undoped laminated polysilicon, the average tensile strength of specimens milled with the "box cut" method was 1.86±0.3 GPa, which was considerably lower than the value of 2.19±0.18 GPa obtained from the same specimens which were ion beam milled by the "line cut" method.

Similarly to specimens with as-fabricated sidewalls, the specimens with ion milled sidewalls also shattered at failure. Some of the laminated polysilicon specimens with ion milled sidewalls using the "line cut" method were tested inside a drop of glycerin to prevent scattering of the specimen fragments in order to locate the critical defects in the fracture cross-sections. Additionally, a high speed camera was mounted on an optical microscope to record specimen top surface during an experiment. Figure 2.25 shows successive frames of the specimen's top surface at the onset of failure. In spite of testing the specimen inside a drop of glycerin which dampened vibrations at failure and scattering, the specimens still broke in many small fragments (~5-10), as shown in Figures 2.25(c-d). The small fragments fell inside glycerin and could not be retrieved after the experiment. The fracture section of the remaining specimen at the left end, shown in Figures 2.25(a-d), was imaged by an SEM. As shown in Figure 2.26, the fracture section did not have any mirror, mist and hackle regions, which could point to the origin of failure initiation. Initial failure occurred at a different location in the gage section, as shown in Figure 2.25(b), which fragmented and fell inside glycerin. The fracture cross-sections in Figure 2.26(b) only imply that failure initiated at the heavily

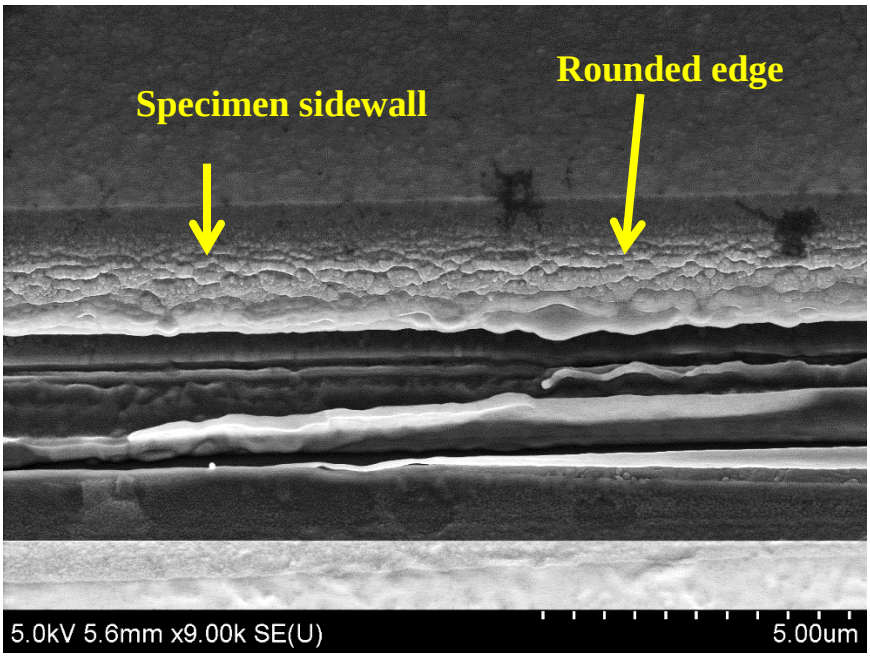

(a)

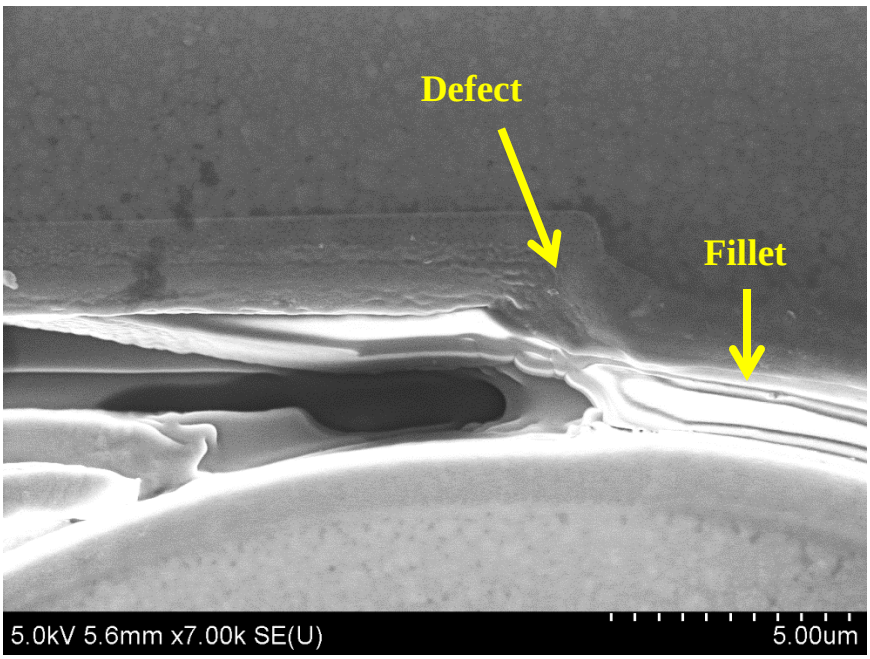

(b)

Figure 2.23. Material damage in undoped laminated polysilicon at **(a)** sidewalls, and **(b)** near the fillets as a result of employing the "box cut" method to mill the specimen sidewalls using a FIB.

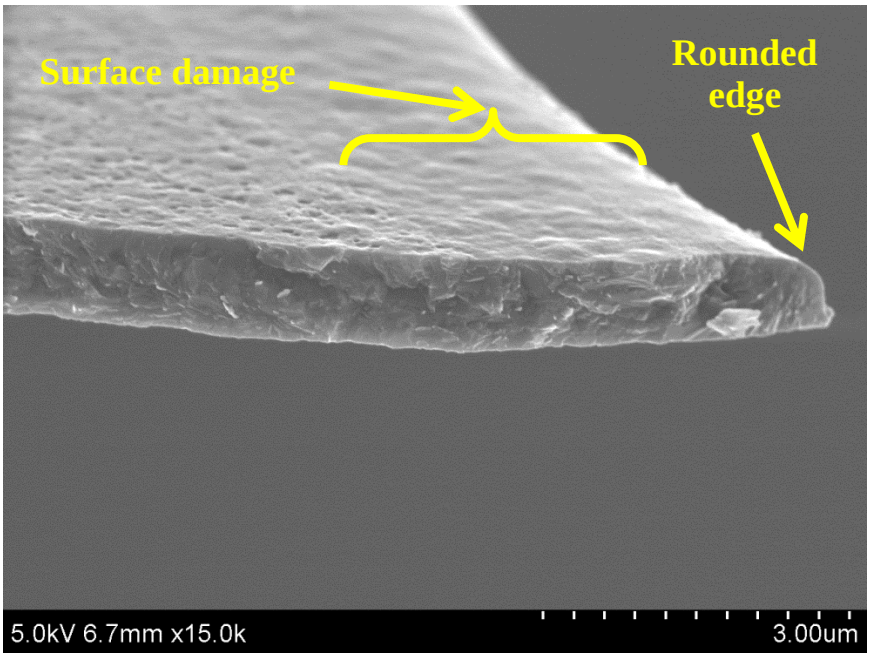

(a)

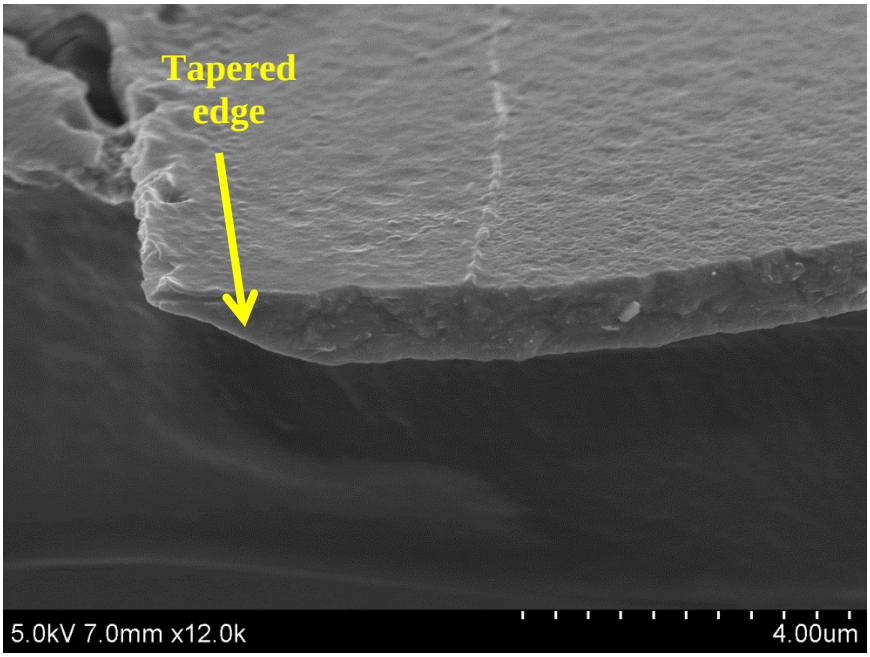

(b)

Figure 2.24. Fracture cross-sections of undoped laminated polysilicon films showing **(a)** rounded, and **(b)** tapered edges as a result of ion beam drift during milling using the "box cut" method.

(a)

(b)

(c)

(d)

Figure 2.25. (a-d) Optical images recorded at 50,000 fps and 100× magnification showing the fracture process of an ion beam milled 0.5% PSG doped laminated polysilicon specimen. The interframe time is ~20 µs.

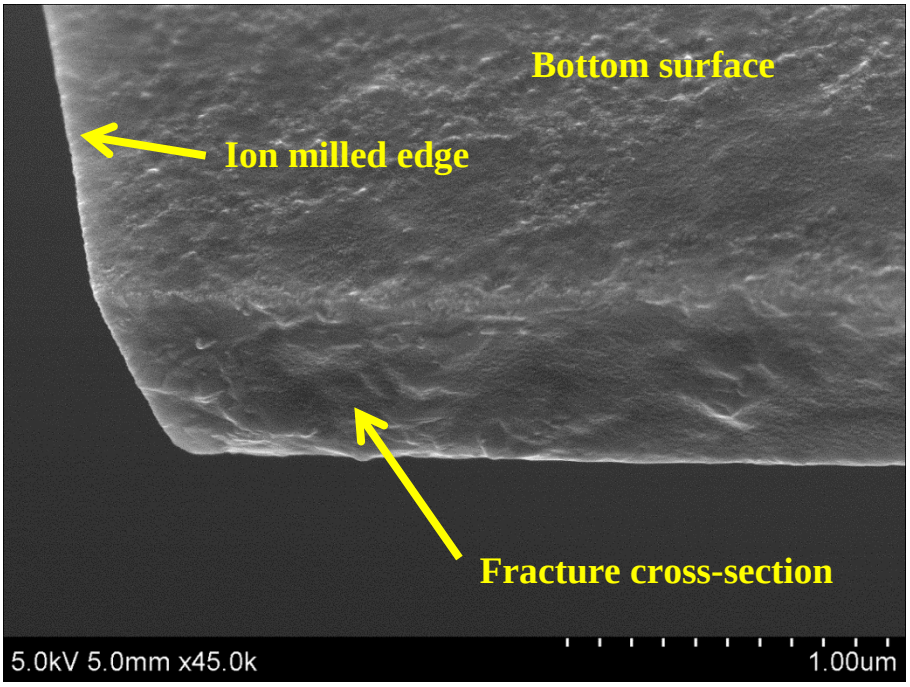

(a)

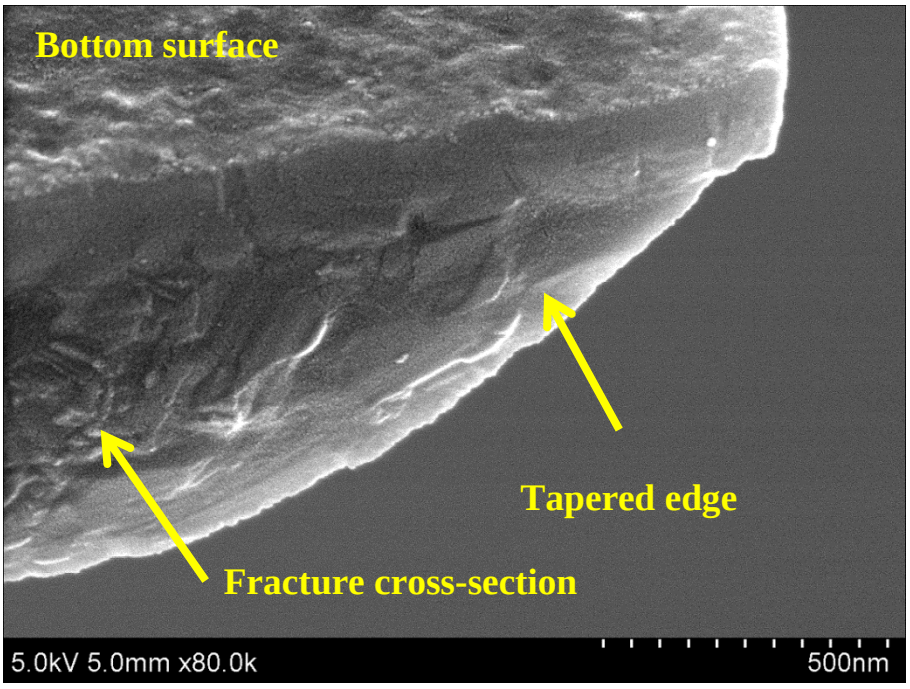

(b)

Figure 2.26 (a,b) SEM images of the two edges of a fracture cross-section of the 0.5% PSG doped laminated polysilicon specimen shown in Figure 2.25.

tapered specimen edges. As a result, the tensile strength of polysilicon films with ion beam milled sidewalls was limited by material damage caused by the ion milling process. Therefore, columnar polysilicon films with defect-free sidewalls could potentially withstand stresses beyond the average tensile strength value of 2.2 GPa, while the strength of undoped columnar polysilicon with smooth sidewalls could be very similar to that of laminated polysilicon.

The characteristic strengths of laminated and columnar polysilicon specimens measured in this work and in [41] are compared in Figure 2.27 with those of polysilicon layers fabricated using Sandia's standard SUMMiT V^{TM} [26] process. A comparison between the Poly1 layer and laminated polysilicon shows that the characteristic strength of the former, which is an integral part of the SUMMiT V^{TM} process, could be enhanced

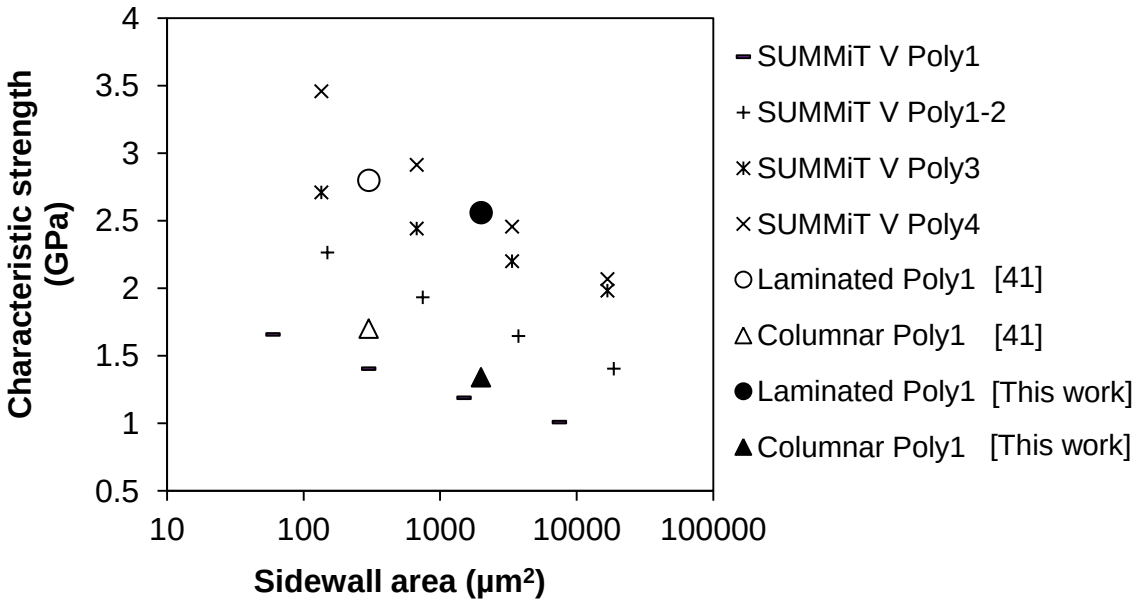

Figure 2.27. Comparison of characteristic strength of polysilicon measured in this work, with the Poly layers fabricated by the standard SUMMiT V^{TM} process. The sidewall area of the specimens tested in this work was 2,000 μm^2. The characteristic strengths of Poly1, Poly1-2, Poly3, Poly4 were reported in [26] for a gauge surface area of 1,000 μm^2.

by 40-150% through control of the microstructure of polysilicon, as described in this dissertation. Thus, if Poly1 was fabricated as a laminated layer, it could have characteristic strength as high as that of the Poly4 layer which has been reported to be the strongest of all polysilicon layers of the SUMMiT V^{TM} process.

2.7 Conclusions

The effects of microstructure and doping on the tensile strength of polysilicon were investigated using columnar and laminated polysilicon films subjected to different doping conditions. The Young's modulus was found to be independent of the grain structure and doping conditions. The strength of laminated polysilicon on the other hand was 60 - 90% higher than that of columnar polysilicon due to quite smaller critical flaws in the former. Heavy P-doping lowered the strength of columnar polysilicon by 30%, but had minimal effect on the strength of laminated polysilicon. The reduction in strength of columnar polysilicon was due to large, top edge, sidewall defects that formed during annealing and P diffusion and acted as stress concentrations. While these defects were more pronounced in polysilicon specimens doped with 2.0% PSG, they were not as severe in 0.5% PSG doped and undoped films, which provides a critical concentration for P, beyond which, defect formation is accelerated during annealing. Assuming that all critical flaws were present in the specimen sidewalls, the calculated Weibull parameters could closely predict the characteristic strength of 180 times smaller polysilicon specimens with the same grain size and doping, and *vice versa*. Notably, the strength of columnar polysilicon with ion milled sidewalls increased by 70-100% after eliminating the critical sidewall flaws. Although, a perfectly unbiased value for the tensile strength of columnar polysilicon could not be measured due to ion beam induced material damage at the sidewalls and geometrical imperfections introduced at the specimen fillets during ion milling, in the absence of the detrimental top edge sidewall flaws in columnar polysilicon the tensile strengths of undoped columnar and undoped laminated polysilicon were found to be very comparable.

CHAPTER 3

Fracture Toughness of Polysilicon Films

3.1 Introduction

The process of fracture of a brittle material in the presence of defects is dictated by the material fracture toughness (or the critical stress intensity factor) and the geometrical details of the defect with respect to the applied stress field. In polycrystalline materials, the material microstructure plays a key role in determining the effective fracture toughness, namely the toughness measured using boundary stress measurements and not the local stress at the crack tip. In Chapter 2, the strength of undoped and heavily doped columnar polysilicon was found to be lower than that of laminated polysilicon, due to the different nature and size of sidewall surface defects. While larger defects lower the mechanical strength, changes in local K_{IC} due to processing, such as doping and annealing, may also have an effect [32,40]. Hence, it is important to quantify the crack resistance of the different polysilicon films especially, those subjected to heavy doping. The intrinsic resistance of a material to fracture is quantified by experiments with pre-fabricated cracks with well-known geometry and dimensions.

In the present case, a reference for the expected values for the effective critical stress intensity factor of polysilicon, $K_{IC,eff}$, is provided by single crystal silicon data [44,68-70]. According to one reference [44], the K_{IC} for single crystal silicon (100), (110) and (111) planes is 0.95 MPa√m, 0.90 MPa√m and 0.83 MPa√m, respectively [44]. The $K_{IC,eff}$ for polysilicon films have been reported by several groups [71-73], with the most recent reports providing a distribution of values in the range of 0.8-1.2 MPa√m [53,73]. This variation in values has been attributed to local material anisotropy near the crack tip

and grain heterogeneity. A direct consequence of this distribution of values for $K_{IC,eff}$, which incorporates the effect of local variations in microstructure, is that cracks could arrest as long as $K_{IC,eff}$ is less than 1.2 MPa$\sqrt{m}$ [53], thus leading to an R-curve behavior.

In a computational analysis using cohesive-zone modeling, Foulk et al. [74,75] demonstrated that the grain shape, crystal lattice orientation and GB strength can also increase $K_{IC,eff}$ by local crack tip deflection and kinking. Figure 3.1 illustrates the crack growth mechanism in a polycrystalline material. Crack propagation takes place along paths of the least critical energy release rate. The advancing crack front encounters grains with higher toughness and as a result, the crack is either arrested or is deflected to a weaker GB. Crack deflection along GBs, Figure 3.1(b), is expected for materials with GB cohesive strength smaller than the grain due to processes, such as doping or prolonged etching in 49% HF, that deteriorate the strength of GBs. Local crack tip deflection followed by crack arrest results in mixed mode cracks and, therefore, an apparent increase (or decrease) in the measured K_{IC}. Thus, modification of the grain structure and potentially the energy landscape between grains and GBs could affect the material resistance to crack initiation. The energy landscape could be modified by dopants such as P that are known to segregate to GBs and promote grain growth [32]. Zeng et al. [51] and Swadener and Nastasi [52] reported an insignificant effect of P-doping on K_{IC} of single crystal silicon wafers, by employing the indentation technique. However, the effect of P-doping on the cohesive strength of silicon GBs is not available. An experimental study employed to understand the effect of grain structure and P-doping on the $K_{IC,eff}$ of polysilicon and the crack propagation mechanism is presented in this Chapter. Subsequently, predictions of the tensile strength are obtained by using established linear elastic fracture mechanics analyses, the measured values of $K_{IC,eff}$ and detailed defect geometry measurements. The results are compared with the experimentally measured values.

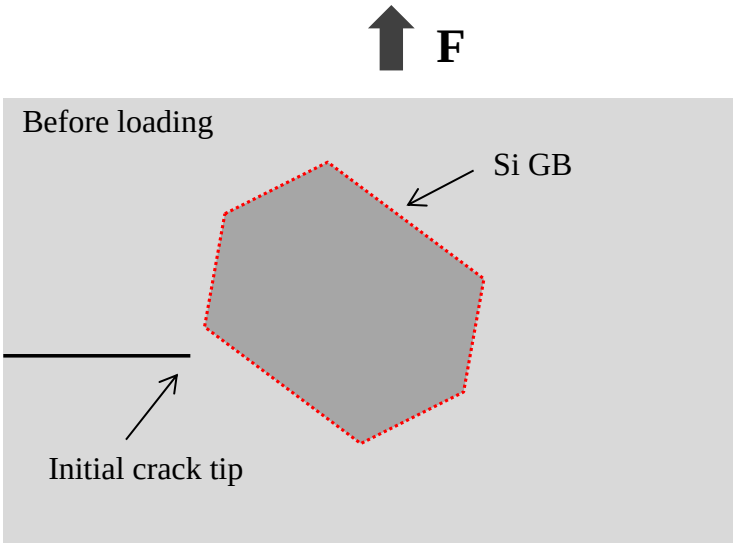

(a)

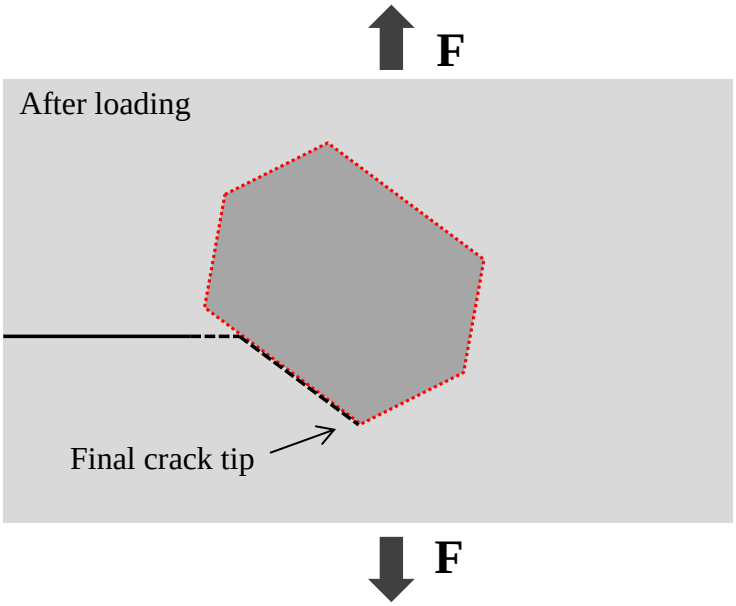

(b)

Figure 3.1. (a-b) Crack growth in an hetrogeneous material with reduced GB strength. Redrawn from [74] with permission from Elsevier.

3.2 Experimental Methodology

The polysilicon specimens used for fracture property measurements were same as those employed for the uniaxial tension experiments described in Chapter 2. For the purposes of fracture experiments, sharp cracks were introduced into the specimen gauge section by a microhardness indenter as described in [53]: an indent is generated to the silicon substrate alongside the unreleased tensile specimen and one of the edge cracks extending from the corners of the indent grows into the polysilicon specimen through the sacrificial oxide layer [53]. The schematics in Figure 3.2 and Figure 3.3(a) illustrate the process of mode I crack creation in polysilicon films. SEM and AFM images of the cracks and their tips were obtained for each specimen to measure the crack length and record the precise location of the crack tip with respect to the grain structure, as determined from the top film surface. Figures 3.3(b,c) show SEM and AFM images of a crack and its tip, respectively, in undoped columnar and laminated polysilicon. After indentation, the films were etched in 49% HF to obtain freestanding specimens with sharp cracks for fracture experiments. AFM images showing the crack and the location of its tip for 0.5% PSG doped and 2.0% PSG doped columnar and laminated polysilicon are shown in Figures 3.4(a-d).

The in-situ uniaxial tension testing apparatus described in Chapter 2 was used to perform mode I fracture experiments. The applied far-field load was obtained by a loadcell with 50 g capacity. The $K_{IC,eff}$ from the edge cracked specimens was calculated using the LEFM solution [76]:

$$K_{IC,eff} = \sigma_{\infty} Y \sqrt{\pi a} \tag{3.1}$$

where σ_{∞} is the far-field stress, a is the crack length, and Y is the shape function given by

$$Y = 1.122 - 0.231\left(\frac{a}{w}\right) + 10.55\left(\frac{a}{w}\right)^2 - 21.71\left(\frac{a}{w}\right)^3 + 30.382\left(\frac{a}{w}\right)^4 + H.O.T \tag{3.2}$$

where w is specimen width. The far-field stress at failure was calculated from the failure load and the cross-section of the films.

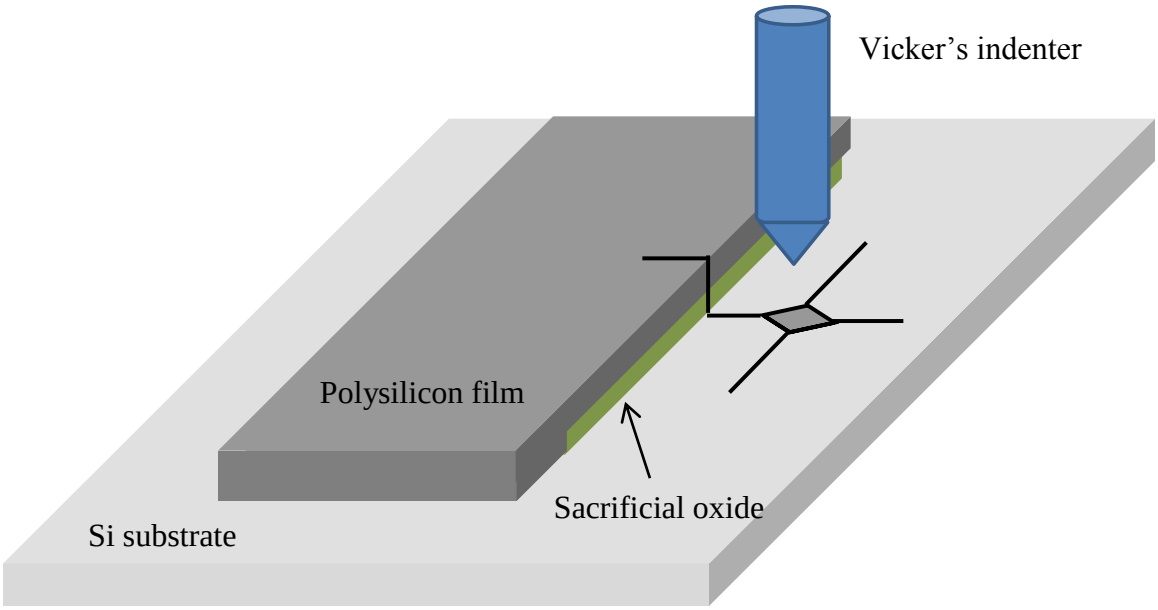

(a)

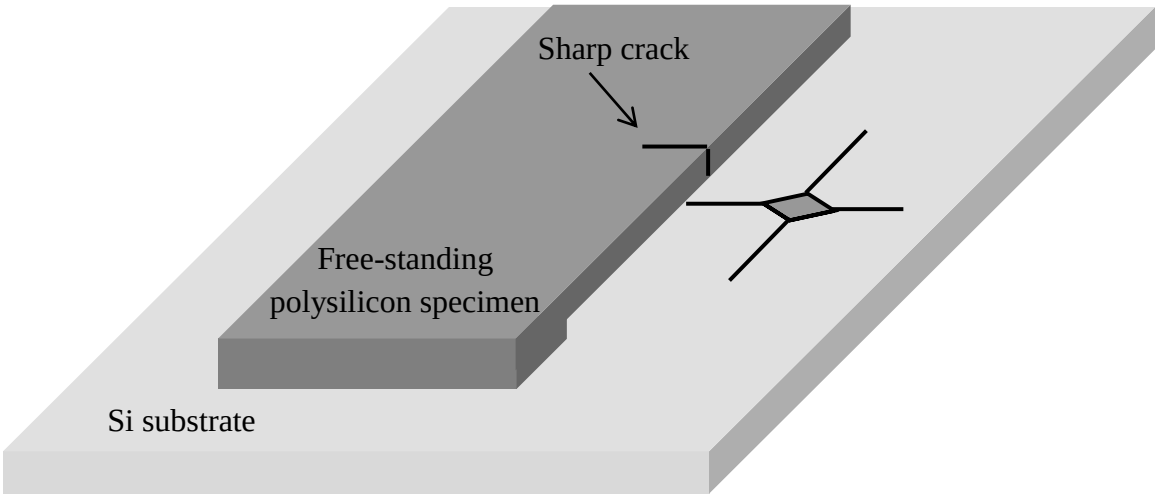

(b)

Figure 3.2. (a) Crack creation in a polysilicon film using a Vicker's indenter, and **(b)** freestanding polysilicon specimen with a sharp crack after etching of the sacrificial oxide.

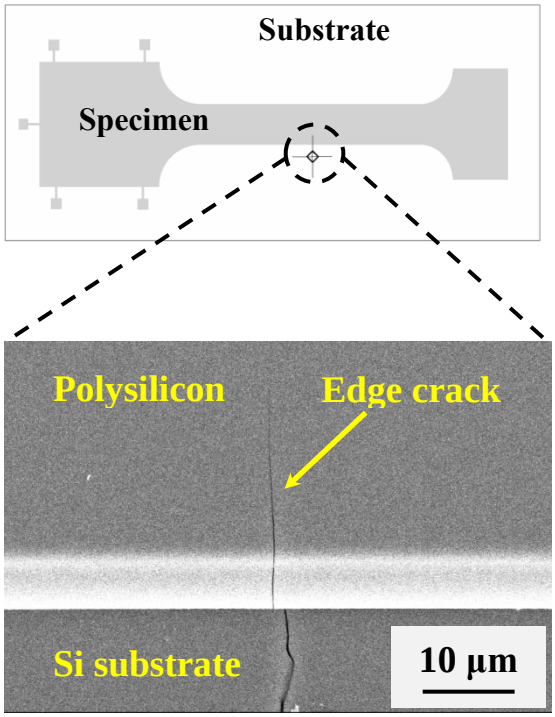

(a)

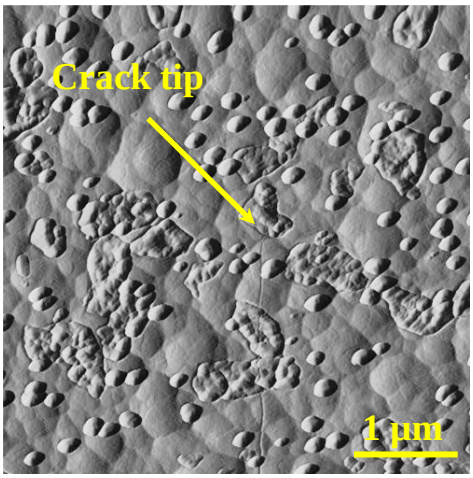

(b)

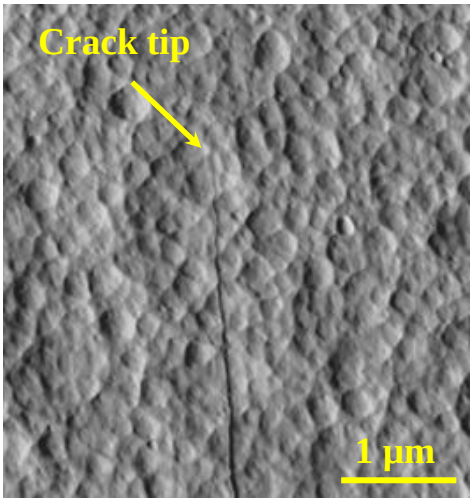

(c)

Figure 3.3. (a) Edge pre-crack. AFM image of pre-crack tip in: undoped **(b)** columnar grain polysilicon, and **(c)** laminated polysilicon.

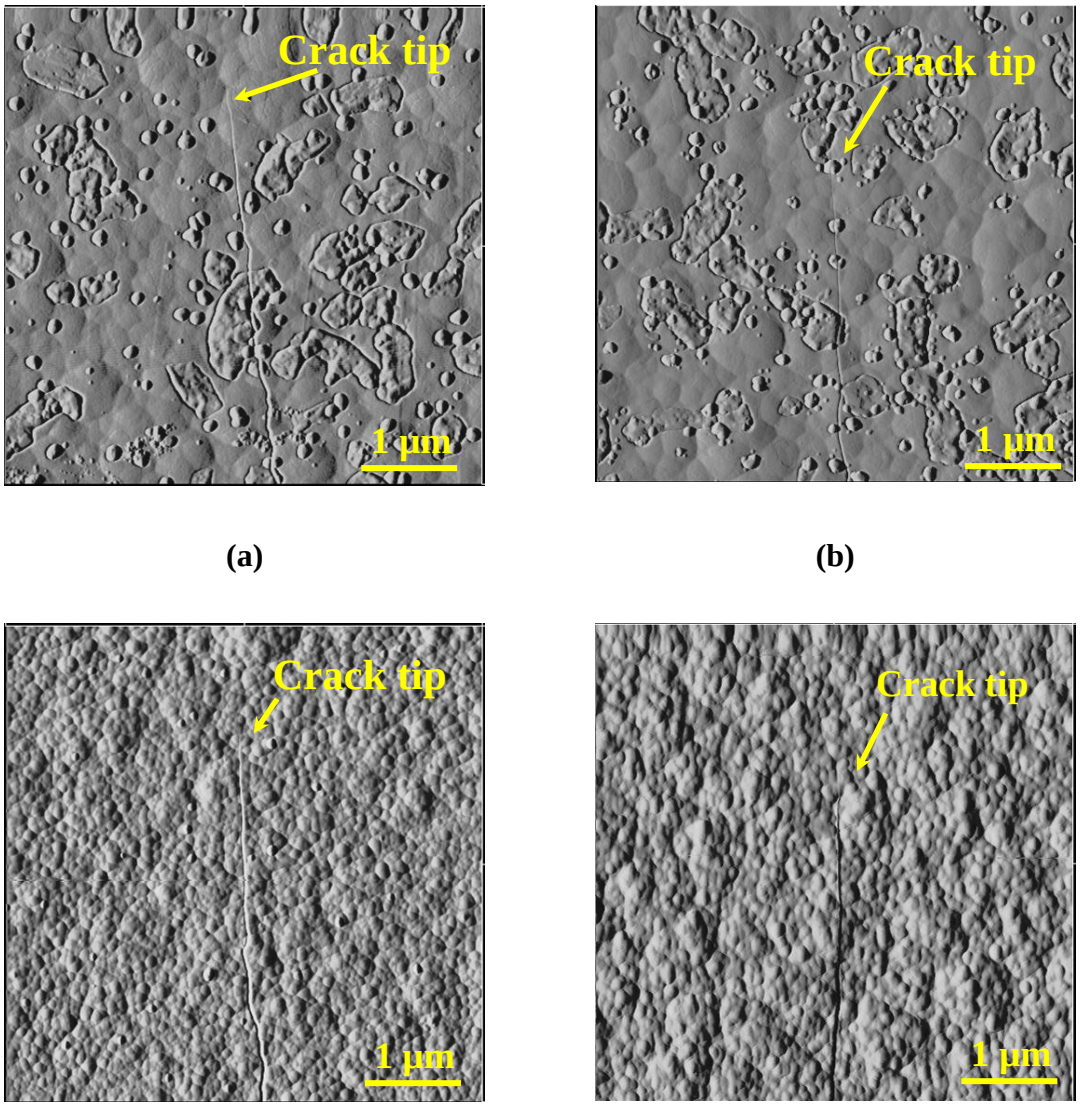

Figure 3.4. AFM photodetector signal error image showing the crack tip location in **(a)** undoped columnar, **(b)** 2.0% PSG columnar, **(c)** undoped laminated, and **(d)** 2.0% PSG laminated polysilicon.

3.3 Effective Mode I Critical Stress Intensity Factors of Polysilicon Films

The calculated $K_{IC,eff}$ for columnar grain and laminated polysilicon films doped with different concentrations of P are given in Table 3.1 and plotted in Figure 3.5. A minimum of 15 specimens were tested for each specimen type. The $K_{IC,eff}$ from all polysilicon thin films was in the range of 0.8 - 1.2 MPa√m which agrees with the K_{IC} values for bulk silicon [44,68,69] and the $K_{IC,eff}$ for polysilicon fabricated by the MUMPs process, previously reported by Chasiotis et al. [53,73]. The average $K_{IC,eff}$ varied slightly with the grain structure and with doping level. Specifically, the $K_{IC,eff}$ values for columnar grain polysilicon were in the range of 0.88 - 1.2 MPa√m vs. laminated polysilicon whose $K_{IC,eff}$ values were in the range of 0.85 - 1.08 MPa√m, averaging 0.95±0.08 MPa√m and 0.99±0.05 MPa√m, respectively. Notably, there was substantial scatter in the values of $K_{IC,eff}$ by as much as 40%, for specimens from the same die with (statistically) the same microstructure and doping level. This value distribution was actually larger for columnar grain polysilicon doped with 0.5% and 2.0% PSG compared to laminated polysilicon.

Table 3.1. $K_{IC,eff}$ of columnar and laminated polysilicon doped with different concentrations of P. The average value and one standard deviation are presented.

Polysilicon	$K_{IC,eff}$ (MPa√m)
Undoped laminated	0.99±0.05
0.5% PSG laminated	0.94±0.10
2.0% PSG laminated	0.95±0.08
Undoped columnar	0.95±0.08
0.5% PSG columnar	1.02±0.13
2.0% PSG columnar	1.05±0.14

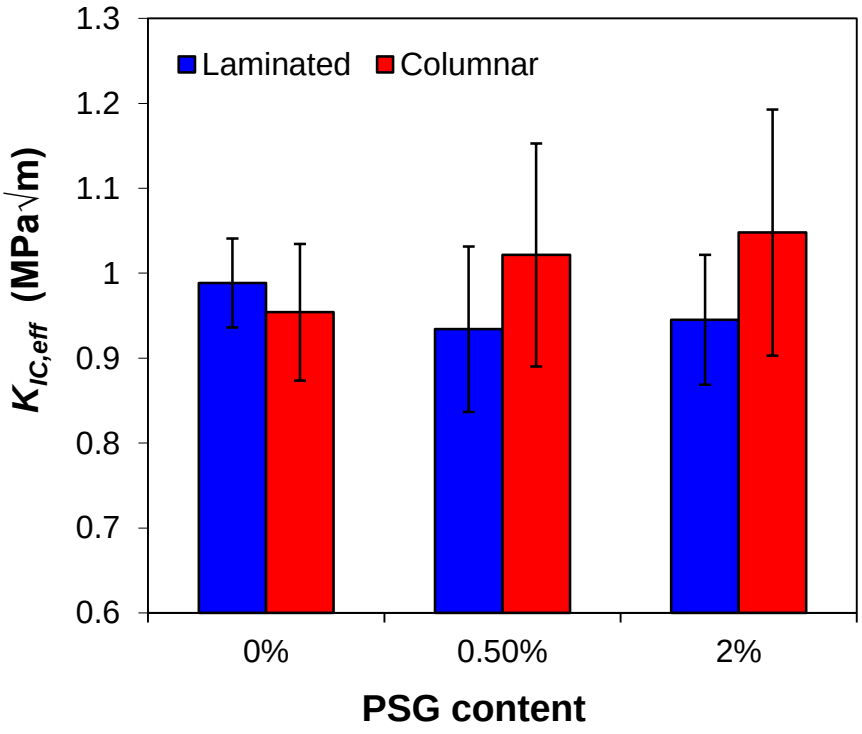

Figure 3.5. $K_{IC,eff}$ of laminated and columnar grain polysilicon vs. P-doping. The error bars represent one standard deviation.

3.4 Effect of Grain Structure and Doping on Local Fracture Initiation

The role of GBs and P-doping on the local fracture behavior of polysilicon in the immediate vicinity of the critical flaws identified in the Chapter 2, may be evaluated by fracture mechanics measurements which can indicate whether **(a)** GBs increase or decrease the fracture resistance, and **(b)** high P concentration changes the local energy release rate for fracture initiation. Due to the polycrystalline nature, the location of the initial crack tip generated in the specimens could be either inside a grain or at a GB, and as a result the values of $K_{IC,eff}$ for undoped polysilicon films varied in the range of 0.8 - 1.2 MPa√m. In [53,73], it was shown that the presence of crack tip at a GB increases the effective K_{IC} of polysilicon. However, three dimensional effects can overshadow such

conclusions that are derived based on two dimensional material considerations. For instance, Figures 3.6(a,b) show AFM images of two different specimens belonging to the same die but exhibiting $K_{IC,eff}$ values of 0.88 MPa√m and 1.03 MPa√m, with the crack tip at the top specimen surface residing at a GB and inside a grain but near a triple junction point, respectively. According to Figure 3.5, this variability in the measured effective K_{IC} was more pronounced for undoped columnar than for undoped laminated polysilicon, due to the random distribution of columnar grains with different orientations where the value of $K_{IC,eff}$ was mostly dependent on the particular (fairly columnar) grain where the crack tip was located. In contrast, the crack tip plane crossed a large number of grains (~10) across the thickness of laminated polysilicon films, which resulted in values for $K_{IC,eff}$ that represented the average of the local value of K_{IC} of several grains through the specimen thickness. Due to this sampling of multiple grains at the crack front, the $K_{IC,eff}$ of laminated polysilicon was close to the average value for single crystal Si (~0.9 MPa√m), and resulted in much tighter distribution of values.

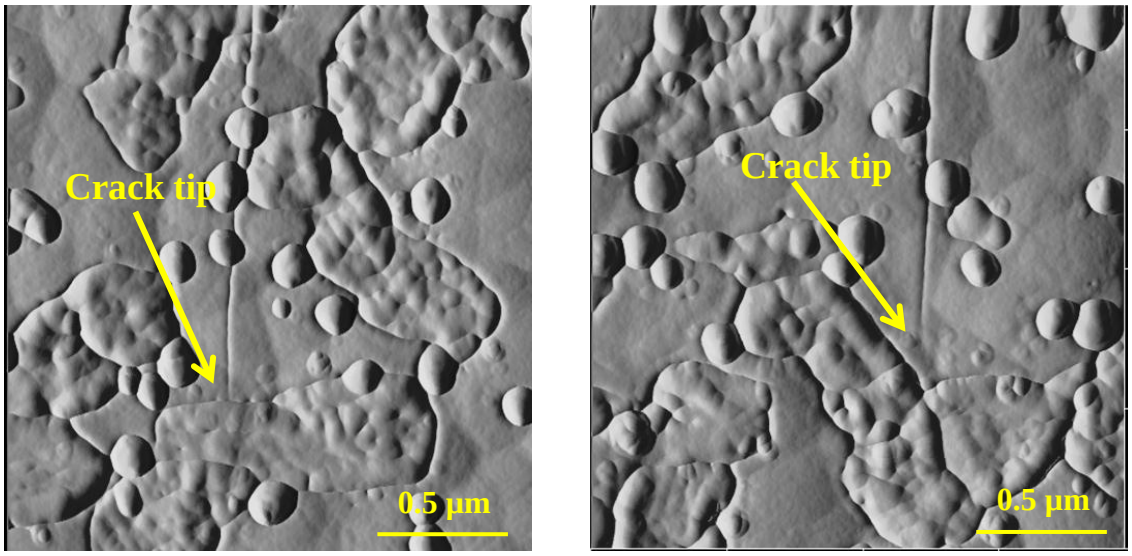

(a) **(b)**

Figure 3.6. AFM top surface images of columnar polysilicon with the crack tip located **(a)** at a GB, resulting in $K_{IC,eff}$ = 0.86 MPa√m, and **(b)** within a grain and in front of a triple junction, resulting in $K_{IC,eff}$ = 1.03 MPa√m.

Similarly to MUMPs polysilicon [53], the local polycrystalline heterogeneity in columnar polysilicon promoted crack arrest: for example, a specimen doped with 2.0% PSG, demonstrated subcritical crack growth: the crack arrested at a GB after an initial advancement and then reinitiated at a higher load. Figure 3.7(a) shows a pre-crack extending to the left hand side, and the fracture cross-section is shown in Figure 3.7(b). The AFM image in Figure 3.7(c) shows the initial location of the crack tip. Upon the applied load of 5.15 mN, the pre-crack initiated, kinked at an angle with respect to the far field load and was arrested at the next grain resulting in an increase in $K_{IC,eff}$. A drop in the load was recorded in the force vs. time plot in Figure 3.7(d). In the initial crack advance, $K_{I,eff}$ = 0.82 MPa√m, which lies at the low bound of measured $K_{IC,eff}$ values. The crack resisted further loading up to 6.8 mN when it propagated catastrophically for $K_{IC,eff}$ = 1.1 MPa√m which is 25% higher than that for the first crack advance. This fracture process was a consequence of local variations in K_{IC} due to microstructure, as illustrated by a cohesive zone microstructural model by Foulk et al. [74,75]. It should be noted, that in addition to the local variations in K_{IC}, the arrested kinked crack in Figure 3.7(b) required a larger load to initiate catastrophic failure due to local mode mixity which resulted in a higher $K_{IC,eff}$.

The $K_{IC,eff}$ of columnar polysilicon doped with 0.5% and 2.0% PSG content was 1.02±0.13 MPa√m and 1.05±0.14 MPa√m, respectively. The $K_{IC,eff}$ for these two types of doped columnar polysilicon was 10% higher than that for undoped polysilicon which averaged 0.95±0.08 MPa√m. The standard deviation of the measured $K_{IC,eff}$ values was also higher for P-doped columnar polysilicon. During diffusion doping at high temperatures (1050 °C), P atoms diffuse into substitutional sites of a Si crystal [51], which alters the cohesive energy thereby modifying its K_{IC}. The bond strength of P-Si (363.6 KJmol^{-1}) is 11% higher than that of Si-Si bond (326.86 KJmol^{-1}) and hence the energy release rate for polysilicon doped with P is higher than undoped Si [77]. An analogous 10% increase in $K_{IC,eff}$ between undoped and 2% PSG doped polysilicon is established from the present fracture experiments[3]. On the other hand, the $K_{IC,eff}$ for doped laminated polysilicon was close to the undoped material, which could be explained

[3] The increase in the critical energy release rate is of the same order of magnitude.

by an uneven distribution of P across the film thickness. The laminated structure limited the diffusion of P throughout the film thickness as opposed to columnar grain polysilicon which facilitates fast P diffusion via its long GBs. Depth profiling measurements of P concentration may shed more light into this hypothesis.

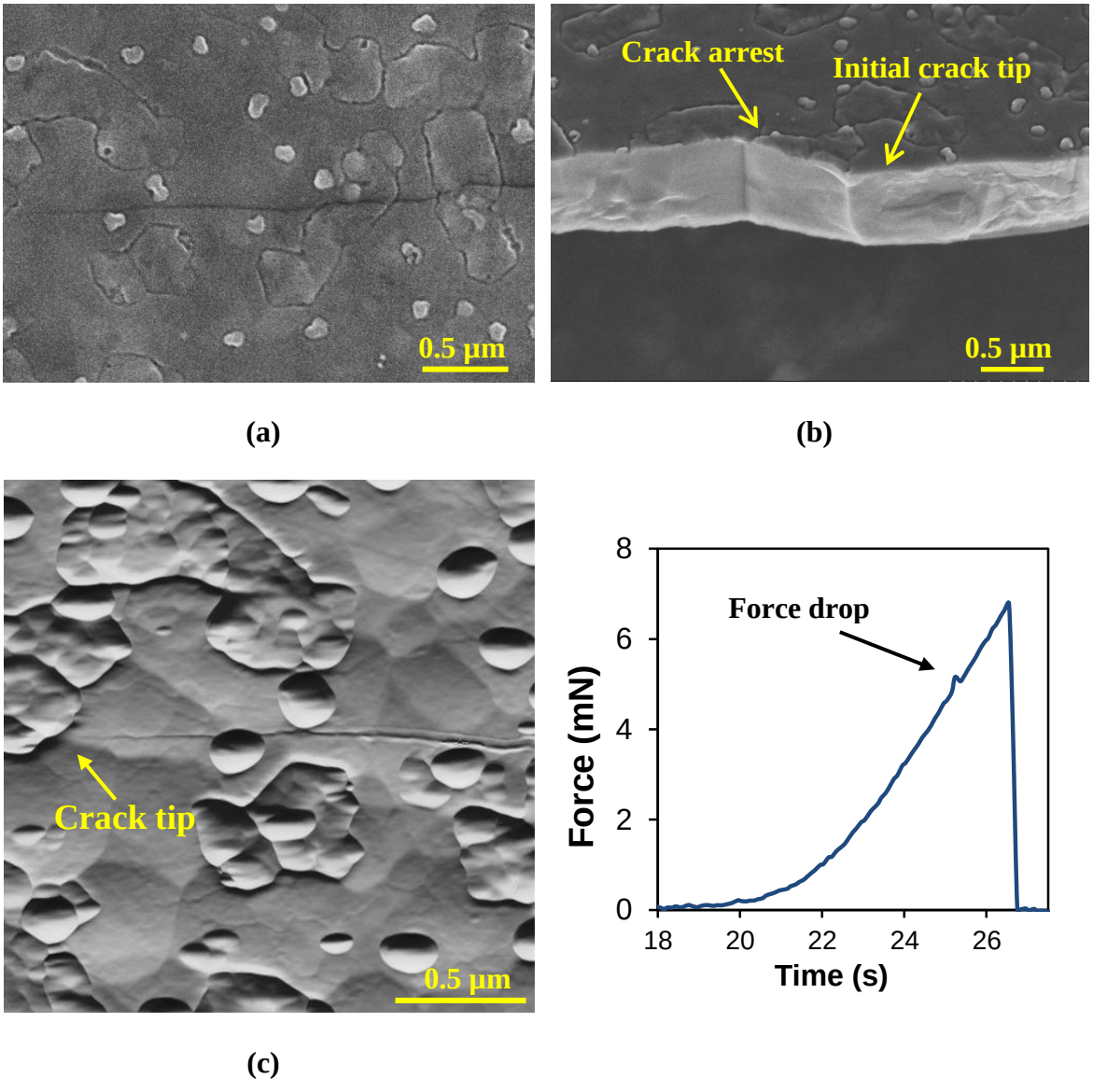

Figure 3.7. **(a)** SEM image of top view of a pre-crack created in a heavily doped columnar polysilicon specimen. **(b)** Fracture surface after catastrophic failure. **(c)** AFM top surface image of pre-crack tip, and **(d)** far-field force vs. time during loading.

On the contrary, the $K_{IC,eff}$ of doped columnar polysilicon was most frequently in the range of 1.1 - 1.2 MPa√m. These relatively high $K_{IC,eff}$ values compared to the undoped material were due to the combined effect of near crack tip material anisotropy and GB inhomogeneity due to high P content. The effect of doping on $K_{IC,eff}$ is, however, overshadowed by its dependence on the location of crack tip which already results in a variation of $K_{IC,eff}$ in the broad range of 0.8 - 1.2 MPa√m. From this analysis it can be deduced that the reduced tensile strength of doped columnar polysilicon reported in Chapter 2 is solely due to larger defects and not changes in fracture resistance. On the contrary, heavily doped columnar polysilicon was marginally tougher than the undoped material.

3.5 Predictions of Tensile Strength using Surface Flaw Data

In the absence of major volumetric flaws or notches in a brittle material, the tensile strength is limited by the surface roughness which acts as surface microcracks. With the knowledge of K_{IC} and the spectrum of surface roughness of a brittle material, its tensile strength could be estimated by using LEFM. Using a finite element formulation, Raju and Newman [78] calculated the mode I stress intensity factors (K_I) for various defect geometries in a finite body, such as an embedded elliptical crack, a semi-elliptical surface crack, Figure 3.8(a,c), and a quarter-elliptical edge crack, Figure 3.8(b,d). From their results, analytical expressions were developed to compute K_I for a finite body. Specifically, the K_I for the semi-elliptical surface crack shown in Figure 3.8(c) is given by

$$K_I = \sigma\sqrt{\pi\frac{a}{Q}}F_s\left(\frac{a}{t},\frac{a}{c},\frac{c}{b},\phi\right) \tag{3.3}$$

where σ is far field stress, Q is shape factor for an elliptical crack, and F_s is boundary correction factor for surface crack. The shape factor Q for an elliptical shaped flaw is approximated by Equation (3.4) for $a/c \leq 1$ and Equation (3.5) for $a/c > 1$:

$$Q = 1 + 1.464\left(\frac{a}{c}\right)^{1.65} \tag{3.4}$$

$$Q = 1 + 1.464\left(\frac{c}{a}\right)^{1.65} \tag{3.5}$$

For $0 \le a/c \le 2$, $c/b < 0.5$ and $0 \le \phi \le \pi$, F_s is given by

$$F_s = \left[M_1 + M_2\left(\frac{a}{t}\right)^2 + M_3\left(\frac{a}{t}\right)^4\right] g f_\phi f_w \tag{3.6}$$

where M_i are curve fitting parameters, and g, f_w and f_ϕ are a curve fitting function, a finite width correction factor and an angular function, respectively, and are given by [78]:

$$M_1 = 1.13 - 0.09\left(\frac{a}{c}\right) \tag{3.7}$$

$$M_2 = -0.54 + \frac{0.89}{0.2 + \left(\frac{a}{c}\right)} \tag{3.8}$$

$$M_3 = 0.5 - \frac{1}{0.65 + \left(\frac{a}{c}\right)} + 14\left(1 - \frac{a}{c}\right)^{24} \tag{3.9}$$

$$g = 1 + \left[0.1 + 0.35\left(\frac{a}{t}\right)^2\right](1 - \sin\phi)^2 \tag{3.10}$$

$$f_\phi = \left[\left(\frac{a}{c}\right)^2 \cos^2\phi + \cos^2\phi\right]^{\frac{1}{4}} \tag{3.11}$$

$$f_w = \left[\sec\left(\frac{\pi c}{2b}\sqrt{\frac{a}{t}}\right)\right]^{\frac{1}{2}} \tag{3.12}$$

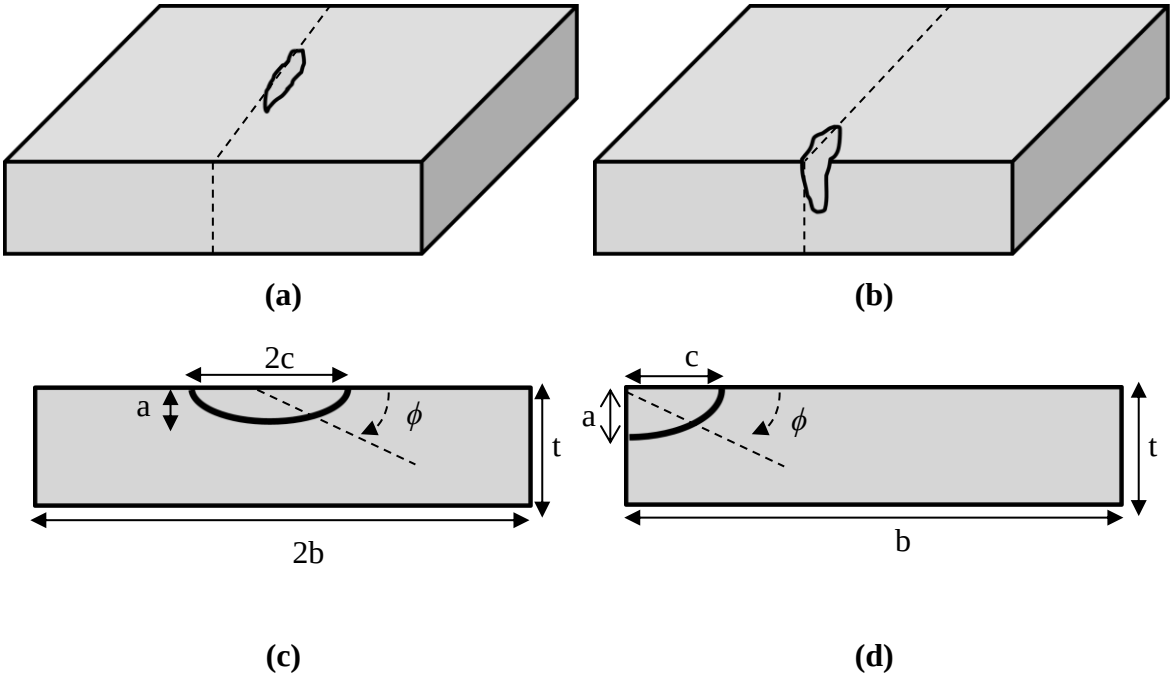

Figure 3.8. (a) Semi-elliptical surface crack, **(b)** quarter-elliptical edge crack, and **(c-d)** the corresponding cross sectional views.

Similarly, the K_I for a finite body with a quarter-elliptical edge crack, Figure 3.8(b,d), is given by

$$K_I = \sigma\sqrt{\pi\frac{a}{Q}}F_c(\frac{a}{t},\frac{a}{c},\phi) \tag{3.13}$$

where F_c is the boundary correction factor for an edge crack. The shape factor for a quarter-elliptical shaped crack is the same as that for a semi-elliptical crack in Equations (3.4) and (3.5). The boundary correction factor F_c is given by

$$F_c = \left[M_1 + M_2\left(\frac{a}{t}\right)^2 + M_3\left(\frac{a}{t}\right)^4\right]g_1 g_2 f_\phi \tag{3.14}$$

For $0.2 \le a/c \le 1$, $a/t \le 1$, and $0 \le \phi \le \pi/2$, the curve fitting parameter M_i, the curve fitting functions (g_1, g_2), and the angular function (f_ϕ) are given by [78]:

$$M_1 = 1.08 - 0.03\left(\frac{a}{c}\right) \tag{3.15}$$

$$M_2 = -0.44 + \frac{1.06}{0.3 + \left(\frac{a}{c}\right)} \tag{3.16}$$

$$M_3 = -0.5 + 0.25\left(\frac{a}{c}\right) + 14\left(1 - \frac{a}{c}\right)^{15} \tag{3.17}$$

$$g_1 = 1 + \left[0.08 + 0.4\left(\frac{a}{t}\right)^2\right](1 - \sin\phi)^3 \tag{3.18}$$

$$g_2 = 1 + \left[0.08 + 0.15\left(\frac{a}{t}\right)^2\right](1 - \cos\phi)^3 \tag{3.19}$$

$$f_\phi = \left[\left(\frac{a}{c}\right)^2 \cos^2\phi + \sin^2\phi\right]^{\frac{1}{4}} \tag{3.20}$$

For $a/c > 1$, M_i and g_i are given by [78]:

$$M_1 = \sqrt{\frac{c}{a}}\left(1.08 - 0.03\left(\frac{a}{c}\right)\right) \tag{3.21}$$

$$M_2 = 0.375\left(\frac{c}{a}\right)^2 \tag{3.22}$$

$$M_3 = -0.25\left(\frac{a}{c}\right)^2 \tag{3.23}$$

$$g_1 = 1 + \left[0.08 + 0.4 \left(\frac{c}{t} \right)^2 \right] (1 - \sin\phi)^3 \tag{3.24}$$

$$g_2 = 1 + \left[0.08 + 0.15 \left(\frac{c}{t} \right)^2 \right] (1 - \cos\phi)^3 \tag{3.25}$$

$$f_\phi = \left[\left(\frac{c}{a} \right)^2 \sin^2\phi + \cos^2\phi \right]^{\frac{1}{4}} \tag{3.26}$$

The tensile strength of laminated and columnar polysilicon was estimated using Equations (3.3) and (3.13) and the flaw geometry as captured in AFM images. From 10×10 μm^2 AFM images of the surface topography of laminated and columnar polysilicon, the RMS surface roughness, the mean-to-valley, and the maximum valley depths (below the surface mean plane) were measured as listed in Table 3.2. Even though the RMS surface roughness was uniform across all polysilicon films in the range of 8 - 10 nm, the mean-to-valley and maximum valley depths were slightly larger in the case of undoped, 0.5% PSG doped columnar polysilicon and significantly larger in heavily doped columnar polysilicon, as shown in Figures 3.9(a,b).

The AFM topography images shown in Figures 3.10(a,b) revealed frequent long grooves on the top surface of columnar polysilicon, which were scarce on laminated polysilicon films. While the frequency of such surface defects did not correlate with dopant concentration in columnar and laminated polysilicon, heavy doping made these groves deeper only in the case of columnar polysilicon. An example of a surface defect in undoped laminated polysilicon and a cross-sectional height profile are shown in Figures 3.11(a) and 3.11(b), respectively. This groove could be approximated as a semi-elliptical surface crack with length $2c$ = 1,200 nm and depth a = 25 nm. In a similar manner, the geometry of crack-like flaws at the top surface of different types of polysilicon films was measured from AFM topography images. A minimum of four severe defects found on the

top surface of each polysilicon type were used to calculate the average and standard deviation for the values of the length (*2c*) and the depth (*a*), as listed in Table 3.3.

Table 3.2. Surface roughness of different polysilicon films measured in three 10×10 μm^2 surface areas with an AFM.

Polysilicon	RMS roughness (nm)	Mean-to-valley depth (nm)	Maximum valley depth (nm)
Undoped laminated	9.5 ± 0.7	17.1 ± 1.0	22.2 ± 2.2
0.5% PSG laminated	8.1 ± 0.3	16.7 ± 0.8	23.4 ± 0.3
2.0% PSG laminated	8.0 ± 0.3	17.4 ± 0.6	24.7 ± 1.5
Undoped columnar	7.8 ± 0.7	18.3 ± 0.3	28.8 ± 1.1
0.5% PSG columnar	8.5 ± 0.6	18.3 ± 0.9	29.0 ± 2.1
2.0% PSG columnar	8.6 ± 0.7	21.2 ± 1.1	37.7 ± 5.1

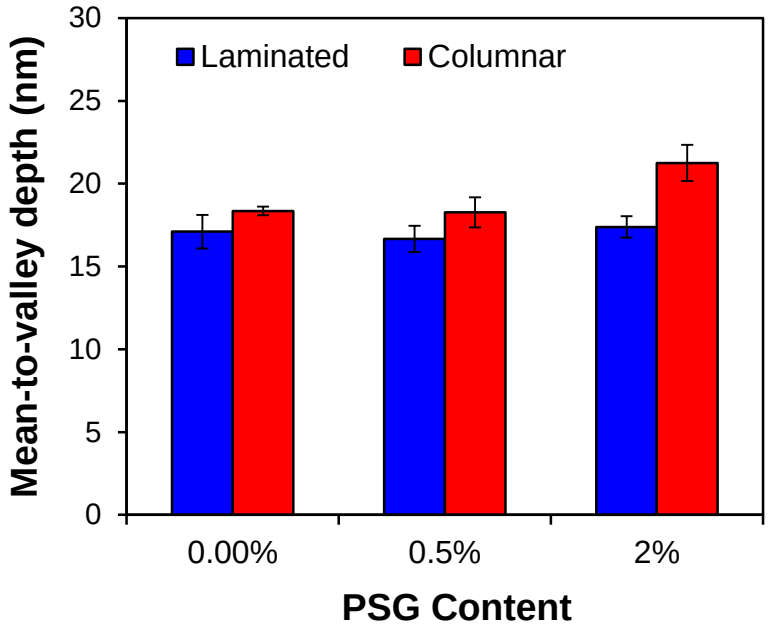

(a)

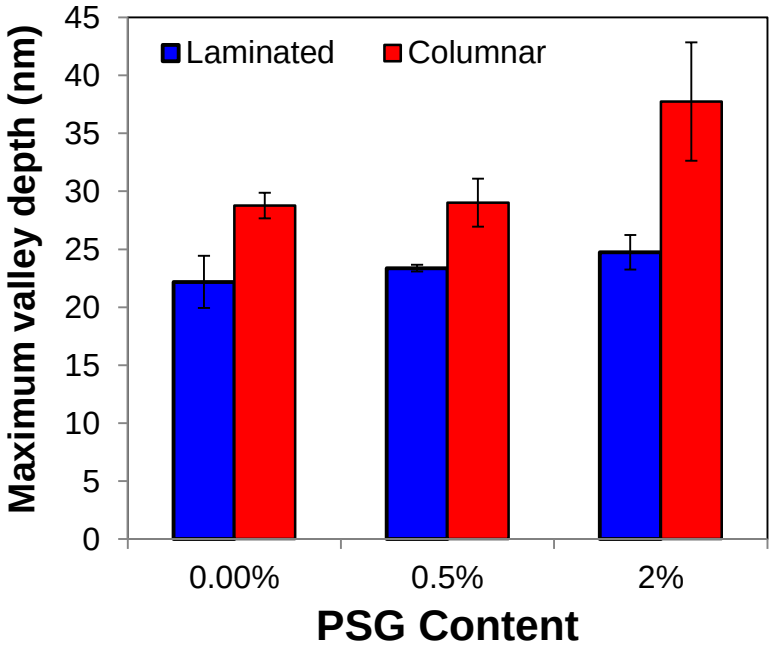

(b)

Figure 3.9. (a) Mean-to-valley, and **(b)** maximum valley depths of different polysilicon films measured by AFM from three 10×10 μm^2 surface areas.

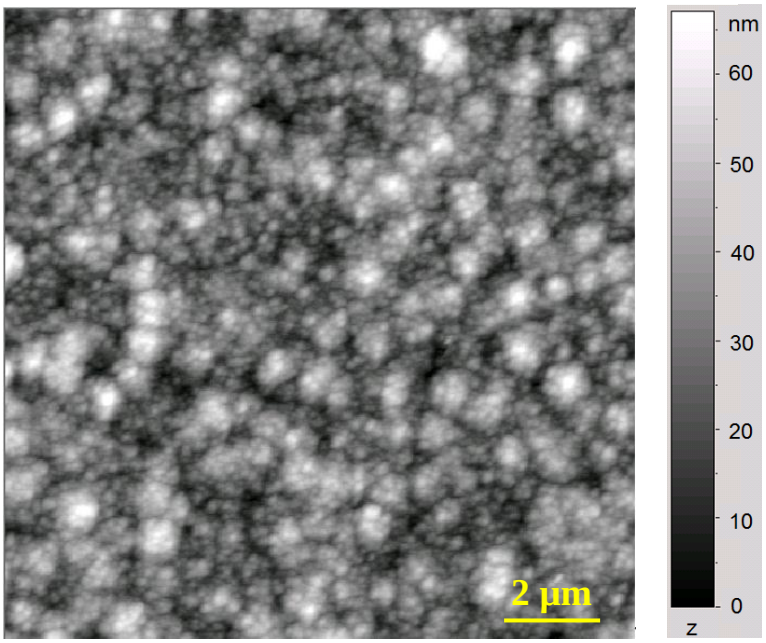

(a)

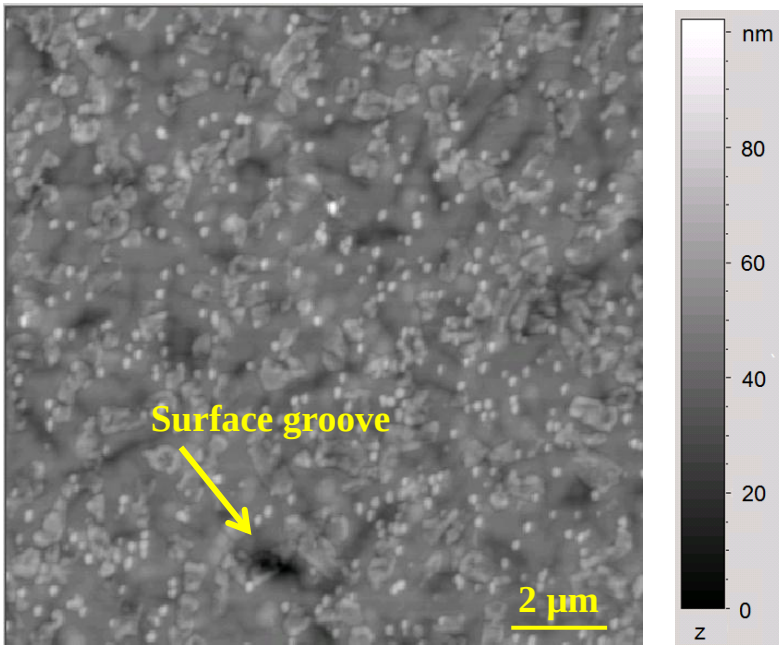

(b)

Figure 3.10. AFM images of surface topography of **(a)** undoped laminated, and **(b)** undoped columnar grain polysilicon. Surface grooves were deeper and more frequent in columnar grain than laminated polysilicon.

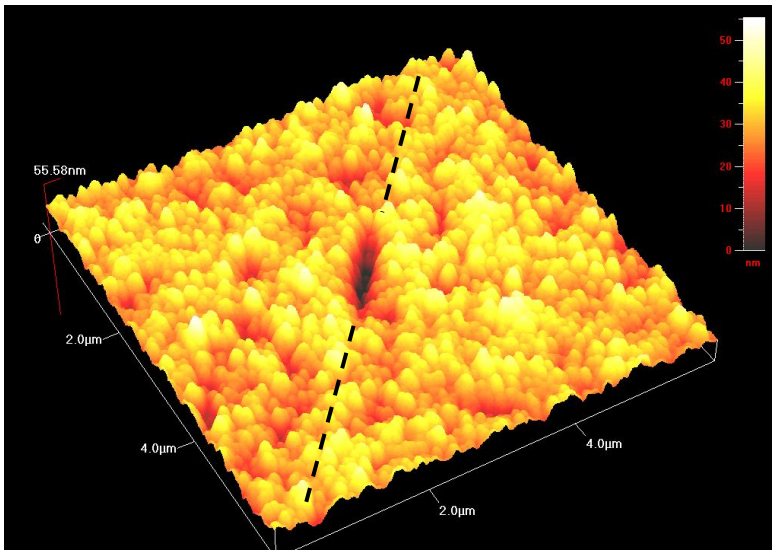

(a)

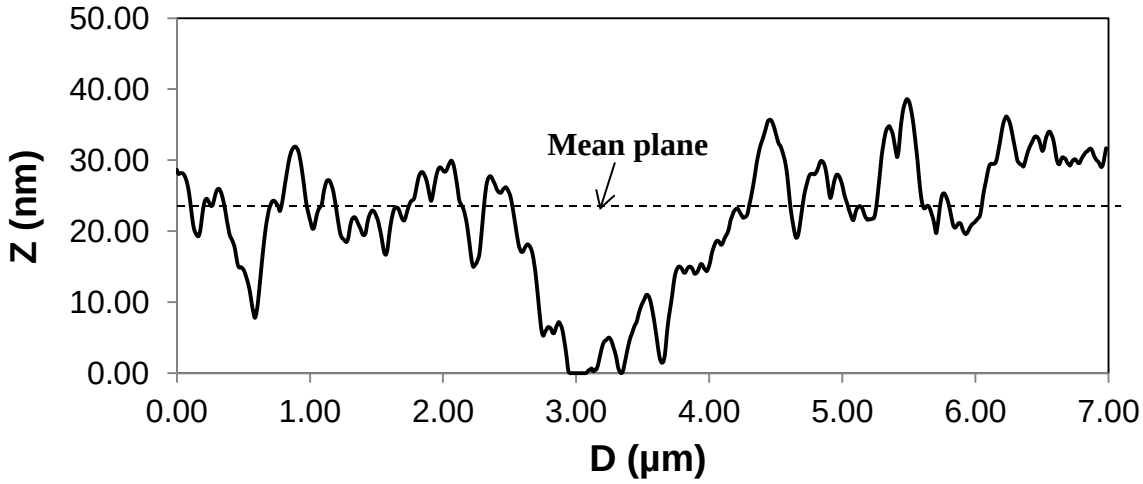

(b)

Figure 3.11. (a) 3-D topography of undoped laminated polysilicon obtained by AFM, and **(b)** height profile at the cross-section indicated in (a). The defect geometry based on such height profiles was used to make predictions for the tensile strength of polysilicon films.

The tensile strength of laminated and columnar polysilicon specimens was calculated by approximating the top surface grooves with semi-elliptical cracks and

applying Equation (3.3) using the measured $K_{IC,eff}$ values. The uncertainty in the estimated value of the tensile strength of each polysilicon type was also calculated by taking into account the standard deviation and the bounds in the measured values for $K_{IC,eff}$, a, and c. [79] In general, if z is a function of independent variables w, x, and y with uncertainties Δw, Δx, and Δy, respectively, the uncertainty Δz is given by:

$$\Delta z = \sqrt{\left(\frac{\partial f}{\partial w}\right)^2 \Delta w^2 + \left(\frac{\partial f}{\partial x}\right)^2 \Delta x^2 + \left(\frac{\partial f}{\partial y}\right)^2 \Delta y^2 + \ldots} \qquad (3.27)$$

A Matlab script was used [80] to calculate the uncertainty in the estimated tensile strength values based on the uncertainties in K_{IC}, a, and c and Equations (3.3) and (3.13). A first estimate of the total uncertainty in tensile strength was computed by using the values for one standard deviation for K_{IC}, a, and c. However, this approach underestimates the maximum uncertainty in tensile strength values because it does not capture the extreme values. Hence, a broad range of estimates for the tensile strength was obtained by using the half range of the total spread of the measured values for K_{IC}, a, and c as the uncertainty in the value of those quantities.

Comparisons between measurements and predictions for as-fabricated and ion milled specimens are provided in Table 3.3 and Figures 3.12(a,b). The estimated strength of laminated polysilicon was in the range of 2.48 - 3.94 GPa, and for columnar polysilicon in the range of 2.09 - 3.50 GPa. As expected from the preceding scaling analysis and Figures 2.13 and 2.14, failure of as-fabricated specimens initiated at the specimen sidewalls. Therefore, any predictions based on top surface flaws would greatly overestimate the film strength. In order to predict the tensile strength of polysilicon with critical sidewall defects, the flaws in Figures 2.13 and 2.14 were approximated as quarter-elliptical edge cracks with lengths a and c, as shown in the schematic in Figure 3.8(b,d). The tensile strength was predicted using the K_I relation for a quarter-elliptical edge crack given in Equation (3.13). The uncertainty in the tensile strength was calculated by using Equation (3.27). SEM images shown in Figures 3.13 - 3.17 were used to measure the

approximate flaw geometry which is summarized in Table 3.4. The average length *c* and depth *a* of the edge cracks for undoped columnar polysilicon were measured from Figure 3.13 as 462±126 nm and 93±23 nm, respectively. Similarly, for 2.0% PSG doped columnar polysilicon, *c* and *a* were 152±32 nm and 620±74 nm according to Figure 3.15. In the case of laminated polysilicon, multiple notches were present at the 100-nm deep sidewall step located at the edge of the bottom surface, as shown in Figures 3.16 and 3.17. The tensile strength of these films was estimated by approximating the largest notch inside the step as a quarter elliptical edge crack, neglecting the potentially amplifying effects of the step and the adjacent defects. The length of the edge crack was measured from the top view SEM images shown in Figures 3.16 and 3.17, and the depth of the edge crack was taken as the step height which was 100 nm for all laminated polysilicon films. The strength of different polysilicon films was predicted in the presence of an edge crack and is compared with values measured from as-fabricated specimens in Table 3.4 and Figure 3.18. In the case of 2.0% PSG doped columnar polysilicon, through thickness edge notch defects were also observed, as shown in Figure 3.19. Hence, the tensile strength of these specimens was also estimated by approximating the notches as sharp cracks with length *a*, and using Equations (3.1) and (3.2). A comparison between the experimental and estimated tensile strength values is presented in Figure 3.20. The strength predicted for laminated and columnar polysilicon films agreed with the measured values, which supports the previous discussion that the tensile strength of laminated and columnar polysilicon was governed by sidewall flaws. It should be noted that this analysis presents a conservative estimate of the tensile strength because it does not take into account the flaw orientation with respect to the far-field applied force.

Table 3.3. Experimental vs. predicted average tensile strength of polysilicon specimens with as-fabricated sidewalls and ion milled sidewalls using a semi-elliptical crack as the top surface flaw geometry.

Polysilicon	Flaw Geometry		$\sigma_{f,predicted}$ (GPa)	$\sigma_{f,as\text{-}fabricated}$ (GPa)	$\sigma_{f,FIB}$ (GPa)
	a **(nm)**	***2c*** **(μm)**			
Undoped laminated	23.4±2.9	1.3±0.3	3.3±0.4	2.4±0.3	2.2±0.2
0.5% PSG laminated	21.1±2.8	1.0±0.6	3.4±0.6	-	2.4±0.3
2.0% PSG laminated	27.4±3.2	1.4±0.1	2.9±0.4	2.5±0.2	2.2±0.1
Undoped columnar	30.7±8.6	1.3±0.5	2.6±0.6	1.3±0.1	2.3±0.2
0.5% PSG columnar	27.6±3.4	1.2±0.3	3.0±0.5	1.3±0.1	2.2±0.2
2.0% PSG columnar	37.7±1.3	1.1±0.6	2.7±0.6	0.92±0.1	1.9±0.1

Table 3.4. Experimental vs. predicted average tensile strength of polysilicon specimens with as-fabricated sidewalls using a quarter elliptical edge crack as the specimen sidewall edge flaw geometry.

Polysilicon	Flaw Geometry		$\sigma_{f,predicted}$ (GPa)	$\sigma_{f,as\text{-}fabricated}$ (GPa)
	a **(nm)**	***c*** **(μm)**		
Undoped laminated	100	0.084±0.018	2.7±0.43	2.4±0.3
0.5% PSG laminated	-	-	-	-
2.0% PSG laminated	100	0.104±0.032	2.32±0.45	2.5±0.2
Undoped columnar	93.0±22.8	0.46±0.13	1.6±0.4	1.3±0.1
0.5% PSG columnar	88.6±2.6	0.39±0.18	1.7±0.4	1.3±0.1
2.0% PSG columnar	620±152	0.15±0.03	1.42±0.3	0.95±0.1

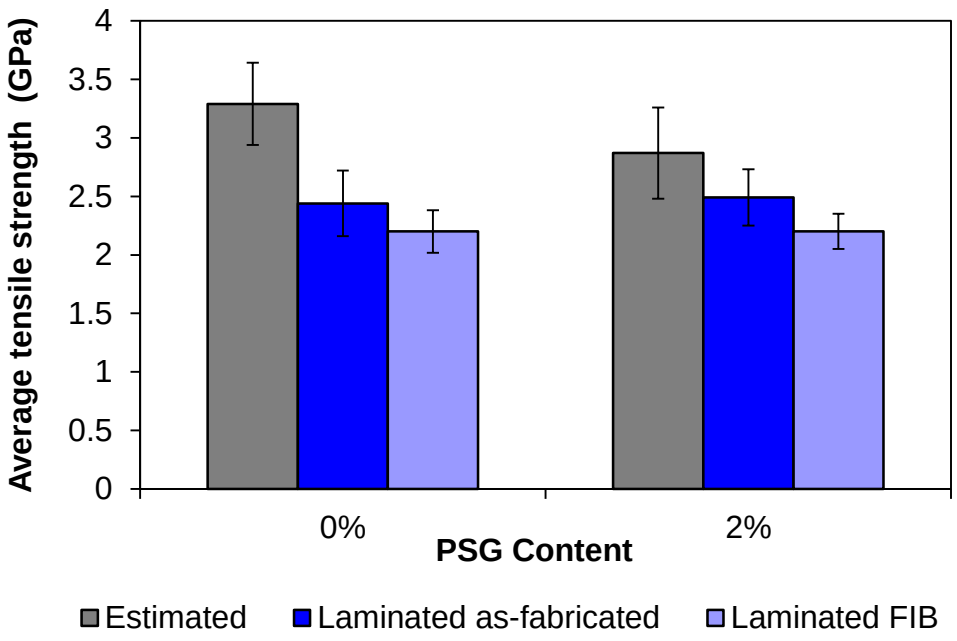

(a)

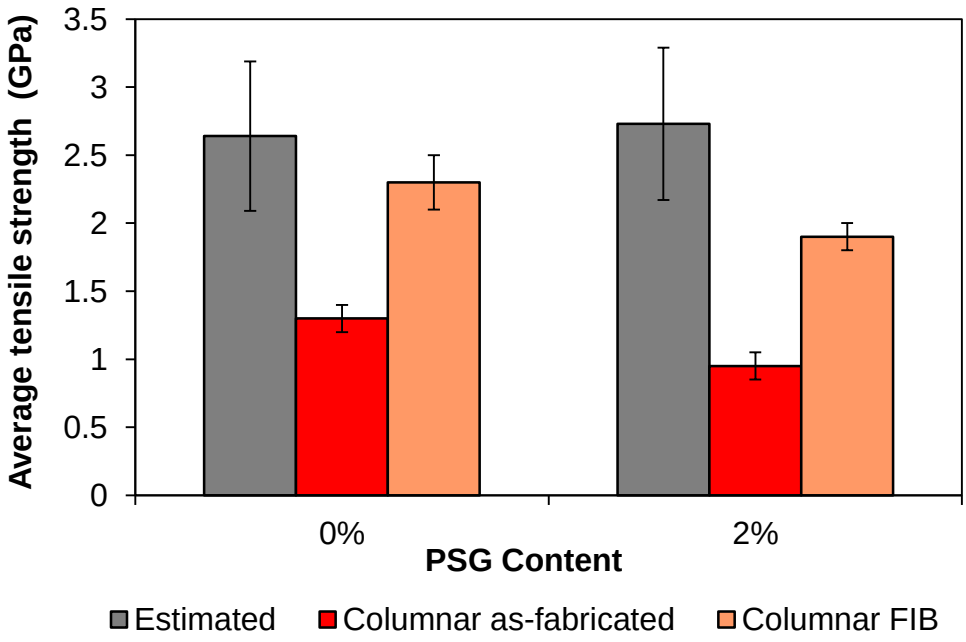

(b)

Figure 3.12. Comparison between estimated and measured tensile strength of as-fabricated and ion beam milled specimen sidewalls for **(a)** laminated and **(b)** columnar polysilicon. The tensile strength was estimated by assuming the top surface flaws as the critical defects.

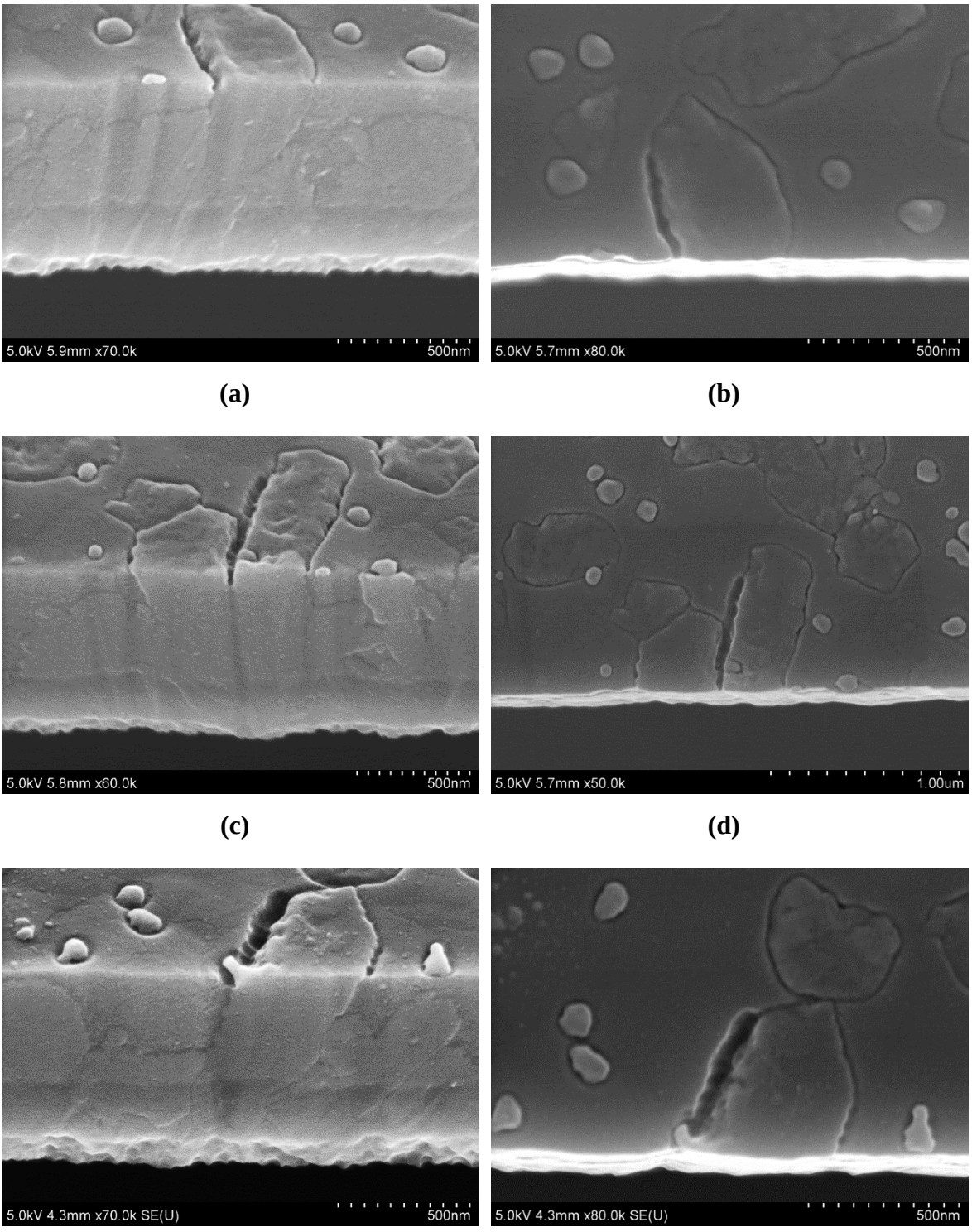

Figure 3.13. (a,c,e) Sidewall and **(b,d,f)** corresponding top surface views of specimen edge defects in undoped columnar polysilicon.

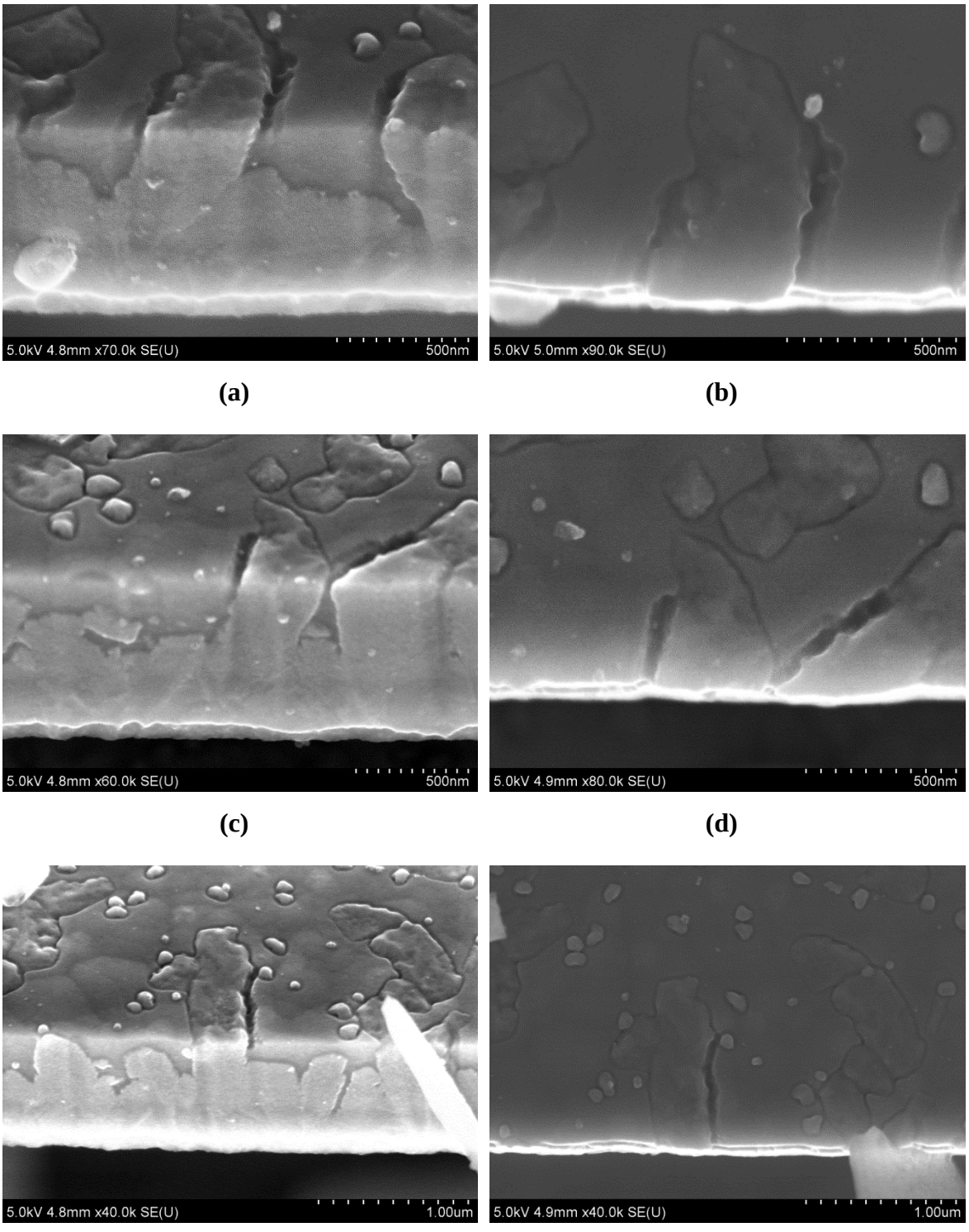

Figure 3.14. SEM images of **(a,c,e)** sidewalls and, **(b,d,f)** the corresponding top surface views of specimen edge defects in 0.5% PSG doped columnar polysilicon films.

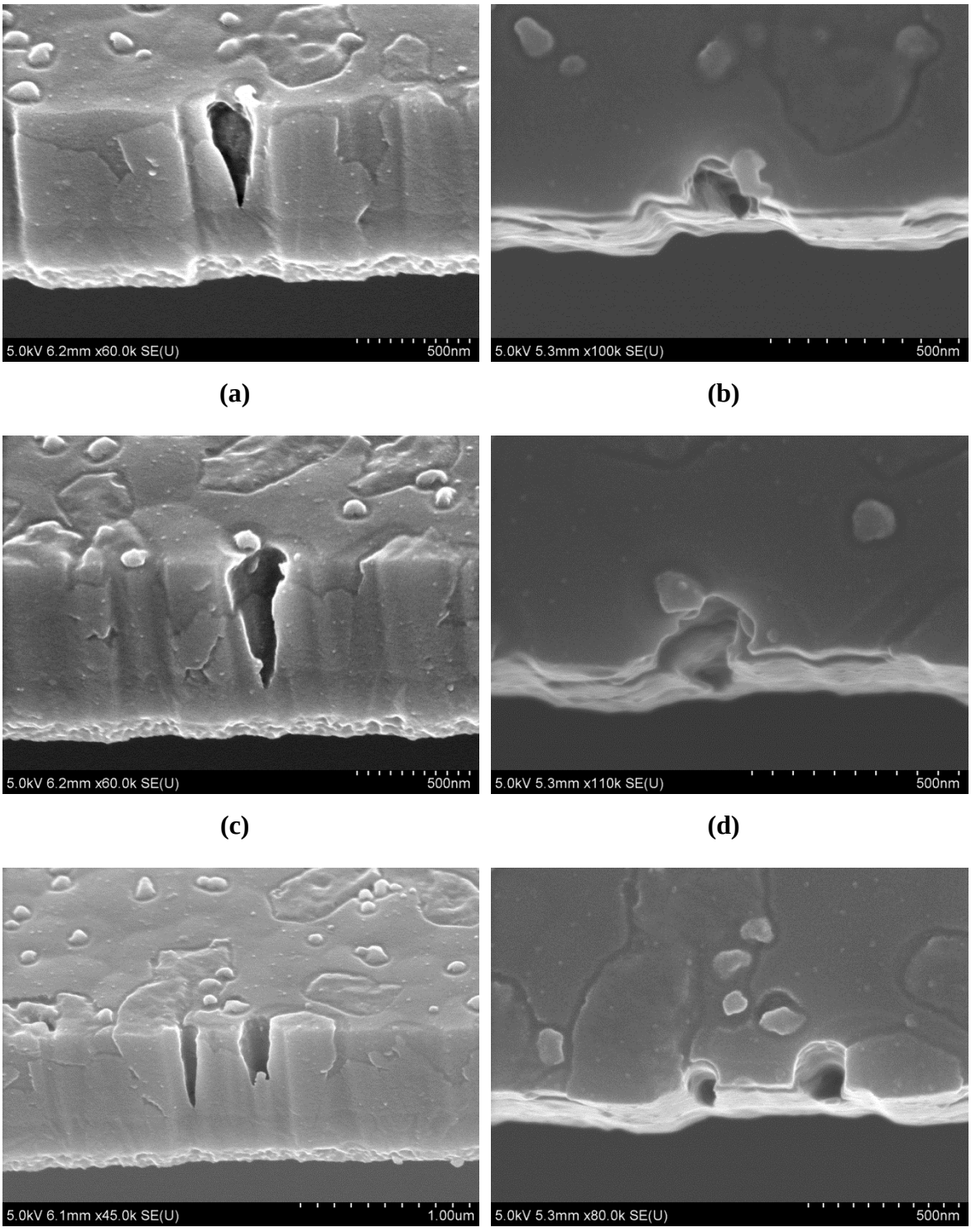

Figure 3.15. (a,c,e) Sidewall and **(b,d,f)** corresponding top surface views of specimen edge defects in 2.0% PSG doped columnar polysilicon.

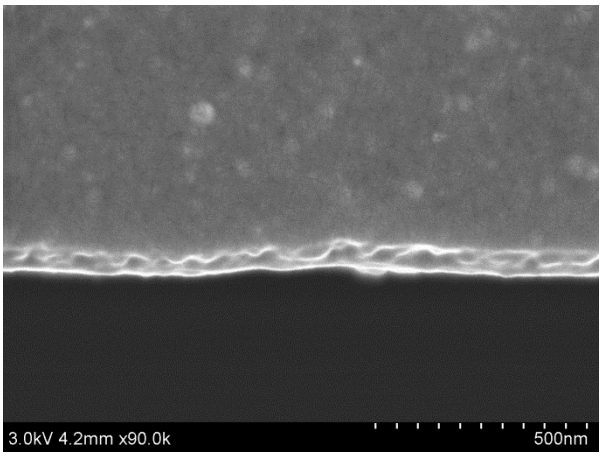

(a)

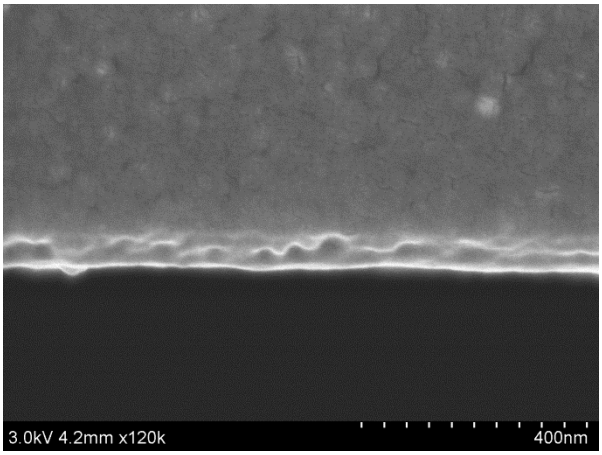

(b)

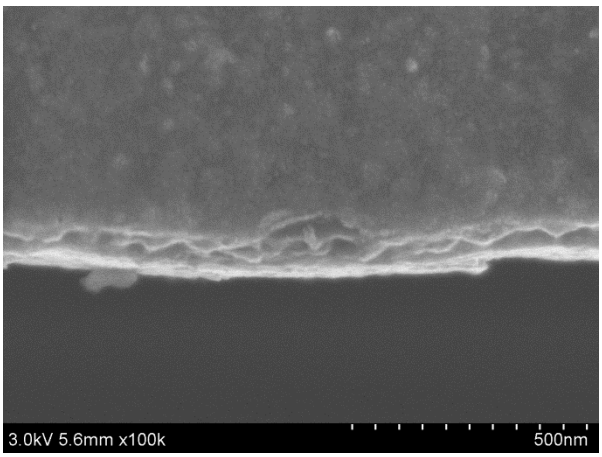

(c)

Figure 3.16. (a-c) Top view of defects at the edge step of the bottom surface of undoped laminated polysilicon.

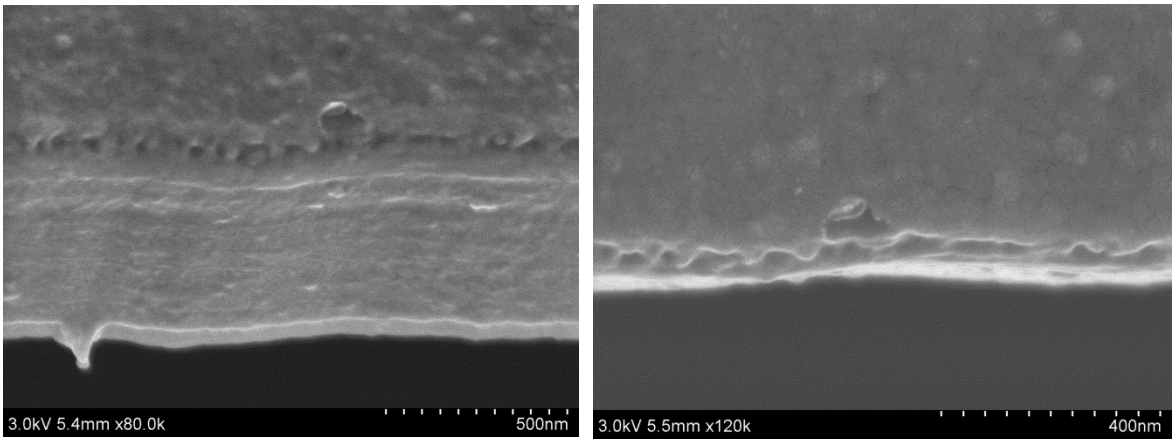

(a) **(b)**

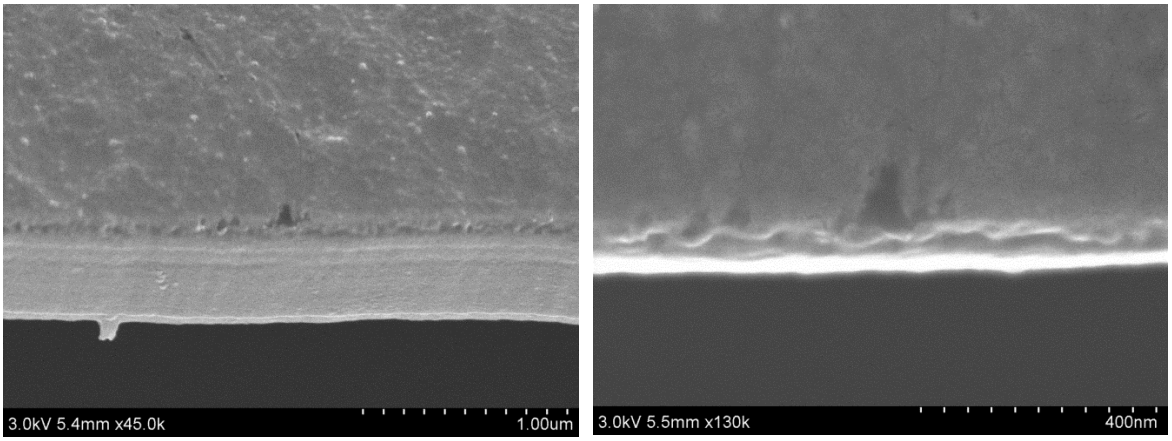

(c) **(d)**

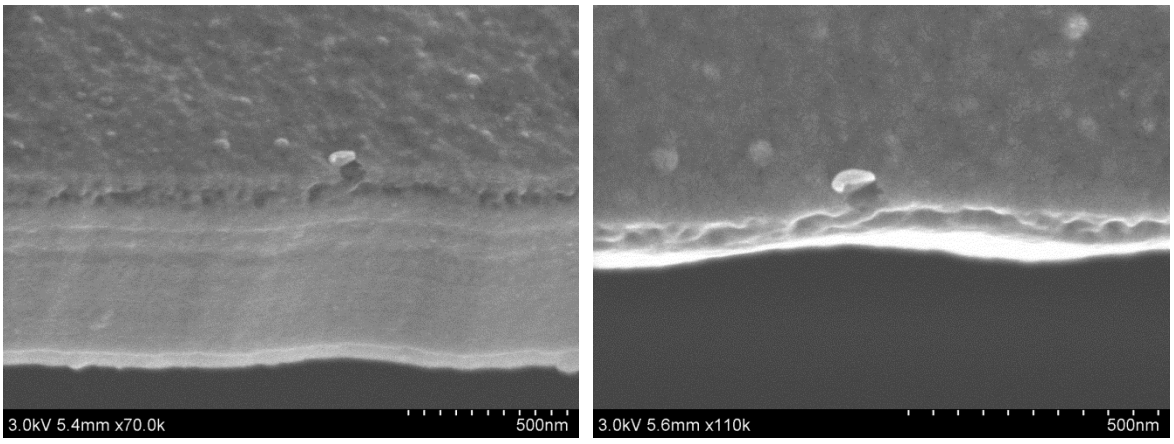

(e) **(f)**

Figure 3.17. (a,c,e) Sidewall and **(b,d,f)** corresponding top surface views of specimen edge defects at the step of the bottom surface of 2.0% PSG doped laminated polysilicon.

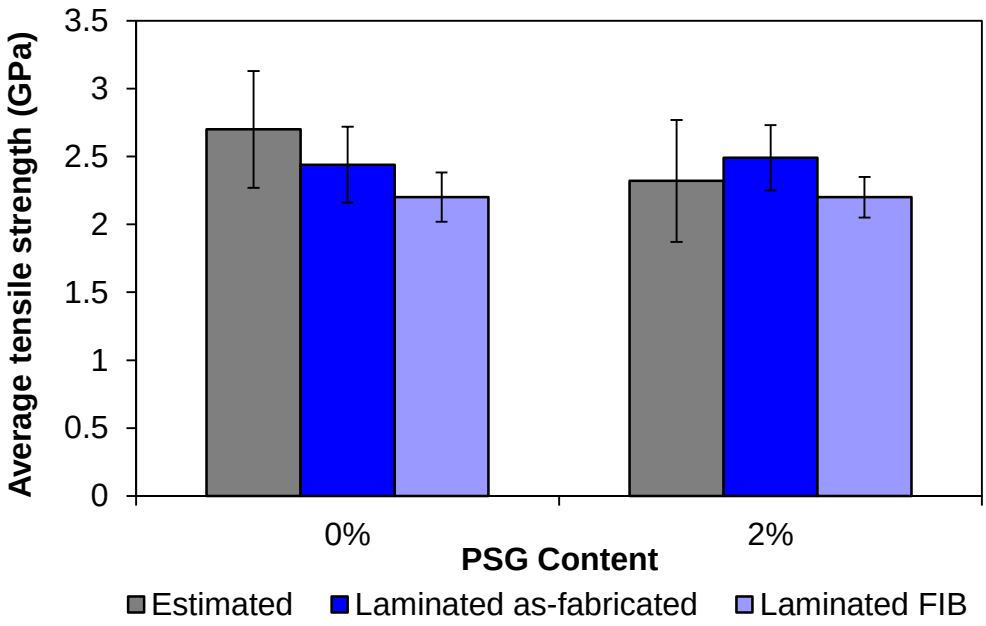

(a)

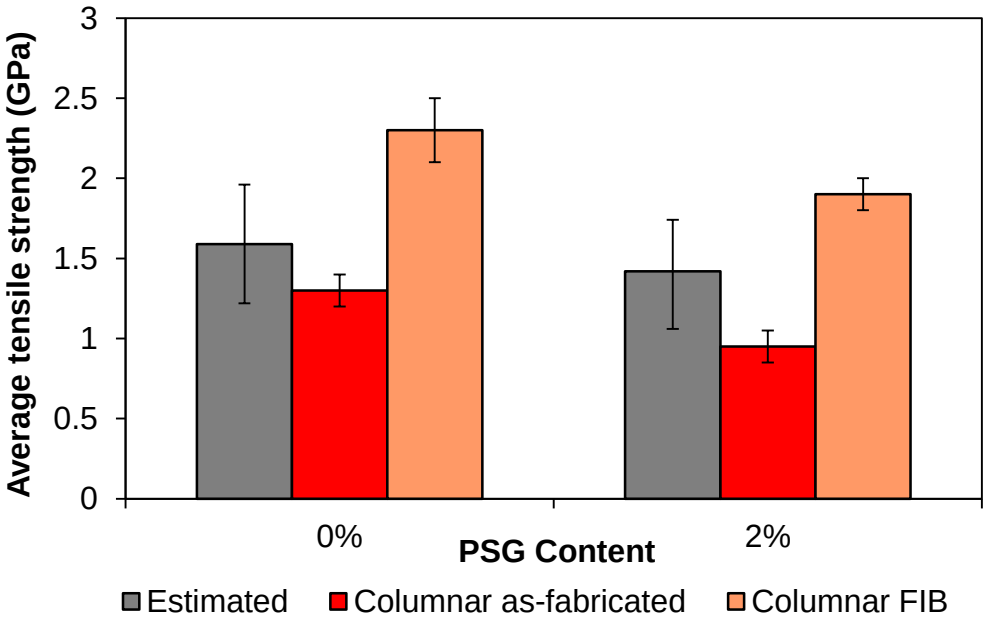

(b)

Figure 3.18. Comparison of estimated and measured tensile strengths of as-fabricated and ion beam milled sidewalls for **(a)** laminated, and **(b)** columnar polysilicon. The tensile strength was estimated by assuming the edge cracks as the critical defects.

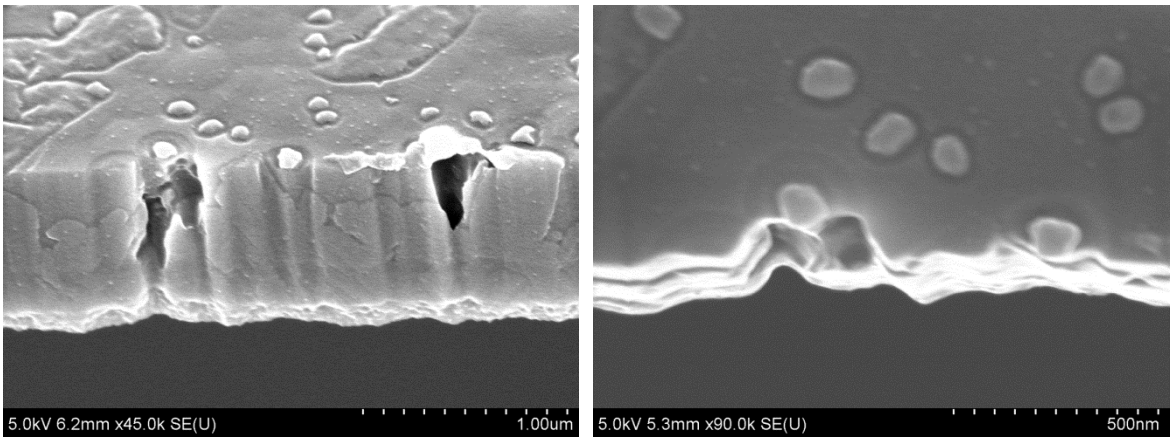

(a) **(b)**

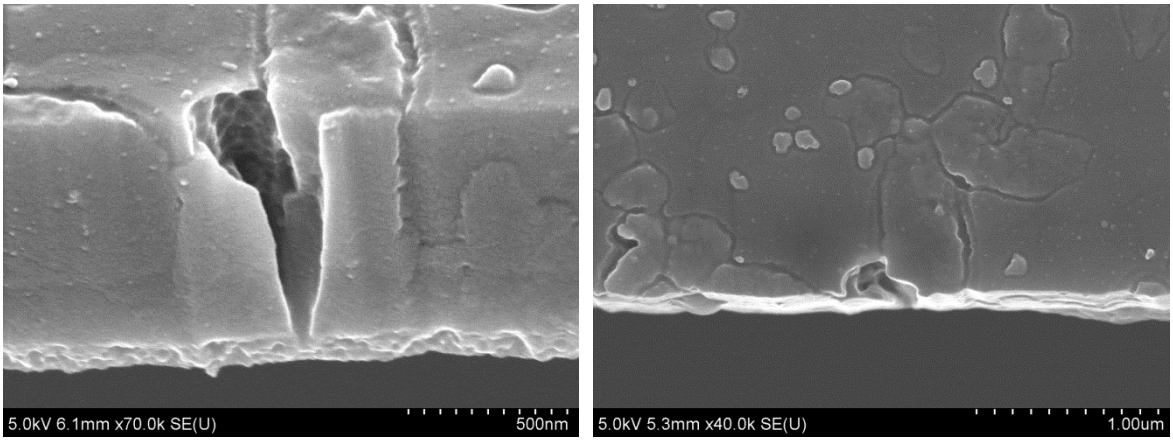

(c) **(d)**

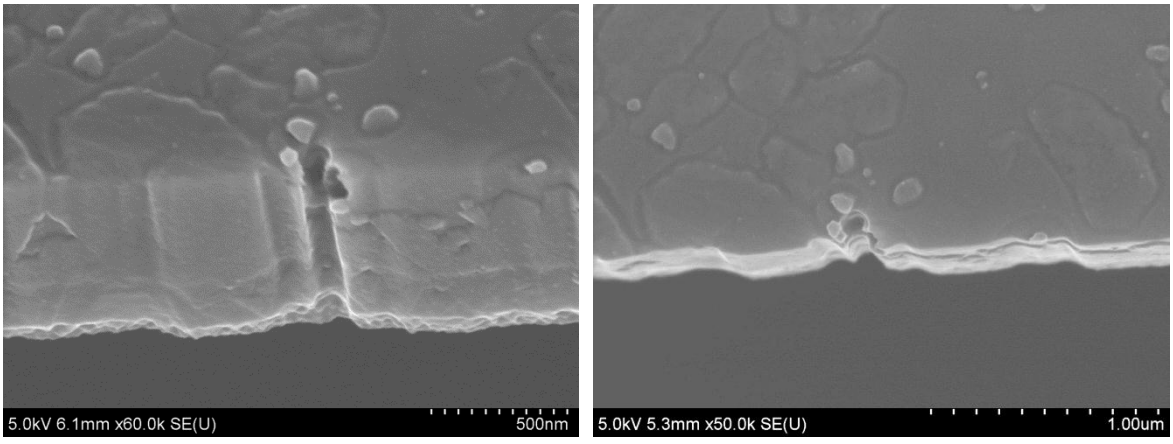

(e) **(f)**

Figure 3.19. (a,c,e) Sidewall and **(b,d,f)** corresponding top surface views of specimen edge defects in 2.0% PSG doped columnar polysilicon.

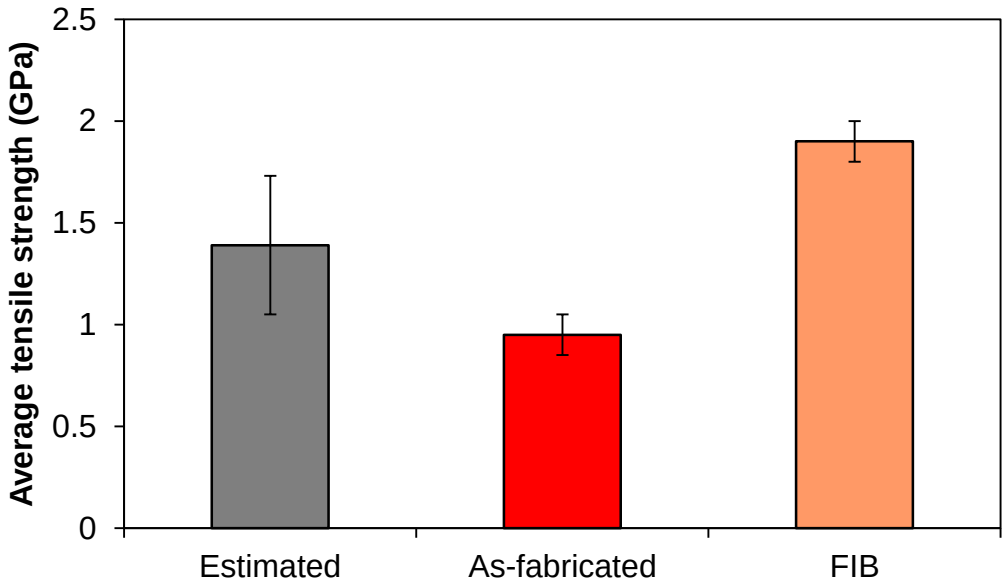

Figure 3.20. Comparison between the estimated and measured tensile strength of as-fabricated and FIB milled sidewalls for 2.0% PSG doped columnar polysilicon. The tensile strength was estimated by assuming edge notches as the critical defects.

3.6 Conclusions

The $K_{IC,eff}$ values of all polysilicon films were measured in the range of 0.8-1.2 MPa√m which is consistent with prior literature data. Due to local material anisotropy at the crack tip, the $K_{IC,eff}$ varied by as much as 40% from specimen to specimen for each type of columnar polysilicon. On the contrary, the $K_{IC,eff}$ of laminated polysilicon varied in a narrower range, due to the averaging effect of different grains in each of the 10 layers, residing at the crack front. P-doping had a beneficial effect on the "intrinsic" crack resistance of columnar grain polysilicon. The average $K_{IC,eff}$ of columnar polysilicon subjected to heavy P-doping was the highest among all films, and by 10% higher than the undoped columnar material. The $K_{IC,eff}$ of doped columnar polysilicon was most frequently in the range of 1.1 - 1.2 MPa√m. The increase in $K_{IC,eff}$ values compared to the undoped material was due to the combined effect of crack tip material anisotropy and

doping. Fracture experiments with Si bicrystals would eliminate the role of polycrystallinity and thus, provide further understanding of the effect of doping on $K_{IC,eff}$.

Since the $K_{IC,eff}$ values of columnar and laminated polysilicon films differed by only 10%, the 60-90% difference in the tensile strength reported in Chapter 2 was owed to differences in the flaw size. By approximating the surface flaws as semi-elliptical and quarter-elliptical edge cracks, an estimate for the tensile strength of the different polysilicon films was made. The tensile strength values estimated from quarter elliptical edge cracks and edge notches were consistent with the experimental strength values, indicating that the strength of polysilicon films was governed by sidewall defects. The use of a statistical distribution that describes the defects on the entire specimen surface, obtained by extensive AFM and SEM imaging, is expected to provide predictions with even better agreement with the experimental tensile strength measurements.

CHAPTER 4

CONCLUSIONS

The objective of this dissertation was to shed light to the convoluted effects of grain structure and doping on the tensile strength and $K_{IC,eff}$ of polysilicon films fabricated for MEMS applications. At the center of this dissertation research was the origin, nature and severity of surface flaws for different types of polysilicon and the statistical nature of the ensuing mechanical strength values as quantified by the cumulative Weibull distribution function. Of special interest was to evaluate the utility of tensile strength data obtained at different laboratories by different experimental methods and very different specimen sizes, fabricated from the same columnar and laminated polysilicon films. This Chapter summarizes the outcomes of this research while making an assessment of the extent that the initial dissertation objectives were met.

4.1 Dissertation Outcomes and Assessment

The Young's modulus of all polysilicon films was measured in the range of 153-158 GPa and was found to be independent of microstructure and doping concentration. These values agreed very well with prior measurements by our lab of the elastic modulus of standard polysilicon specimens fabricated at the Sandia National Laboratories using the SUMMMiT V^{TM} process. Of greater interest were the failure properties of polysilicon films: the tensile strength of laminated polysilicon was 60 - 90% higher than that of columnar grain polysilicon. Furthermore, heavy doping of P using 2.0% PSG lowered the strength of columnar polysilicon by 30%, whereas light doping by 0.5% PSG had no

impact on the mechanical strength and the nature and type of defects encountered in undoped columnar polysilicon. Large defects in the form of surface grooves and crevices were found at the specimen sidewalls of undoped columnar polysilicon, which were accentuated after high temperature annealing and heavy doping. Notably, heavy doping did not result in similar defects in laminated polysilicon, whose mechanical strength did not change after light or heavy doping. Using the experimental results of this dissertation, it was shown that the severe defects at the specimen sidewalls of columnar grain polysilicon were the result of the combination of RIE, P-doping and high temperature annealing. Due to lack of control on specimen fabrication, observations on the polysilicon films after every fabrication step were not possible

The tensile strength of polysilicon with columnar and laminated grain structure was measured from specimens with ion milled sidewalls using a FIB. In the absence of sidewall flaws, the strength of columnar polysilicon was same as the strength of laminated polysilicon that underwent a similar ion beam milling process, and was quite close to the tensile strength of as-fabricated laminated polysilicon specimens, thus indicating that the tensile strength of unpatterned columnar grain and laminated polysilicon films could be the same. The strength of ion beam milled specimens was found to be limited by ion beam induced material damage near the milled sidewalls, tapered specimen edges, and irregularities introduced at the fillets.

The effect of grain structure and doping on $K_{IC,eff}$ of polysilicon was evaluated from thin film specimens with sharp cracks subjected to mode I loading. The $K_{IC,eff}$ values for all polysilicon types varied between 0.8 - 1.2 MPa$\sqrt{m}$ as a result of local material anisotropy at the crack tip, which is consistent with values reported by our group before for polysilicon fabricated by the MUMPs process. Hence, the 60-90% difference in the tensile strength of columnar and laminated polysilicon was not due to changes in the material toughness, rather due to the differences in the flaw nature and dimensions, as evidenced in SEM images. The $K_{IC,eff}$ values for columnar polysilicon were typically higher than that of laminated polysilicon, but the latter displayed a smaller variability. The average $K_{IC,eff}$ of columnar polysilicon doped with 2.0% PSG increased by 10% and this was attributed to the crack tip material anisotropy and change in the cohesive law

between Si-Si due to P doping. Unfortunately, the currently study could not isolate the convoluted effect of material anisotropy and doping on the $K_{IC,eff}$ of polysilicon. Further studies to elucidate this question are proposed in Section 4.2.

By using the aforementioned results for $K_{IC,eff}$, surface flaw data measured with the help of an AFM, and stress intensity relations for simple defect geometries, such as a semi-elliptical surface crack and a quarter-elliptical edge crack, predictions for the tensile strength of polysilicon films and the associated uncertainty bounds were made and compared to the experimental values. When the critical flaw population was correctly identified, the tensile strength predictions for different polysilicon films were consistent with experimental measurements. This approach could evolve into a powerful tool to estimate the mechanical strength as it reduces the need for large numbers of tension experiments. More precise predictions of the tensile strength of polysilicon could be obtained by performing an extensive search for critical defects on the entire specimen surface via an AFM.

4.2 Future Prospects

Further questions rose during this dissertation research, which were not fully investigated but represent significant preliminary studies, are discussed in this Section. This dissertation research showed that modifications to processing of brittle materials can result in significant changes in tensile strength and very modest changes in $K_{IC,eff}$. Even though microstructural differences do not directly influence the measured tensile strength, the fabrication steps employed to achieve a particular microstructure governed the formation of critical flaws. For instance, the origin of critical defects in heavily doped polysilicon was identified in the combination of RIE, P-doping and annealing processes. The proof-of-concept studies presented in Chapter 2, established that the mechanical strengths of laminated and columnar polysilicon are actually quite similar, and additional fabrication steps, such as selective etching of the sidewalls using tetramethylammonium hydroxide solution (TMAH) or chemical oxidation of sidewalls followed by wet etching

in 49% HF, could dramatically improve the tensile strength of columnar grain polysilicon.

Due to the polycrystalline nature of the films at hand, the exclusive effects of P-doping on the fracture resistance of GBs and the silicon grains could not be isolated and quantified. Experiments with Si bicrystals doped with various concentrations of P could eliminate uncertainties due to material heterogeneity and improve our understanding of the effect of doping on GB fracture. In [74,75], Foulk et al. showed that crystal lattice orientation and the strength of GBs can increase the $K_{IC,eff}$ of an heterogeneous brittle material by local crack tip deflection. The addition of P atoms is expected to change the fracture resistance of crystal planes due to replacement of Si-Si bonds with higher strength P-Si bonds. Such an assessment could be obtained by atomistic calculations [81], which, however, still lack experimental verification. In this regard, an assessment of the fracture toughness of Si GBs could be made by double cantilever beam (DCB) fracture experiments with fusion-bonded single crystal Si wafers of different orientations. P-doping of these wafers prior to fusion bonding will provide appropriate specimens to quantify the role of P-doping in GB strength.

Such preliminary experiments were carried out with fusion bonded single crystal Si wafers pre-micromachined chevron notches on their surface as described in [82,83], which were fabricated at the Micro-Nano-Mechanical Systems Cleanroom at the University of Illinois at Urbana-Champaign. The geometry and dimensions of the fracture specimens were adopted from the SEMI standard on interface bond strength [83]. Chevron notched specimens were micro-machined on 4” Si wafers using the process summarized in Figure 4.1(a). A Si wafer was coated with photoresist and subsequently patterned to create 52 1×1 cm^2 DCB specimens with the geometry and dimensions defined by the SEMI standard [83]. A 10 - 15 μm step was etched on the Si surface using the Bosch process and the remaining photoresist on the wafer was removed with a photoresist stripper. The wafer was additionally dipped in Pirana (3:1 concentrated sulfuric acid to hydrogen peroxide) solution for 10 min to completely remove organic residues from the wafer. Before bonding, the Si wafers were treated with 49% HF to remove native oxide on the Si surface and achieve a clean Si-Si interface. The wafers

were then dried using dry N_2 and were immediately bonded in high vacuum and 500 °C using a commercial bonder. The bonded wafers were subsequently annealed at > 700 °C in Ar atmosphere to enhance the interfacial bond strength. The wafer was diced into microscale chevron specimens with the aid of dicing streets patterned on the back side of the Si wafer. Specimens with different GBs and doping conditions can be simulated by bonding wafers with different orientation and resistivity. A schematic of a DCB specimen with a chevron notch and a load vs. time plot of a specimen annealed at 1050 °C are shown in Figures 4.1(b) and 4.1(c), respectively. Even though the 1×1 cm^2 specimens should be treated as plates rather than beams, they are still referred to as DCB specimens in literature. The relationship for the stress intensity at the interface was derived using plate theory as [83]:

$$K_C = \frac{F_{\max}}{B\sqrt{w}} Y_{\min} \tag{4.1}$$

where F_{max} is the maximum load, B is the width of the test structure, w is the length of crack from the loading axis, and Y_{min} is the minimum value of the shape function which is derived by finite element modeling for the particular Chevron notch geometry.

The interface quality is of paramount importance. It was characterized via thermal intensity measurements by a far-field IR microscope. Figure 4.2(a) shows the IR intensity of the bond interface at the tip of the chevron notch prior to loading. Wafers bonded at 500 °C in vacuum did not contain voids at the interface. The same interface was imaged after loading and unloading (before catastrophic failure) and is compared to the as-fabricated specimen in Figures 4.2(a,b). More accurate and detailed information could be obtained by TEM imaging which can also identify the presence of an interface oxide.

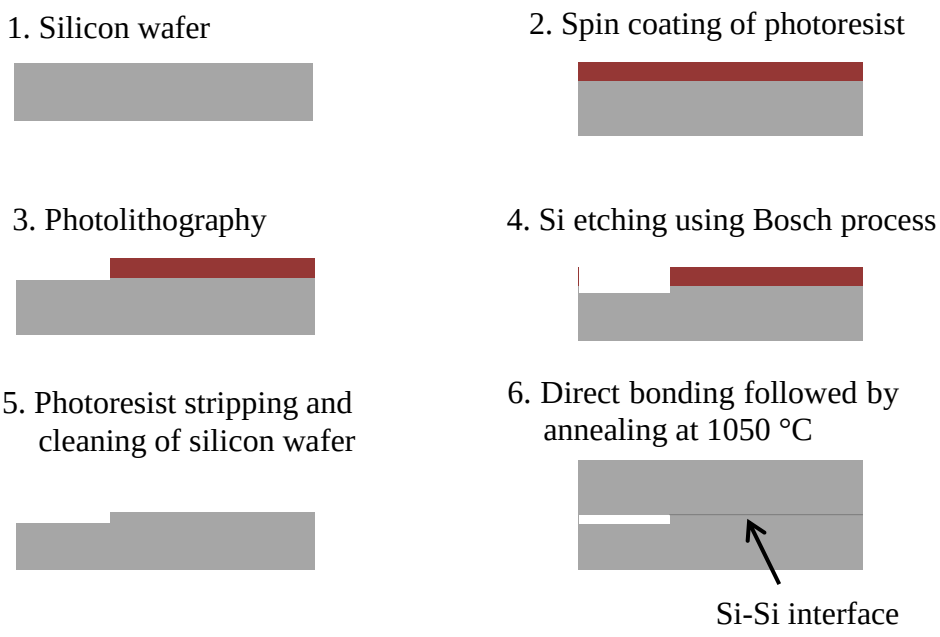

(a)

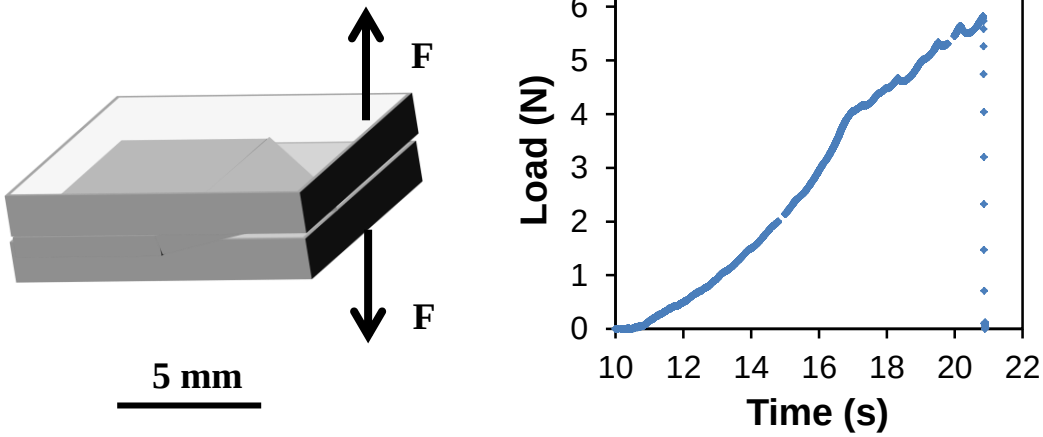

(b) **(c)**

Figure 4.1. **(a)** Step by step approach to bond Si wafers, **(b)** schematic of a DCB specimen loaded under mode I, **(c)** load vs. time plot from a DCB specimen annealed at 1050 °C.

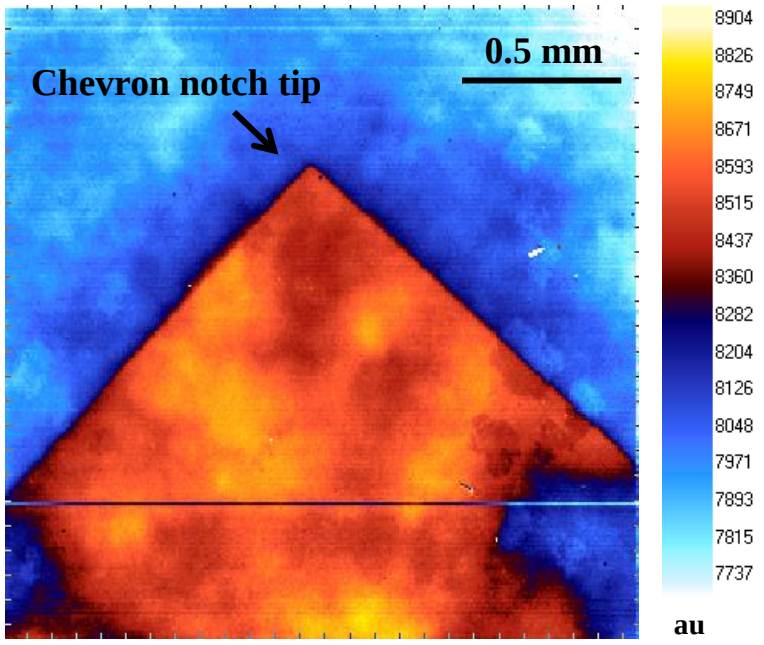

(a)

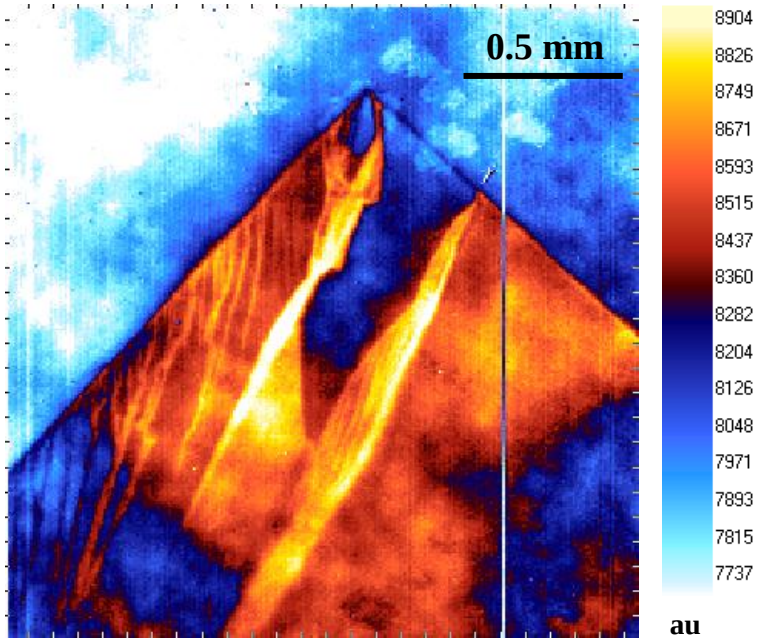

(b)

Figure 4.2. IR image of the interface at the chevron notch tip **(a)** before loading, and **(b)** after loading but before complete fracture. The contour bars show the IR intensity in arbitrary units.

Preliminary experiments were conducted with the aforementioned DCB specimens. A crack initiated at the chevron notch tip during loading and grew slowly as a function of loading until it reached a critical length. Experiments with DCB specimens annealed at 500 °C, 700 °C, 800 °C and 1050 °C after direct bonding showed a temperature dependence of interface bond strength, as shown in Figure 4.3. SEM images of the fracture interface showed that the crack front preferentially propagated along the [110] direction due to the smaller energy release rate along that direction in (111) planes. Further experiments, however, are needed to resolve the two experimental challenges encountered in this study, namely **(a)** achieving a perfect Si-Si interface without voids or a native oxide, and **(b)** driving the crack consistently and completely through the bond interface.

Similarly, the critical stress intensity factors of doped GBs could be evaluated with chevron notched specimens are fabricated by bonding (100)-(100), (110)-(110) and (111)-(111) oriented Si wafers, which have been pre-doped with different concentrations of *P*. In addition to GBs, dopants are expected to alter the fracture toughness of the Si crystal itself. The effect of P-doping on the K_{IC} of some crystal planes of silicon, such as (001), (110) and (111), could be quantified by indentation experiments as reported in [68].

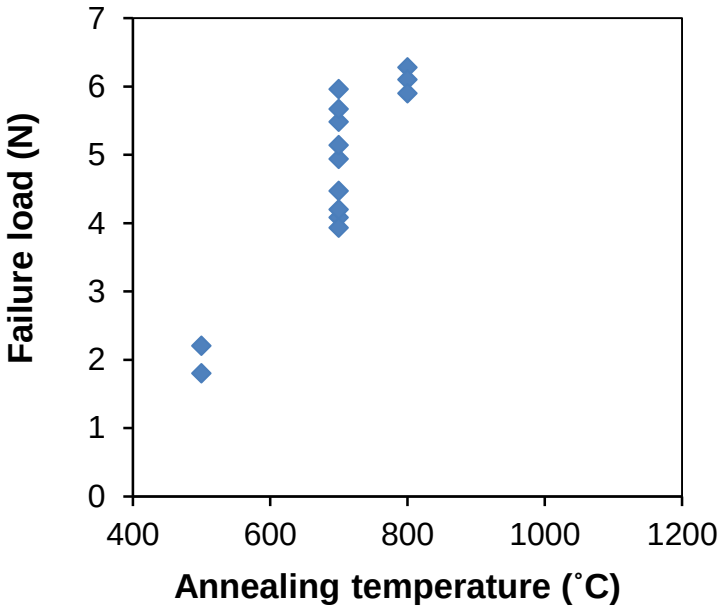

(a)

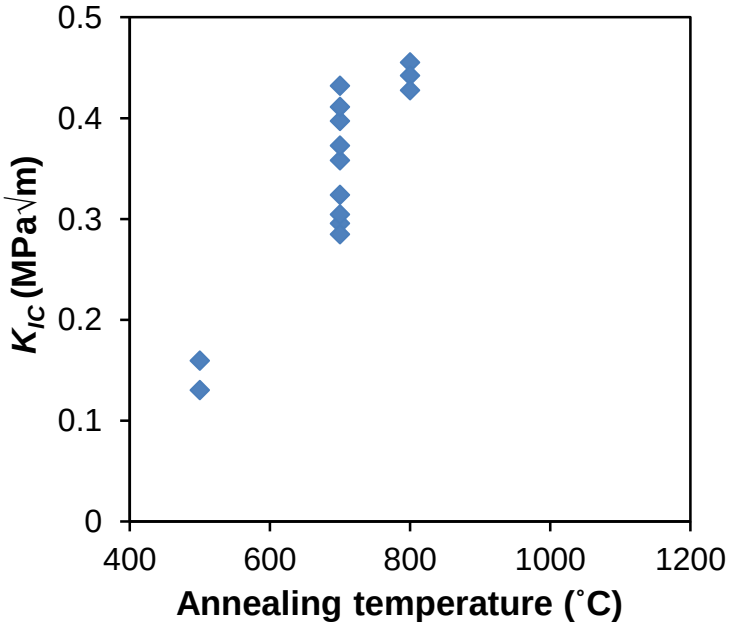

(b)

Figure 4.3. (a) Chevron notch failure load and, **(b)** K_{IC} of directly bonded (111) silicon wafers as a function of annealing temperature.

APPENDIX A

A.1 Uncertainty Calculations

The following Matlab code was used for the uncertainty calculations in this thesis. The script calculates the propagation of uncertainty in a given function *sigma* [80].

```
function sigma = PropError(f,varlist,vals,errs)
%(c) 2010, Brad Ridder.
n = numel(varlist);
sig = vpa(ones(1,n));
for i = 1:n
   sig(i) = diff(f,varlist(i),1);
end
error1 =sqrt((sum((subs(sig,varlist,vals).^2).*(errs.^2))));
error = double(error1);
sigma = [{subs(f,varlist,vals)} {'+/-'} {error};
```

Sigma for semi-elliptical surface crack

```
syms k a c
% Boundary correction factor Fs was insensitive to a and c and was calculated as 1.12
sigma = k/ sqrt(pi*a/(1+1.464*(a/c)^1.65))/1.12
% The uncertainty in the tensile strength of polysilicon films was computed by
substituting corresponding uncertainties values for k, a, and c.
```

```
s=PropError(sigma,[k a c],[.971e6 21.05e-9 (1191e-9)/2],[.149e6 2.75e-9 (508e-9)/2])
```

Sigma for quarter elliptic edge crack

```
syms k a c
% For a/c<1
% Boundary correction factor Fe was insensitive to a and c and was calculated as 1.17
sigma = k/ sqrt(pi*a/(1+1.464*(a/c)^1.65))/1.17
%For  a/c>1
sigma = k/ sqrt(pi*a/(1+1.464*(c/a)^1.65))/((sqrt(c/a)*(1.08-0.03*c/a))+
0.375*(c/a)^2*(a/1e-6)^2-0.25*(c/a)^2*(a/1e-6)^4)/1.08
s=PropError(sigma,[k a c],[0.951e6 100e-9 (96e-9)],[.119e6 100e-9 (28.5e-9)])
```

Sigma for edge notch

```
syms k a
w=100e-6 % w is width of the specimen
sigma = k/sqrt(pi*a)/(1.122-0.231*(a/w)+10.55*(a/w)^2);
s=PropError(sigma,[k a],[1.058e6 162.4e-9],[.14e6 36e-9])
```

REFERENCES

[1] http://mems.sandia.gov/gallery/images.html

[2] W.C. Tang, T-C. Nguyen, M.W. Judy, and R.T. Howe, "Electrostatic-comb drive of lateral polysilicon resonators", Sensors and Actuators A: Physical, 21 (1-3), pp. 328-331, 1990

[3] R. Legtenberg, A.W. Groeneveld and M. Elwenspoek, "Comb-drive actuators for large displacements", Journal of Micromechanics and Microengineering, 6 (3), pp. 320-329, 1996

[4] J. Yasaitis, M. Judy, T. Brosnihan, P. Garone, N. Pokrovskiy, D. Sniderman et al, "A modular process for integrating thick polysilicon MEMS devices with sub-micron CMOS", Micromachining and Microfabrication Process Technology VIII, Proceedings of SPIE, 4979, pp. 145-154, 2003

[5] A. Ghisi, S. Kalicinski, S. Mariani, I. De Wolf, and A. Corigliano, "Polysilicon MEMS accelerometers exposed to shocks: numerical–experimental investigation", Journal of Micromechanics and Microengineering, 19, 035023, 2009

[6] J.B. Sampsell, "Digital micromirror device and its application to projection displays", Journal of Vacuum Science & Technology B, 12 (6), pp. 3242-3246, 1994

[7] S. Kurth, R. Hahn, C. Kaufman, K. Kehr, J. Mehner, U. Wollman, W. Dotzel, and T. Gessner, “Silicon mirrors and micromirror arrays for spatial laser beam modulation”, Sensors and Actuators A, 66, pp. 76-82, 1998

[8] T. Gessner, W. Dotzel, D. Billep, R. Hahn, C. Kaufmann, K. Kehr, S. Kurth, C. Steiniger, and U. Wollman, “Silicon mirror arrays fabricated by using bulk- and surface- micromachining”, Proceeding of SPIE, 3008, pp. 296-305, 1997

[9] D.L. Hetherington and J.J. Sniegowski, "Improved polysilicon surface-micromachined micromirror devices using chemical-mechanical polishing", Proceedings of SPIE on Photonics for Space Environments VI,3440, 1998

[10] http://mems.sandia.gov/gallery/images/cl1a.jpg

[11] http://mems.sandia.gov/gallery/images/gear-mesh_1.jpg

[12] SUMMiT V^{TM} five level surface micromachining technology design manual, version 3.2, Sandia National Laboratories, Albuquerque, New Mexico

[13] S.B. Brown and E. Jansen, "Reliability and long term stability of MEMS", Proceedings of Advanced Application of Lasers in Materials, pp. 9 -10, 1996

[14] D.M. Tanner at el., "MEMS reliability: Infrastructure, test structures, experiments, and failure modes", Sandia Report, SAND2000-0091, 2000

[15] A. McCarty, and I. Chasiotis, "Description of Brittle Failure of Non-uniform MEMS Geometries", Thin Solid Films 515, pp. 3267-3276, 2007

[16] I. Chasiotis, and W.G. Knauss, "The mechanical strength of polysilicon films: Part 2. Size effects associated with elliptical and circular perforation", Journal of the Mechanics and Physics of Solids, 51 (8), pp. 1551-15, 2003

[17] D.C Miller, B.L Boyce, P.G Kotula, and C.R Stoldt, "Connections between morphological and mechanical evolution during galvanic corrosion of micromachined polycrystalline and monocrystalline silicon", Journal of Applied Physics, 103, 123518, 2008.

[18] I. Chasiotis, "Mechanics of thin films and microdevices", IEEE Transactions of Devices, Materials, and Reliability, 4 (2), pp. 176-188, 2004

[19] T. Alan, M.A. Hines, and A.T. Zehnder, "Effect of surface morphology on the fracture strength of silicon nanobeams", Applied Physics Letters, 89 (9), Art. no. 091901, 2006

[20] T. Alan, A.T. Zehnder, D. Sengupta, and M.A. Hines, "Methyl monolayers improve the fracture strength and durability of silicon nanobeams", Applied Physics Letters, 89, 231905, 2006

[21] D. Roundy and M. Cohen, "Ideal strength of diamond, Si, and Ge", Physical Review B, 64 (21), 212103, 2001

[22] S. Sundararajan, B. Bhushan, T. Namazu, and Y. Isono, "Mechanical property measurements of nanoscale structures using an atomic force microscope", Ultramicroscopy, 91 (1-4), pp. 111-118, 2002

[23] T. Namazu, Y. Isono, and T. Tanaka, "Evaluation of size effect on mechanical properties of single crystal silicon by nano-scale bending test using AFM", Journal of Microelectromechanical systems, 9, pp. 450-459, 2000

[24] W. Sharpe Jr., K. Jackson, J. Hemker, and Z. Xie, "Effect of specimen size on young's modulus and fracture strength of polysilicon", Journal of Microelectromechanical Systems, 10 (3), pp. 317-326, 2001

[25] J. Koskinen, J. Steinwall, R. Soave, and H. Johnson, "Microtensile testing of free-standing polysilicon fibers of various grain sizes", Journal of Micromechanics and Microengineering, 3 (1), pp. 13-17, 1993

[26] B.L. Boyce, J.M. Grazier, T.E. Buchheit and M.J. Shaw, "Strength distributions in polycrystalline silicon MEMS", Journal of Microelectromechanical Systems, 16 (2), pp. 179-190, 2007

[27] S.S. Hazra, M.S. Baker, J.L. Beuth, and M.P. De Boer, "Demonstration of an in situ on-chip tensile tester", Journal of Micromechanics and Microengineering, 19 (8), art. no. 082001, 2009

[28] E.D. Reedy Jr., B.L. Boyce, J.W. Foulk III, R.V. Field Jr.,M.P. de Boer, and S.S. Hazra, "Predicting fracture in micrometer-scale polycrystalline silicon MEMS structures", Journal of Microelectromechanical Systems, 20 (4), pp. 922-932, 2011

[29] R. Ballarini, H. Kahn, N. Tayebi, and A.H. Heuer, "Effects of microstructure on the strength and fracture toughness of polysilicon: A wafer level testing approach," ASTM special technical publication, 1413, pp. 37-51, 2001

[30] G.C. Johnson, P.T. Jones, and R.T. Howe, "Materials characterization for MEMS-A comparison of uniaxial and bending tests", Proceedings of the SPIE Conference on Micromachining and Microfabrication Process Technology V, 3874, pp. 94-101, 1999

[31] M.J. Madou, "Fundamentals of Microfabrication", CRC Press, 2002

[32] T. Kammins, "Polycrystalline silicon for integrated circuits and displays", 2nd ed., Kluwer Academic Publishers, Chapter 2, pp. 103-114

[33] J. Akhtar, S.K. Lamichhane, and P. Sen, "Thermal-induced normal grain growth mechanism in LPCVD polysilicon film", Materials Science in Semiconductor Processing, 8, pp. 476-482, 2005

[34] Y. Wada and S. Nishimatsu, "Grain growth mechanism of heavily phosphorus implanted polycrystalline silicon", Journal of Electrochemical Society, 125 (9), pp. 1499-1504, 1978

[35] V.P Lesnikova, A.S Turtsevich, V.Y Krasnitsky, V.A Emelyanov, O.Y Nalivaiko, S.V Kravtsov, and T.V Makarevich, "The structure, morphology and resistivity of in situ phosphorus doped polysilicon films", Thin Solid Films, 247 (2), pp. 156-161, 1994

[36] T.A. Lober and R.T. Howe, "Surface-micromachining processes for electrostatic microactuator fabrication", Solid-State Sensors and Actuators Workshop, pp. 59-62, 1988

[37] H. Kahn, C. Deeb, I. Chasiotis and A. Heuer, "Anodic Oxidation During MEMS Processing of Silicon and Polysilicon: Native Oxides Can Be Thicker Than You Think", Journal of Micromechanical systems, 14 (5), pp. 914-923, 2005

[38] J.A. Walker and K.J. Gabriel, "Mechanical integrity of polysilicon films exposed to hydrofluoric acid solutions", Journal of Electronic Materials, 20 (9), pp. 665-670, 1991

[39] D.C. Miller, W.L. Hughes, Z-L. Wang, K. Gall and C.R. Stoldt, "Mechanical Effects of Galvanic Corrosion on Structural Polysilicon", Journal of Microelectromechanical Systems, 16 (1), pp. 87-101, 2007

[40] T. Tsuchiya, J. Sakata and Y. Taga, "Tensile strength and fracture toughness of surface micromachined polycrystalline silicon thin films prepared under various conditions" MRS Symposium Proceedings, 505 , pp. 285-290, 1997

[41] B.L. Boyce, M.J. Shaw, P. Lu, and M.T. Dugger, "Stronger silicon for microsystems", Acta Materialia, 58, pp. 439-448, 2010

[42] R.E. Proano and D.G. Ast, "Effects of the presence/absence of HCl during gate oxidation on the electrical and structural properties of polycrystalline silicon thin film transistors", Journal of Applied Physics, 66, pp. 2189-2199, 1989

[43] I. Chasiotis, and W.G. Knauss, "The mechanical strength of polysilicon films: Part 1. The influence of fabrication governed surface conditions", Journal of the Mechanics and Physics of Solids, 51 (8), pp. 1533-1550, 2003

[44] C.P. Chen, and M.H. Leipold, "Fracture toughness of silicon", American Ceramics Society Bulletin, 59, pp. 519, 1980

[45] R. Plugaru, E. Vasile, C. Cobianu, and D. Dascalu, "Investigation of the surface of P-implanted LPCVD silicon films", Materials Science and Engineering: B, 42 (1-3), pp. 240-242, 1996

[46] V.P Lesnikova, A.S Turtsevich, V.Y Krasnitsky, V.A Emelyanov, O.Y Nalivaiko, S.V Kravtsov, and T.V Makarevich, "The structure, morphology and resistivity of in situ phosphorus doped polysilicon films", Thin Solid Films, 247 (2), pp. 156-161, 1994

[47] K. Park, S. Batra, and S. Banerjee, "Role of negatively charged vacancies in secondary grain growth in polycrystalline silicon during rapid thermal annealing", Applied Physics Letters, 58 (21), pp. 2414-2416, 1991

[48] H.-J. Kim and C.V. Thompson, "Kinetic modeling of grain growth in polycrystalline silicon films doped with phosphorus and boron", Journal of Electrochemical Society, 135 (9), pp. 2312-2319, 1988

[49] H. Puchner, and S. Selberherr, "An advanced model for dopant diffusion in polysilicon", IEEE Transactions on Electron Devices, 42 (10), pp. 1750-1755, 1995

[50] M. Biebl and H. von Philipsborn, "Fracture strength of doped and undoped polysilicon", Proceedings of the 8th International Conference on Solid State Sensors and Actuators, 3, pp. 72-75, 1995

[51] Z. Zeng, X. Ma, J. Chen, Y. Zeng, D. Yang, and Y. Liu, "Effects of heavy phosphorus-doping on mechanical properties of Czochralski silicon", Journal of Applied Physics, 107 (12), pp. 123503-1-5, 2010

[52] J.G. Swadener and M. Nastasi, "Effect of dopants on the fracture toughness of silicon", Journal of Materials Science Letters, 21 (17), pp. 1363-1365, 2002

[53] I. Chasiotis, S.W. Cho, and K. Jonnalagadda, "Fracture toughness and subcritical crack growth in polycrystalline silicon", Journal of Applied Mechanics 73 (5), pp. 714-722, 2006

[54] S.W. Cho and I. Chasiotis, "Elastic properties and representative volume element of polycrystalline silicon for MEMS," Experimental Mechanics, 47 (1), pp. 37-49, 2007

[55] I. Chasiotis and W.G. Knauss, "Experimentation at the micron- and submicron scale", in Comprehensive Structural Integrity Vol. 8. Interfacial and Nanoscale Failure. Volume Editors: W. Gerberich and W. Yang, Elsevier Science, Oxford, U.K., pp. 41-87, 2003

[56] J.J. Sniegowski and M.P. de Boer, "IC-compatible polysilicon surface micromachining", Annual Review of Material Science, 30, pp. 299-333, 2000

[57] D.H. Alsem, B.L. Boyce, E.A. Stach, and R.O. Ritchie, "Effect of post-release sidewall morphology on the fracture and fatigue properties of polycrystalline silicon structural films", Sensors and Actuators A: Physical, 147 (2), pp. 553-560, 2008

[58] K. Jonnalagadda, I. Chasiotis, S. Yagnamurthy, J. Lambros, J. Pulskamp, R. Polcawich, and M. Dubey, "Experimental investigation of strain rate dependence of nanocrystalline Pt films", Experimental Mechanics, 50, pp. 25-35, 2010

[59] B.D. Jensen, M.P. de Boer, N.D. Masters, F. Bitsie, and D.A. LaVan, "Interferometry of actuated microcantilevers to determine material properties and test structure nonidealities in MEMS", Journal of Microelectromechanical Systems, 10 (3), pp. 336-346, 2001

[60] W.N. Sharpe, B. Yuan, R. Vaidyanathan, and R.L. Edwards, "Measurements of Young's modulus, Poisson's ratio, and tensile strength of polysilicon", Proceedings of the IEEE, Tenth Annual International Workshop on MicroElectroMechanical Systems, pp. 424-429, 1997

[61] P.T. Jones, G.C. Johnson, and R.T. Howe, "Fracture strength of polycrystalline silicon", MRS proceedings, 518, pp. 197-202, 1998

[62] J.J. Wortman and R.A. Evans, "Young's modulus, shear modulus, and Poisson's ratio in silicon and germanium", Journal of Applied Physics, 36 (1), pp. 153-156, 1965

[63] M.A. Hopcroft, W.D. Nix, and T.W. Kenny, "What is the Young's modulus of silicon?", Journal of Microelectromechanical systems, 19 (2), pp. 229-238, 2010

[64] A. Hallinan Jr., "A review of the Weibull distribution", Journal of Quality Technology, 25 (2), pp. 85-93, 1993

[65] W.M. Robertson, "Thermal etching and grain-boundary grooving of silicon ceramics", Journal of the American Ceramic Society, 64 (1), pp. 9-13, 1981

[66] A.M. Smith, Fundamentals of silicon integrated device technology, 1967

[67] M. Steyer, A. Dastgheib-Shirazi, H. Wagner, G. Micard, P.P. Altermatt, and G. Hahn, "A study of various methods for the analysis of the phosphosilicate glass layer", 27th European Photovoltaic Solar Energy Conference and Exhibition in Frankfurt, Germany, pp. 1325-1328, 2012

[68] F. Ebrahimi, and L. Kalwani, "Fracture anisotropy in silicon single crystal", Materials Science and Engineering: A, 268 (1-2), pp. 116-126, 1999

[69] Y. Tsai and J. Mecholsky, "Fractal fracture of single crystal silicon", Journal of Materials Resources, 6, pp. 1248–1263, 1991

[70] A.M. Fitzgerald, R.H. Dauskardt and T.W. Kenny, "Fracture toughness and crack growth phenomena of plasma-etched single crystal silicon", Sensors and Actuators A, 83, pp. 194–199, 2000

[71] H. Kahn, N. Tayebi, R. Ballarini, R.L. Mullen, and A.H. Heuer, "Fracture toughness of polysilicon MEMS devices", Sensors and Actuators A: Physical, 82 (1-3), pp. 274-280, 2000

[72] J. Bagdahn, J. Schischka, M. Petzold, and W.N. Sharpe Jr., "Fracture toughness and fatigue investigations of polycrystalline silicon", Proceedings of SPIE - The International Society for Optical Engineering, 4558, pp. 159-168, 2001

[73] S.W. Cho, K. Jonnalagadda, and I. Chasiotis, "Mode I and mixed mode fracture of polysilicon for MEMS", Fatigue and Fracture of Engineering Materials and Structures, 30 (1), pp. 21-31, 2007

[74] J.W. Foulk, III, G.C. Johnson, P.A. Klein, and R.O. Ritchie, "A micromechanical basis for partitioning the evolution of grain bridging in brittle materials", Journal of the Mechanics and Physics of Solids, 55 (4), pp. 719-743, 2007

[75] J.W. Foulk, III, G.C. Johnson, P.A. Klein, and R.O. Ritchie, "On the toughening of brittle materials by grain bridging: Promoting intergranular fracture through grain angle, strength, and toughness", Journal of the Mechanics and Physics of Solids, 56 (6), pp. 2381-2400, 2008

[76] H. Tada, P.C. Paris, and G.R. Irwin, , The stress analysis of cracks handbook, 3rd ed., ASME Press, New York, pp. 52–53, 2000

[77] D.R. Lide, Handbook of chemistry and physics, 85th Ed, CRC Press LLC

[78] J.C. Newman and I.S Raju, “Stress intensity factor equations for cracks in three-dimensional finite bodies”, ASTM STP791-EB / STP37074S, 1983

[79] J.R. Taylor, "An introduction to error analysis: The study of uncertainities in physical measurements", Chapter 3, pp. 61, 2nd Ed., University Science Books.

[80] http://www.mathworks.com/matlabcentral/fileexchange/17901-propagation-of-uncertainty/content/PropError.m

[81] R. Perez and P. Gumbsch, "An ab initio study of the cleavage anisotropy in silicon", Acta Materialia, 48 (18-19), pp. 4517-4530, 2000

[82] M. Petzold, J. Bagdahn, D. Katzer, “Quality and mechanical reliability assessment of wafer-bonded micromechanical components,” Microelectronics Reliability, 39, pp. 1103-1108, 1999

[83] Test method for wafer bond strength measurements using micro-chevron test structures, SEMI MS5-110